HZG REPORT 2011-7 // ISSN 2191-7833

Experimental and Numerical Investigation of Mg Alloy Sheet Forming

(Von der Technischen Fakultät der Christian-Albrechts-Universität zu Kiel als Dissertation angenommene Arbeit)

Mintesnot Nebebe Mekonen

wissen
schafft
nutzen

Helmholtz-Zentrum
Geesthacht
Zentrum für Material- und Küstenforschung

HZG REPORT 2011-7

Experimental and Numerical Investigation of Mg Alloy Sheet Forming

(Von der Technischen Fakultät der Christian-Albrechts-Universität zu Kiel als Dissertation angenommene Arbeit)

Mintesnot Nebebe Mekonen

Helmholtz-Zentrum Geesthacht
Zentrum für Material- und Küstenforschung GmbH | Geesthacht | 2011

Die HZG Reporte werden kostenlos abgegeben.
HZG Reports are available free of charge.

Anforderungen/Requests:

Helmholtz-Zentrum Geesthacht
Zentrum für Material- und Küstenforschung GmbH
Bibliothek/Library
Max-Planck-Straße 1
21502 Geesthacht
Germany
Fax.: +49 4152 87-1717

Druck: HZG-Hausdruckerei

Als Manuskript vervielfältigt.

ISSN 2191-7833

Helmholtz-Zentrum Geesthacht
Zentrum für Material- und Küstenforschung GmbH
Max-Planck-Straße 1
21502 Geesthacht
www.hzg.de

HZG REPORT 2011-7

Experimental and Numerical Investigation of Mg Alloy Sheet Forming

(Von der Technischen Fakultät der Christian-Albrechts-Universität zu Kiel als Dissertation angenommene Arbeit)

Mintesnot Nebebe Mekonen

109 pages with 47 figures and 8 tables

Abstract

In this thesis, a thermodynamically consistent, rate-dependent, finite strain elastoplastic constitutive model for application in sheet forming simulations of magnesium alloys is developed and implemented. The constitutive model is established so that the characteristic mechanical features observed in magnesium alloys such as anisotropy and compression-tension asymmetry can be accommodated. More precisely, a model originally proposed by Cazacu and Barlat in 2004 and later modified to account for the evolution of the material anisotropy is rewritten in a thermodynamically consistent framework. For calibration of the constitutive model, mechanical characterization through uniaxial tensile tests is performed. These tests constitute the magnesium alloys ZE10 and AZ31, both in heat treated condition. For circumventing the poor formability at room temperature, the tests were conducted at elevated temperature (200° C). The uniaxial tensile tests reveal sufficient ductility allowing sheet forming processes at this temperature. Moreover, the differences in yield stresses and plastic strain ratios or r-values confirm the anisotropic response of the materials under study. For predicting limit conditions of a forming process, the localization criterion by Marciniak and Kuczynski is adopted. The calibrated constitutive model together with the localization criterion is implemented in a finite element framework based on a fully implicit time integration. In the implementation, both shell and solid element formulations are considered. The model is verified and finally employed to simulate Nakazima-type forming limit tests. The reasonably good agreement between the responses of the model and the respective experiments, which is demonstrated in terms of force-displacement curves, the loading paths and forming limit diagrams, indicates the predictive capability of the implemented model for the considered magnesium alloys.

Experimentelle und numerische Untersuchung der Blechumformung von Mg-Legierung

Zusammenfassung

In der vorliegenden Arbeit wird ein thermodynamisch konsistentes Materialmodell für die Beschreibung ratenabhängiger großer elastoplastischer Deformationen für die Simulation des Umformens von Magnesiumblechen entwickelt und implementiert. Das Materialmodell erlaubt die Beschreibung der charakteristischen mechanischen Eigenschaften von Magnesiumlegierungen wie Anisotropie und Zug-Druck-Asymmetrie. Ein ähnliches Modell von Cazacu und Barlat (2004) wird dazu in einem thermodynamisch konsistenten Rahmen reformuliert und zur Beschreibung der Evolution der Anisotropie erweitert. Einachsige Zugversuche an den Legierungen AZ31 und ZE10 – beide in wärmebehandeltem Zustand – dienen zur Kalibrierung der Modellparameter. Die Versuche wurden bei 200° C Umgebungstemperatur durchgeführt, um die schlechte Umformbarkeit beider Legierungen bei Raumtemperatur zu umgehen. Die Tests belegten eine ausreichende Duktilität der Materialien für Umformoperationen bei dieser erhöhten Temperatur sowie quantifizierten die Anisotropie in Form von richtungsabhängigen Fließspannungen und Fließrichtung (r-Werte). Zur Vorhersage der Lokalisierung wird das Modell von Marciniak and Kuczynski verwendet. Materialmodell und Lokalisierungskriterium werden Mithilfe eines voll-impliziten Integrationsalgorithmus in ein Finite-Elemente Programm implementiert, wobei sowohl 3D-Kontinuums- als auch Schalenelemente berücksichtigt werden. Das Modell wird verifiziert und schließlich zur Beschreibung von Nakazima-Umformversuchen verwendet. Eine gute Übereinstimmung der Vorhersagen des Modells mit experimentellen Ergebnissen kann erzielt werden, wobei sowohl das Kraft-Verformungsverhalten und die Dehnungspfade, als auch die Grenzformänderungskurven bewertet werden.

Manuscript received / Manuskripteingang in TFP: 14. Dezember 2011

Acknowledgements

I would like to express my heart felt gratitude to my supervisor, Prof. Mosler, for his guidance and close supervision during the course of this work.

My sincere appreciation to Dr. Steglich, Dr. Bohlen and Dr. Letzig who introduced me to this research work, provided me with the required experimental facilities and for the fruitful discussions which ultimately shaped up this work.

My thanx to Dr. Homayonifar, Dr. Kintzel, Dr. Scheider, Dr. Ertürk for the valuable discussions regarding topics focusing on their respective area of expertise and the whole WMS department for creating a live and engaging working environment. Many thanx to Mr. Stutz for the support in conducting the sheet forming tests and the follow up discussions along with the whole WZW department who at one point or another have contributed to the experimental part of my work.

My gratitude also to the examination committee members: Prof. Brocks, Prof. Faupel and Prof. Rätzke for their time and expert opinions on this work.

I would like to thank Prof. Huber and Prof. Kainer for the opportunity to be part of their research works.

Last but not least, many thanx to my family, particularly Ato Beyene, for the moral support during my academic endeavor in Germany.

Contents

1 Introduction

1.1 Motivation

Motivated by the growing demand for light weight materials, research on magnesium and its alloys has been getting more attention. This is attributed to the fact that magnesium is the lightest metal in use for the production of structural components with a promising application in the aircraft and auto industries, see Polmear (2006). Despite the high strength-to-weight ratio, the application of magnesium to these light weight structures has been limited. This limitation is correlated to its pronounced anisotropy, the compression-tension asymmetry as well as its comparably poor formability, specially at room temperature, cf. (Kelley & Hosford, 1968; Hosford & Allen, 1973; Hosford, 1993; Lou et al., 2007; Bohlen et al., 2007). In the objective of resolving the aforementioned limitations, recent research on magnesium is focused on two main topics. The first is the development of new magnesium alloys with improved mechanical properties, see (Bohlen et al., 2007; Hantzsche et al., 2010). The second topic, also the focus of this work, deals with the investigation of the mechanical behavior of the existing alloys at elevated temperatures. The choice of the elevated temperature for the investigation is attributed to the reasonable formability achieved at such condition. A comprehensive account on this topic can be found in (Dröder, 1999; Doege & Dröder, 2001; Chen & Huang, 2003; Agnew & Duygulu, 2003, 2005; Palaniswamy et al., 2004; Chang et al., 2007; Peng et al., 2007; Palumbo et al., 2007; Yi et al., 2010).

The improvement in the formability at elevated temperatures results from the activation of dislocation systems, which are absent at room temperature, cf. (Wonsiewicz & Backofen, 1967a,b; Agnew & Duygulu, 2005). For commercial magnesium alloys, such as AZ31, the aforementioned studies indicate that sufficient formability is observed for temperatures varying between 150^oC and 250^oC. It is also reported that finding the correct forming temperature is highly dependent on the process parameters, such as forming speed, local temperature treatment and clamping force. Despite the encouraging efforts made to understand the mechanical behavior of magnesium alloys at elevated temperatures, the available data on this topic are still limited. To supplement these limited data as well as to get a further insight into the mechanical behavior, the work presented here investigates sheet forming processes at an

elevated temperature, more precisely at 200^oC. This is carried out through both experimental investigation and numerical analyses.

1.1.1 Mechanical characterization of Mg alloy sheets by experiments

Mechanical characterization by experiments is fundamental in understanding the behavior of a given material such as magnesium alloy sheets. This is often achieved through standardized uniaxial tensile and sheet forming tests, cf. (Erichsen, 1914; Keeler & Backofen, 1963; Nakazima et al., 1971; Brozzo et al., 1972; Hasek, 1978). The responses obtained from the uniaxial tensile tests provide information describing magnesium alloy sheets such as the plastic flow, the normal anisotropy as well as the planar anisotropy, see (Banabic et al., 2000). Here, normal anisotropy is described as the ratios of the in-plane and out-of-plane strains, whereas planar anisotropy is quantified based on differences in the stress or strain responses obtained from tests having different prescribed test specimen orientations within the sheet plane.

The sheet forming tests, on the other hand, give valuable information regarding the formability of the sheet metal. There are a number of methods proposed for such tests with the first dating back to Erichsen (1914). Details about these methods can be found in (Banabic et al., 2000). Following the comparative simplicity of the experimental setup, the Nakazima-type forming test is frequently employed, hence also adopted in this work, cf. (Nakazima et al., 1971; Banabic et al., 2000). The large number of sheet forming process parameters such as temperature, contact and friction between the forming tools and work-piece and loading, make the full experimental investigation of the process by such forming tests rather expensive. Therefore, making use of the significant advances in computational power, numerical analyses play a central role in supporting the experimental investigation.

1.1.2 Modeling of Mg alloy sheets

The modeling aspects of the work presented here deal with the development, calibration and implementation of a material model that is suitable for the simulation of sheet forming tests. Evidently, numerical simulations of complex processes, such as sheet forming, require a computationally efficient material model. For that purpose, the so-called phenomenological constitutive models are commonly used. Over the years, several authors proposed a number of such models describing the yielding behavior in terms of macroscopic yield functions, cf. (von Mises, 1928; Hill, 1948, 1990; Karafillis & Boyce, 1993; Cazacu & Barlat, 2001; Drucker, 1949; Cazacu & Barlat, 2004). For instance,

von Mises proposed the first yield function for anisotropic materials in the form of a quadratic function, cf. von Mises (1928). Later Hill introduced a modification of this model for application to orthotropic materials with reduced parameters of anisotropy, cf. Hill (1948). A number of alternative and versatile anisotropic models can be found in (Hill, 1990; Karafillis & Boyce, 1993; Cazacu & Barlat, 2001). However, they do not capture an important feature in magnesium alloy sheets, namely the stress-differential effect. Cazacu & Barlat introduced a yield function (CaBa2004) as a modification of the Drucker model, having the capability to account for the material anisotropy as well as for the stress-differential effect, cf. (Drucker, 1949; Cazacu & Barlat, 2004). The yield function presented in this work is based on CaBa2004. However, this yield function is rewritten in tensor form employing 4th-order transformation tensors associated with the distortion of the yield locus. Even more important and different to CaBa2004, such tensors are not constant here, but evolve according to suitable evolution equations, see (Dafalias, 1979; Graff, 2007). By doing so, the distortional hardening effect (change in shape of the yield locus) can be taken into account. Furthermore, for ensuring a physically sound relation, the constitutive model is recast into a thermodynamically consistent form, cf. (Chaboche et al., 1979; Dafalias et al., 2003; Feigenbaum & Dafalias, 2004).

Having calibrated the constitutive model based on the mechanical characterization, simulating a sheet forming process requires a localization criterion. Such a criterion establishes the limit conditions in the forming process. For that purpose, a number of theoretical models have been proposed over the years. For a comprehensive presentation of these models the interested reader is referred to (Butuc, 2004; Banabic et al., 2000; Kuroda & Tvergaard, 2000). Among these models, the Marciniak and Kuczynski localization criterion is adopted due to its simplicity and frequent use, see Marciniak & Kuczynski (1967). Subsequently, this localization criterion is incorporated within the constitutive model for the prediction of the forming limits.

1.2 Chapters guide

Having introduced the objective of the work, Chapter 2 presents a brief discussion on the fundamentals of continuum mechanics. This is followed by the development of a constitutive model incorporating isotropic and distortional hardening in Chapter 3. For the application of the constitutive model, Chapter 4 presents its numerical implementation within the context of a finite element framework. For predicting the limit conditions in sheet forming process, Chapter 5 details a localization criterion along with its numerical implementation. Chapter 6 and Chapter 7 discuss the experimental investiga-

tions conducted for the mechanical characterization and level of formability of the materials in use, respectively. Based on the mechanical characterization, the calibration of the constitutive model is performed in Chapter 8. Chapter 9 discusses the forming simulations in comparison to the forming limit tests. Finally in Chapter 10, the work is summarized and concluded.

2 Fundamentals of continuum mechanics

This chapter is concerned with the fundamentals of continuum mechanics. As such, a brief account on the kinematics and governing laws is presented. These information are the basis for the description of the material models established in the next chapter. Further details on this topic can be found in (Truesdell & Noll, 1965; Ogden, 1984; Ciarlet, 1988; Wu, 2005; Xiao et al., 2006; Mosler, 2007). A short introduction to tensor algebra and differentiation used in this thesis is presented in Appendix A.

2.1 Kinematics

The deformation of a continuum body is defined by the mapping $\boldsymbol{\varphi}$ of the material particles from an undeformed body Ω to its deformed counterpart $\boldsymbol{\varphi}(\Omega)$ (see Fig. 2.1). With the material particles represented by position vectors $\boldsymbol{X}$ in Ω and $\boldsymbol{x}$ in $\boldsymbol{\varphi}(\Omega)$, the mapping is defined as

$$\boldsymbol{x} = \boldsymbol{\varphi}(\boldsymbol{X}). \tag{2.1}$$

In line with the concept of continua, $\boldsymbol{\varphi}$ is required to be sufficiently smooth and invertible in the interior of the deforming body, cf. Ciarlet (1988). Having these requirements in mind, it is also possible to map an infinitesimal line element $\mathrm{d}\boldsymbol{X}$ to an infinitesimal line element $\mathrm{d}\boldsymbol{x}$ in the deformed body (see Fig. 2.1). In what follows, the respective mapping is referred to as deformation gradient $\mathbf{F}$. Mathematically, the second-order tensor $\mathbf{F}$ is expressed as

$$\mathrm{d}\boldsymbol{x} = \mathbf{F} \cdot \mathrm{d}\boldsymbol{X} \quad \text{with} \quad \mathbf{F} = \frac{\partial \boldsymbol{\varphi}(\boldsymbol{X})}{\partial \boldsymbol{X}}. \tag{2.2}$$

Applying the inverse function theorem to $\boldsymbol{\varphi}$, it can be shown that the determinant of the deformation gradient J has to fulfill the necessary condition

$$\mathrm{J} = \det\mathbf{F} \neq 0. \tag{2.3}$$

Physically, J can be interpreted as the relative measure of the infinitesimal volume element $\mathrm{d}v = \mathrm{d}\boldsymbol{x} \cdot (\mathrm{d}\boldsymbol{x} \times \mathrm{d}\boldsymbol{x})$ of the deformed domain with respect to

$\mathrm{d}V = \mathrm{d}\boldsymbol{X} \cdot (\mathrm{d}\boldsymbol{X} \times \mathrm{d}\boldsymbol{X})$ of the undeformed domain such that

$$\mathrm{J} = \frac{\mathrm{d}v}{\mathrm{d}V}. \tag{2.4}$$

Consequently, the inequality $\mathrm{J} > 0$ has to be satisfied. Having a positive

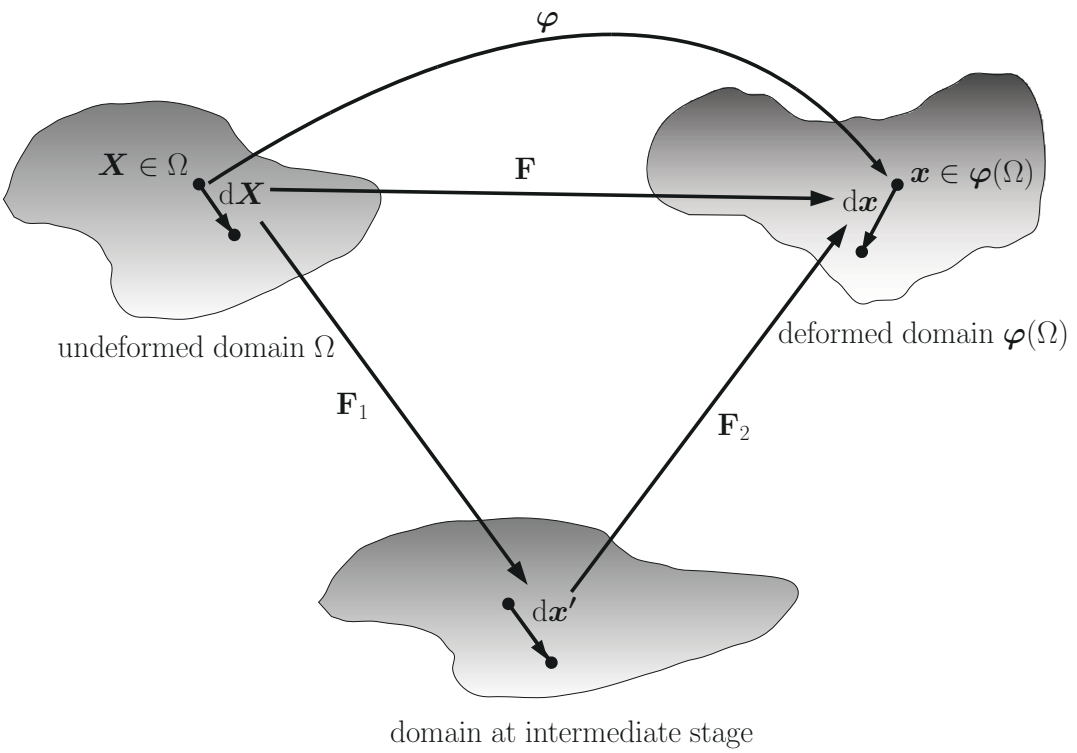

Figure 2.1: Kinematics of a deformable body.

determinant, $\mathbf{F}$ belongs to a special category of tensors called the general linear group (GL). Such tensors can multiplicatively be decomposed into tensors which also belong to GL. By doing so, an intermediate state (domain) can be introduced (see Fig. 2.1). Henceforth, a general form of the decomposition

$$\mathbf{F} = \mathbf{F}_1 \cdot \mathbf{F}_2 \quad \text{with} \quad \mathbf{F}_1 = \frac{\mathrm{d}\boldsymbol{x}'}{\mathrm{d}\boldsymbol{X}} \quad \text{and} \quad \mathbf{F}_2 = \frac{\mathrm{d}\boldsymbol{x}}{\mathrm{d}\boldsymbol{x}'} \tag{2.5}$$

is considered. The tensors $\mathbf{F}_1, \mathbf{F}_2 \in \mathrm{GL}$ represent different deformation types. For instance, $\mathbf{F}_1$ and $\mathbf{F}_2$ can be the stretch and rigid rotation, i.e.,

$$\mathbf{F} = \mathbf{R} \cdot \mathbf{U} = \mathbf{V} \cdot \mathbf{R}, \tag{2.6}$$

where $\mathbf{R}$ represents an orthogonal rotation tensor and $\mathbf{U}$, $\mathbf{V}$ are symmetric positive-definite stretch tensors. Based on Eq. 2.6, strain measures can be defined independent of the rotation $\mathbf{R}$. Most of the frequently used strain

measures are of Hill-type, cf. Hill (1968). For example, the Green strain $\mathbf{E}$ of Lagrangian-type has the form

$$\mathbf{E} = \frac{1}{2}(\mathbf{U}^2 - \mathbf{I}) = \frac{1}{2}(\mathbf{F}^{\mathrm{T}} \cdot \mathbf{F} - \mathbf{I}), \tag{2.7}$$

where the term $\mathbf{F}^{\mathrm{T}} \cdot \mathbf{F}$ represents the right Cauchy-Green tensor $\mathbf{C}$. The true or logarithmic strain $\mathbf{H}$ also known as the Hencky strain of Lagrangian-type reads

$$\mathbf{H} = \ln(\mathbf{U}) = \frac{1}{2}\ln(\mathbf{F}^{\mathrm{T}} \cdot \mathbf{F}). \tag{2.8}$$

To further describe the kinematics, the rate of deformation (material derivative) is introduced. For example, applying the material derivative to the particle position vector $\boldsymbol{x}$ one obtains the particle velocity $\boldsymbol{v}$, which is written as

$$\boldsymbol{v} = \frac{\partial \boldsymbol{\varphi}}{\partial t}. \tag{2.9}$$

The spacial gradient of this particle velocity also called the velocity gradient $\boldsymbol{l}$ is then defined as

$$\boldsymbol{l} = \frac{\partial \boldsymbol{v}}{\partial \boldsymbol{x}} = \frac{\partial \boldsymbol{v}}{\partial \boldsymbol{X}} \cdot \frac{\partial \boldsymbol{X}}{\partial \boldsymbol{x}} = \dot{\mathbf{F}} \cdot \mathbf{F}^{-1}. \tag{2.10}$$

In general, this velocity gradient is not symmetric. However, as it is true for every second-order tensor, it can additively be split into symmetric $\boldsymbol{d}$ and skew-symmetric $\boldsymbol{\Omega}$ parts, i.e.,

$$\boldsymbol{l} = \boldsymbol{d} + \boldsymbol{\Omega} \tag{2.11}$$

where

$$\boldsymbol{d} = \frac{1}{2}(\boldsymbol{l} + \boldsymbol{l}^{\mathrm{T}}) \quad \text{and} \quad \boldsymbol{\Omega} = \frac{1}{2}(\boldsymbol{l} - \boldsymbol{l}^{\mathrm{T}}). \tag{2.12}$$

In Eq. 2.12, $\boldsymbol{d}$ represents the true rate of change of deformation and it is also referred to as stretching, whereas the spin tensor $\boldsymbol{\Omega}$ can be interpreted as a measure for the local angular velocity.

2.2 Balance laws

In addition to the kinematics, a proper description of the mechanics of a deforming body has to fulfill certain fundamental physical laws also known as balance laws. These are the conservation laws of mass, momentum and energy as well as the balance of entropy. In what follows, each of these laws is briefly discussed.

2.2.1 Conservation of mass

The conservation law of mass states that mass m

$$\mathrm{m} = \int_{\Omega} \rho_o \, \mathrm{d}V = \int_{\boldsymbol{\varphi}(\Omega)} \rho \, \mathrm{d}v = \int_{\boldsymbol{\varphi}(\Omega)} \mathrm{J} \, \rho \, \mathrm{d}V, \tag{2.13}$$

of a given material body Ω remains constant at all times, where ρ_o and ρ are the material density in the undeformed and deformed domain. This conservation law can then mathematically be expressed as

$$\dot{\mathrm{m}} = 0 \quad \Leftrightarrow \quad \dot{\rho_o} = \dot{\overline{\mathrm{J}\,\rho}} = 0. \tag{2.14}$$

2.2.2 Conservation of momentum

The conservation of momentum can be understood as the extension of Newton's laws of motion. In the following, the conservation of linear and angular momentum are introduced separately.

2.2.2.1 Conservation of linear momentum

Conservation of linear momentum is derived on the basis of Newton's second law. With the linear momentum of a body in motion defined as

$$I = \int_{\boldsymbol{\varphi}(\Omega)} \rho \, \boldsymbol{v} \, \mathrm{d}v, \tag{2.15}$$

the corresponding conservation law relates the rate of the linear momentum and the applied forces such that

$$\dot{I} = \int_{\boldsymbol{\varphi}(\Omega)} \rho \, \dot{\boldsymbol{v}} \, \mathrm{d}v = \int_{\boldsymbol{\varphi}(\Omega)} \rho \, \mathbf{b} \, \mathrm{d}v + \int_{\boldsymbol{\varphi}(\partial\Omega)} \mathbf{t} \, \mathrm{d}a. \tag{2.16}$$

In Eq. 2.16, $\mathbf{b}$ and $\mathbf{t}$ represent specific body forces and the surface tractions applied on the boundary $\boldsymbol{\varphi}(\partial\Omega_1) \subset \boldsymbol{\varphi}(\partial\Omega)$, while $\mathrm{d}a$ is the differential surface element of the body. Applying Cauchy's stress postulate, the traction can be redefined in terms of the Cauchy stress tensor $\boldsymbol{\sigma}$ and a normal vector $\mathbf{n}$ to $\boldsymbol{\varphi}(\partial\Omega_1)$, i.e.,

$$\mathbf{t} = \boldsymbol{\sigma} \cdot \mathbf{n}. \tag{2.17}$$

Inserting Eq. 2.17 in Eq. 2.16 and imposing the Gauss theorem, one can transform the global momentum conservation relation in Eq. 2.16 to a local form. In the absence of dynamic effects, the resulting relation reads

$$\mathrm{div}\boldsymbol{\sigma} + \rho\,\mathbf{b} = 0, \tag{2.18}$$

where the divergence div() is defined in Appendix A.

2.2.2.2 Conservation of linear momentum - weak form / Principle of virtual work

The weak form or the principle of virtual work is an equivalent formulation for the conservation of linear momentum. The derivation of this formulation involves the multiplication of the local form in Eq. 2.18 by a weighting function $\delta\mathbf{w}$ and integrating over the whole domain. The weighting function also referred to as virtual displacement is required to comply with the prescribed essential boundary conditions. As such, it should vanish at the boundary $\boldsymbol{\varphi}(\partial\Omega_2) = \boldsymbol{\varphi}(\partial\Omega)/\boldsymbol{\varphi}(\partial\Omega_1)$ where the deformation is prescribed. Thus, for a prescribed traction $\overline{\mathbf{t}} = \mathbf{t}|_{\boldsymbol{\varphi}(\partial\Omega_1)}$, applying the aforementioned modifications to Eq. 2.18 leads to

$$\int\limits_{\boldsymbol{\varphi}(\Omega)} \rho\,\delta\mathbf{w}\cdot\mathbf{b}\,\mathrm{d}v + \int\limits_{\boldsymbol{\varphi}(\Omega)} \delta\mathbf{w}\cdot\mathrm{div}\boldsymbol{\sigma}\,\mathrm{d}v + \int\limits_{\boldsymbol{\varphi}(\partial\Omega_1)} \delta\mathbf{w}\cdot(\overline{\mathbf{t}}-\mathbf{t})\,\mathrm{d}a = 0. \tag{2.19}$$

Imposing the Gauss theorem and assuming sufficient smoothness of $\delta\mathbf{w}$, Eq. 2.19 can be rewritten as

$$\int\limits_{\boldsymbol{\varphi}(\Omega)} \rho\,\delta\mathbf{w}\cdot\mathbf{b}\,\mathrm{d}v - \int\limits_{\boldsymbol{\varphi}(\Omega)} \boldsymbol{\sigma}:\mathrm{grad}(\delta\mathbf{w})\,\mathrm{d}v + \int\limits_{\boldsymbol{\varphi}(\partial\Omega_1)} \delta\mathbf{w}\cdot\overline{\mathbf{t}}\,\mathrm{d}a = 0, \tag{2.20}$$

where the gradient grad() is defined in Appendix A. The components in Eq. 2.20 are understood as the representations of the external virtual work δW_{ext} and internal virtual work δW_{int} where

$$\begin{aligned}
\delta W_{\mathrm{ext}} &= \int\limits_{\boldsymbol{\varphi}(\Omega)} \rho\,\delta\mathbf{w}\cdot\mathbf{b}\,\mathrm{d}v + \int\limits_{\boldsymbol{\varphi}(\partial\Omega_1)} \delta\mathbf{w}\cdot\overline{\mathbf{t}}\,\mathrm{d}a \\
\delta W_{\mathrm{int}} &= \int\limits_{\boldsymbol{\varphi}(\Omega)} \boldsymbol{\sigma}:\mathrm{grad}(\delta\mathbf{w})\,\mathrm{d}v.
\end{aligned} \tag{2.21}$$

Replacing the weighting function in Eq. 2.20 by a virtual displacement $\delta\mathbf{u}$ gives the standard virtual displacement work

$$\beth = \int\limits_{\boldsymbol{\varphi}(\Omega)} \rho\,\delta\mathbf{u}\cdot\mathbf{b}\,\mathrm{d}v - \int\limits_{\boldsymbol{\varphi}(\Omega)} \boldsymbol{\sigma}:\mathrm{grad}(\delta\mathbf{u})\,\mathrm{d}v + \int\limits_{\boldsymbol{\varphi}(\partial\Omega_1)} \delta\mathbf{u}\cdot\overline{\mathbf{t}}\,\mathrm{d}a = 0. \tag{2.22}$$

2.2.2.3 Conservation of angular momentum

Angular momentum of a given body $\boldsymbol{\varphi}(\Omega)$ measured with respect to a fixed origin is defined as

$$\int\limits_{\boldsymbol{\varphi}(\Omega)} \rho\, \boldsymbol{x} \times \boldsymbol{v}\, \mathrm{d}v, \tag{2.23}$$

where $\boldsymbol{x}$ is considered as the lever arm with respect to the origin. The conservation law then states that the rate of angular momentum for a given body $\boldsymbol{\varphi}(\Omega)$ equals the momentum of all external forces acting on it, i.e.,

$$\frac{\mathrm{d}}{\mathrm{d}t} \int\limits_{\boldsymbol{\varphi}(\Omega)} \rho\, \boldsymbol{x} \times \boldsymbol{v}\, \mathrm{d}v = \int\limits_{\boldsymbol{\varphi}(\Omega)} \rho\, \boldsymbol{x} \times \mathbf{b}\, \mathrm{d}v + \int\limits_{\boldsymbol{\varphi}(\partial\Omega)} \boldsymbol{x} \times \mathbf{t}\, \mathrm{d}a = 0. \tag{2.24}$$

Applying the Cauchy postulate to the second term on the right hand side of Eq. 2.24 and subsequent transformation into volume integral leads to the local form of the angular momentum

$$\boldsymbol{\sigma} = \boldsymbol{\sigma}^{\mathrm{T}}, \tag{2.25}$$

thus, establishing the symmetry of the Cauchy stresses.

2.2.3 Conservation of energy

The conservation of energy also known as the first law of thermodynamics states that the total energy of a closed system is conserved. In what follows, the internal energy U, heat energy Q and the energies due to externally applied forces A are considered. For a static process, the conservation law relates the rate forms of these energies, i.e.,

$$\dot{U} = \overset{\circ}{A} + \overset{\circ}{Q}. \tag{2.26}$$

In Eq. 2.26, $\dot{U}$ represents the internal power as a function of the specific internal power $\dot{u}$ and hence,

$$\dot{U} = \int\limits_{\boldsymbol{\varphi}(\Omega)} \rho\, \dot{u}\, \mathrm{d}v. \tag{2.27}$$

The power due to the applied forces $\overset{\circ}{A}$ reads

$$\overset{\circ}{A} = \int\limits_{\boldsymbol{\varphi}(\Omega)} \rho\, \mathbf{b} \cdot \boldsymbol{v}\, \mathrm{d}v + \int\limits_{\boldsymbol{\varphi}(\partial\Omega)} \boldsymbol{v} \cdot \mathbf{t}\, \mathrm{d}a. \tag{2.28}$$

Finally, the heat power is defined in terms of the contribution from heat source density r and the heat flux $\boldsymbol{q}$ flowing normal $\boldsymbol{n}$ to the boundary, i.e.,

$$\overset{\circ}{Q} = \int\limits_{\boldsymbol{\varphi}(\Omega)} \rho\, r \mathrm{d}v - \int\limits_{\boldsymbol{\varphi}(\partial\Omega)} \boldsymbol{q}\cdot\boldsymbol{n}\, \mathrm{d}a. \tag{2.29}$$

It should be noted that, unlike $\dot{U}$, the powers $\overset{\circ}{A}$, $\overset{\circ}{Q}$ are not necessarily the time derivatives of the corresponding energies. Thus, the resulting integrated powers are path-dependent in general.

For the derivation of the second law of thermodynamics, discussed in the next section, the local form

$$\rho\dot{u} = \boldsymbol{\sigma} : \boldsymbol{d} + \rho\, r - \mathrm{div}\boldsymbol{q} \tag{2.30}$$

of the conservation law is also introduced. This is achieved by transforming the surface integrals to volume integrals in Eq. 2.26 together with the conservation of linear momentum.

2.2.4 Balance of entropy

The balance of entropy or second law of thermodynamics states that the entropy s never decreases within a closed system. This is mathematically expressed as

$$\frac{\mathrm{d}}{\mathrm{d}t}\int\limits_{\boldsymbol{\varphi}(\Omega)} \rho\, s \mathrm{d}v \geq \int\limits_{\boldsymbol{\varphi}(\Omega)} \frac{\rho\, r}{\theta}\mathrm{d}v - \int\limits_{\boldsymbol{\varphi}(\partial\Omega)} \frac{\boldsymbol{q}\cdot\boldsymbol{n}}{\theta}\, \mathrm{d}a. \tag{2.31}$$

The equality case in Eq. 2.31 represents reversible processes, for instance, elasticity. Otherwise, the second law of thermodynamics determines the direction of energy transfer based on the level of entropy and the energy conservation law. The local form of the balance law can be written as

$$\rho\, \dot{s} - \frac{\rho\, r}{\theta} + \mathrm{div}\frac{\boldsymbol{q}}{\theta} \geq 0. \tag{2.32}$$

Specific to the application of continuum mechanics, the second law of thermodynamics is defined in terms of the Helmholtz energy Ψ. This law is also referred to as the Clausius-Duhem dissipation inequality. This inequality can be derived by introducing the Helmholtz energy of the form

$$\Psi = \inf_{s}\{u(\bullet, s) - \theta\, s\} \tag{2.33}$$

through a Legendre transformation. According to Eq. 2.33, the Helmholtz energy does not depend on the entropy. Therefore, by introducing the Helmholtz

energy and enforcing the conservation of linear momentum into Eq. 2.30, the second law of thermodynamics reads

$$\boldsymbol{\sigma} : \boldsymbol{d} - \rho \left(\dot{\Psi} + \dot{\theta}\, s \right) - \frac{\boldsymbol{q} \cdot \mathrm{grad}\theta}{\theta} \geq 0. \tag{2.34}$$

Imposing isothermal conditions, the Clausius-Duhem dissipation inequality reduces to

$$\mathcal{D} = \boldsymbol{\sigma} : \boldsymbol{d} - \rho\, \dot{\Psi} \geq 0, \tag{2.35}$$

where $\mathcal{D}$ represents the dissipation. Equivalently, the dissipation inequality can be expressed with respect to the undeformed domain such that

$$\mathcal{D} = \mathbf{P} : \dot{\mathbf{F}} - \rho_o\, \dot{\Psi} \geq 0, \tag{2.36}$$

where $\mathbf{P}$ represents the first Piola-Kirchhoff stress tensor.

The brief account on the kinematics and the governing equations presented in this chapter is applicable to any continuum provided the typical assumptions are fulfilled (for instance, Boltzman axiom, closed system, ...). However, this is insufficient to fully determine or solve the motion of a body. Consequently, the additional necessary conditions are established in terms of constitutive models in the next chapter.

3 Constitutive model

This chapter presents constitutive models for the determination of the material response, specifically for that of magnesium. In what follows, both reversible (elastic) and irreversible (plastic) processes are considered. For the reversible processes, hypoelastic and hyperelastic models are employed. For the irreversible processes, hyperelastoplastic and hypoelastoplastic models incorporating isotropic and distortional hardening are established. Concerning the hyperelastoplasticity, the respective models are derived in a thermodynamically consistent framework.

3.1 Elasticity

Elasticity is described as a reversible process. In this subsection, the two frequently applied theories to elasticity are briefly discussed. These are hyperelasticity and hypoelasticity. It should be noted that, despite its frequent use, hypoelasticity theory does not guarantee a non-dissipative response.

3.1.1 Hyperelasticity

According to hyperelasticity theory, elasticity is described as a path-independent process. Therefore, it can be represented by an elastic potential of the type $\psi(\mathbf{F})$, cf. Ciarlet (1988). In order to ensure the material frame indifference the potential can be defined as a function of $\mathbf{C}$, i.e., $\psi(\mathbf{C})$. Subsequently, the first Piola-Kirchhoff stress can be derived as

$$\mathbf{P} = \frac{\partial \psi}{\partial \mathbf{F}} = \frac{\partial \psi}{\partial \mathbf{C}} \bullet\circ \frac{\partial \mathbf{C}}{\partial \mathbf{F}} = 2\, \mathbf{F} \cdot \frac{\partial \psi}{\partial \mathbf{C}}, \tag{3.1}$$

where the nonstandard double contraction ($\bullet\circ$) is described in Appendix A. With $\mathbf{P}$ defined as a function of the second Piola-Kirchhoff stress tensor ($\mathbf{P} = \mathbf{F} \cdot \mathbf{S}$), a relation for $\mathbf{S}$ is established such that

$$\mathbf{S} = 2\, \frac{\partial \psi}{\partial \mathbf{C}}. \tag{3.2}$$

By inserting the stress power ($\mathbf{P}\colon\dot{\mathbf{F}}$)

$$\dot{\psi} = \mathbf{P}\colon\dot{\mathbf{F}} = \rho_o\ \dot{\Psi}. \tag{3.3}$$

into the dissipation inequality Eq. 2.36, a relation for the elastic potential can be established in terms of the Helmholtz free energy, i.e.,

$$\psi = \rho_o\ \Psi. \tag{3.4}$$

Therefore, elasticity is completely described by the Helmholtz free energy. A number of explicit definitions for the Helmholtz free energy have been proposed, see (Ogden, 1984; Ciarlet, 1988). In this work, the Neo-Hookean energy function

$$\Psi = \Psi(\mathbf{C}) = \frac{\lambda}{4}\left(\mathrm{J}^2 - 1\right) - \left(\frac{\lambda}{2} + \mu\right)\ln \mathrm{J} + \frac{\mu}{2}\left(\mathrm{tr}\mathbf{C} - 3\right) \tag{3.5}$$

is adopted, where λ, μ represent the Lam*é* parameters. This energy implies zero stresses and strain energy in the undeformed state. Furthermore, the energy converges to infinity, if the volume of the body approaches infinity or zero, as required by physics.

3.1.2 Hypoelasticity

The hypoelasticity theory establishes a relation between an objective rate of the Cauchy stress $\overset{\circ}{\boldsymbol{\sigma}}$ and the stretching tensor $\boldsymbol{d}$ via a fourth-order moduli tensor $\mathbb{C}$, cf. Truesdell (1955), i.e.

$$\overset{\circ}{\boldsymbol{\sigma}} = \mathbb{C}\colon\boldsymbol{d}. \tag{3.6}$$

Unlike hyperelasticity, the above ad hoc relation does not guarantee the path-independence of the stress response and the resulting work. Thus, in general sense, the second law of thermodynamics is not fulfilled. In cases where the elastic deformation is small, this inconsistency is, however, not pronounced. For such cases its application can be allowed.

3.2 Elastoplasticity

In contrast to elasticity, plasticity is characterized by a permanent deformation and a nonvanishing dissipation. Processes involving plastic deformation are often coupled with elastic deformation. For instance, the sheet forming processes dealt in this work undergo a coupled elastoplastic deformation. As such, these processes are described by the so-called elastoplasticity theories. In the present section, the underlying kinematics associated with elastoplasticity are discussed first. Subsequently, the respective constitutive assumptions are addressed.

3.2.1 Kinematical assumptions

In this subsection, two of the most commonly employed kinematical assumptions are presented. The first assumption decomposes additively the stretching tensor into the elastic $\boldsymbol{d}^{\mathrm{e}}$ and plastic $\boldsymbol{d}^{\mathrm{pl}}$ components, i.e.,

$$\boldsymbol{d} = \boldsymbol{d}^{\mathrm{e}} + \boldsymbol{d}^{\mathrm{pl}}. \tag{3.7}$$

For instance, this assumption is employed in the classical Eulerian rate formulations, cf. Truesdell (1955). The second assumption is advocated by Lee & Liu (1967). This method introduces an intermediate stress free state giving rise to the so-called multiplicative decomposition of the deformation gradient into elastic $\mathbf{F}^{\mathrm{e}}$ and plastic $\mathbf{F}^{\mathrm{pl}}$ components, such that

$$\mathbf{F} = \mathbf{F}^{\mathrm{e}} \cdot \mathbf{F}^{\mathrm{pl}}. \tag{3.8}$$

A detailed account of the aforementioned assumptions can be found in Xiao et al. (2006), see also Fig. 2.1.

3.2.2 Constitutive assumptions

One possible classification of constitutive models for plastic deformation is provided by the length scale of the models. For instance, the underlying physical features contributing to plasticity are understood to originate from dislocation slip and twinning during deformation within a micro-mechanical description. These micro-mechanical processes are also responsible for the hardening or softening behavior and dissipation observed. However, when dealing with problems at the macro-scale, accounting for all physical features at the micro-level can be a tedious and complicated task. For such applications, the so-called phenomenological theories are advantageous. These theories are established based on hypotheses and assumptions corresponding to macro-mechanical observations without direct regard to the physical features at micro-level. In this work, only phenomenological theories have been considered. With the special attention to magnesium, the hardening and dissipation describing plasticity are represented by mathematical formulations of the stored and dissipated energies in the following subsections.

3.2.2.1 Stored energy

The hardening behavior observed during plastic deformation can be described by a set of strain-like internal variables, such as those corresponding to isotropic α and distortional $\mathbb{E}$ hardening. Here, isotropic hardening is understood as an isotropic expansion of the yield surface, whereas, the distortional hardening

represents all remaining transformations of the yield surface caused by plastic deformation, for instance, change in shape of the yield locus. With such assumptions, the Helmholtz energy Ψ reads

$$\Psi = \Psi(\mathbf{C}^{\mathrm{e}}, \alpha, \mathbb{E}), \tag{3.9}$$

where $\mathbf{C}^{\mathrm{e}} = \mathbf{F}^{\mathrm{e}\mathrm{T}} \cdot \mathbf{F}^{\mathrm{e}}$ is the elastic part of the right Cauchy-Green tensor $\mathbf{C}$. Assuming an additive decomposition of the elastic and plastic response, the stored energy can be split as

$$\Psi = \Psi^{\mathrm{e}}(\mathbf{C}^{\mathrm{e}}) + \Psi^{\mathrm{pl}}(\alpha, \mathbb{E}). \tag{3.10}$$

The plastic stored energy is further assumed to be decoupled on the basis of the different hardening components, such as the isotropic Ψ^{iso} and distortional Ψ^{dis} hardening, i.e.,

$$\Psi^{\mathrm{pl}} = \Psi^{\mathrm{iso}}(\alpha) + \Psi^{\mathrm{dis}}(\mathbb{E}). \tag{3.11}$$

According to the work conjugacy definition, the strain-like internal variables are related to their conjugate stress-like counterparts, cf. Chaboche et al. (1979). Mathematically, the conjugate relation can be expressed as

$$\tau = -\frac{\partial \Psi^{\mathrm{iso}}}{\partial \alpha} \quad \text{and} \quad \mathbb{H} = -\frac{\partial \Psi^{\mathrm{dis}}}{\partial \mathbb{E}}, \tag{3.12}$$

where $\mathbb{H}$ and τ are the stress-like internal variables conjugate to $\mathbb{E}$ and α, respectively. In this work, the explicit definitions for the stored energy functions are established assuming a simple isotropic function, as proposed by Dafalias et al. (2003). As such, Ψ^{iso} and Ψ^{dis} take the forms

$$\Psi^{\mathrm{iso}} = 1/2\ h_{\mathrm{iso}}\ \alpha^2 \quad \text{and} \quad \Psi^{\mathrm{dis}} = 1/2\ h_{\mathrm{d}}\ \mathbb{E} \colon \colon \mathbb{E}, \tag{3.13}$$

where h_{iso} and h_{d} are the hardening moduli. In the final model, an exponential isotropic hardening is realized through a non-linear relation between α and the equivalent plastic strain (see Eq. 3.35). Subsequently, the conjugacy relation in Eq. 3.12 can be written as

$$\tau = -h_{\mathrm{iso}}\ \alpha \quad \text{and} \quad \mathbb{H} = -h_{\mathrm{d}}\ \mathbb{E}. \tag{3.14}$$

3.2.2.2 Dissipation

Following the definitions for the stored energies in the previous subsection, the dissipation caused by plastic deformation is quantified based on the Clausius-Duhem dissipation inequality

$$\mathcal{D} = \frac{1}{2}\ \mathbf{S} \colon \dot{\mathbf{C}} - \dot{\Psi} \geq 0. \tag{3.15}$$

Subsequently, expanding the rate form of $\mathbf{C}$ and Ψ into elastic and plastic components by considering the multiplicative split of $\mathbf{F}$ (see Eq. 3.8) leads to the expression

$$\mathcal{D} = \left(\frac{1}{2}\, \mathbf{F}^{\mathrm{pl}} \cdot \mathbf{S} \cdot \mathbf{F}^{\mathrm{pl}\,\mathrm{T}} - \partial_{\mathbf{C}^{\mathrm{e}}} \Psi^{\mathrm{e}} \right) : \dot{\mathbf{C}}^{\mathrm{e}} + \mathbf{S} : \left(\mathbf{F}^{\mathrm{pl}\,\mathrm{T}} \cdot \mathbf{C}^{\mathrm{e}} \cdot \dot{\mathbf{F}}^{\mathrm{pl}} \right) - \dot{\Psi}^{\mathrm{pl}} \geq 0, \quad (3.16)$$

where, the first part is related to the elastic strain rate and the second to plastic deformation. Due to the non-dissipative nature of elasticity, the relation

$$\mathbf{F}^{\mathrm{pl}} \cdot \mathbf{S} \cdot \mathbf{F}^{\mathrm{pl}\,\mathrm{T}} = 2\, \partial_{\mathbf{C}^{\mathrm{e}}} \Psi^{\mathrm{e}} \quad (3.17)$$

is obtained. From Eq. 3.17, it can be seen that the stress field in the intermediate configuration $\mathbf{S}^{\mathrm{e}} = 2\, \partial_{\mathbf{C}^{\mathrm{e}}} \Psi^{\mathrm{e}}$ is related to the stress in the reference configuration $\mathbf{S}$ through a push-forward operation. Furthermore, the reduced dissipation inequality can be written as

$$\mathcal{D} = \boldsymbol{\Sigma} : \mathbf{L}^{\mathrm{pl}} + \dot{\Psi}^{\mathrm{pl}} \geq 0, \quad (3.18)$$

where $\boldsymbol{\Sigma} = 2\, \mathbf{C}^{\mathrm{e}} \cdot \partial_{\boldsymbol{C}^{\mathrm{e}}} \Psi$ is the Mandel stress, which is work conjugate to the plastic part of the velocity gradient $\mathbf{L}^{\mathrm{pl}} = \dot{\mathbf{F}}^{\mathrm{pl}} \cdot \mathbf{F}^{\mathrm{pl}\,-1}$. Applying the chain rule to $\dot{\Psi}^{\mathrm{pl}}$, one obtains

$$\dot{\Psi}^{\mathrm{pl}} = \frac{\partial \Psi^{\mathrm{dis}}}{\partial \mathbb{E}} : : \dot{\mathbb{E}} + \frac{\partial \Psi^{\mathrm{iso}}}{\partial \alpha}\, \dot{\alpha}. \quad (3.19)$$

Moreover, imposing the work conjugacy, $\dot{\Psi}^{\mathrm{pl}}$ takes the form

$$\dot{\Psi}^{\mathrm{pl}} = -\mathbb{H} : : \dot{\mathbb{E}} - \tau\, \dot{\alpha}. \quad (3.20)$$

A complete description of the dissipation relation requires the rate or evolution equations of the strain-like quantities $\mathbf{L}^{\mathrm{pl}}$, $\dot{\mathbb{E}}$ and $\dot{\alpha}$. For that purpose, the flow rule and hardening laws are introduced. By introducing a convex plastic potential g, such laws are assumed to be of the type

$$\mathbf{L}^{\mathrm{pl}} = \dot{\lambda} \frac{\partial g}{\partial \boldsymbol{\Sigma}} \qquad \dot{\mathbb{E}} = \dot{\lambda}\, \frac{\partial g}{\partial \mathbb{H}} \qquad \dot{\alpha} = \dot{\lambda}\, \frac{\partial g}{\partial \tau}, \quad (3.21)$$

with $\dot{\lambda}$ being the plastic multiplier. For checking whether the respective deformation is elastic (where $\dot{\lambda} = 0$) or plastic, the space of admissible stresses is defined by a yield function f. More precisely,

$$f(\boldsymbol{\Sigma}, \mathbb{H}, \tau) \leq 0. \quad (3.22)$$

For $f < 0$, the yield function defines the stress domain for fully elastic states. The equality relation in Eq. 3.22 is the necessary condition for a plastic state.

The yield condition is complemented by the so-called Karush-Kuhn-Tucker conditions, which read

$$\dot{\lambda} f = 0 \qquad \text{and} \quad \dot{\lambda} \geq 0, \tag{3.23}$$

together with the consistency condition expressed as

$$\dot{\lambda} \dot{f} = 0 \tag{3.24}$$

which allows computing the plastic multiplier. The yield function has to be convex to guarantee material stability, cf. Drucker (1964). Substituting the plastic potential by the yield function in Eq. 3.21, the associated flow rule

$$\mathbf{L}^{\mathrm{pl}} = \dot{\lambda} \frac{\partial f}{\partial \boldsymbol{\Sigma}} \qquad \dot{\mathbb{E}} = \dot{\lambda} \, \frac{\partial f}{\partial \mathbb{H}} \qquad \dot{\alpha} = \dot{\lambda} \, \frac{\partial f}{\partial \tau}, \tag{3.25}$$

is obtained. An explicit definition of the yield function is presented in the following subsection.

3.2.2.3 Yield function

Over the years, several authors proposed a number of yield functions corresponding to different materials exhibiting isotropic and anisotropic behavior. For instance, von Mises proposed the first yield function for anisotropic materials in the form of a quadratic function, cf. von Mises (1928). The modification of this model, also one of the most commonly used models in commercial codes to-date, was later introduced by Hill for the application to orthotropic materials, cf. Hill (1948). Additionally, a number of versatile anisotropic models was introduced in (Hill, 1990; Karafillis & Boyce, 1993; Cazacu & Barlat, 2001). These models, however, make no distinction between in-plane tension and compression loadings. In other words tension and compression responses of the yield function are assumed to be same. This assumption is not true for some metals, for example, magnesium. Such phenomenon is considered in a model introduced by Hosford, as a modification of the Hill model by adding linear stress terms, cf. Hosford (1966). Although this model correctly describes the tension and compression response mismatch, it is not suitable for materials exhibiting strong yield loci asymmetry. Cazacu & Barlat introduced a higher-order yield function (CaBa2004) as a modification of the Drucker model, having the capability to account for a strong yield loci asymmetry as well as tension-compression asymmetry, cf. (Drucker, 1949; Cazacu & Barlat, 2004). The formulation of CaBa2004 is based on the generalized forms of the second and third invariants of the deviatoric stress tensor $\mathrm{J}_2^{\mathrm{o}}$ and $\mathrm{J}_3^{\mathrm{o}}$, respectively. Such invariants can be written as

$$\mathrm{J}_2^{\mathrm{o}}(\boldsymbol{\Sigma}, a_i) \qquad \text{and} \qquad \mathrm{J}_3^{\mathrm{o}}(\boldsymbol{\Sigma}, b_j), \tag{3.26}$$

where a_i and b_j with $i = \{1, ..., 6\}$ and $j = \{1, ..., 11\}$ are the model constants associated with the initial anisotropy of the yield function. For $a_i = 1$ and $b_i = 1$, these invariants are identical to the standard invariants.

The yield function presented in this work is based on CaBa2004. That is, the current model adopts the same order of function, accounts for material anisotropy as well as tension-compression asymmetry. However, it is rewritten here in tensor notation. For that purpose, fourth-order transformation tensors $\mathbb{H}_1$ and $\mathbb{H}_2$ associated with the distortion of the yield locus are introduced. Even more important and different to CaBa2004, such tensors are not constant here, but evolve according to suitable evolution equations. By doing so, the distortional hardening effect (change in shape of the yield locus) can be taken into account. The properties of these tensors as well as the relation of the respective components to the model parameters of the CaBa2004 model are detailed in Section 8.2.1. With the fourth-order transformation tensors, the modified invariants can be written as

$$\mathrm{J}_2^{\mathrm{o}} = \frac{1}{2}\,\mathrm{tr}(\overline{\boldsymbol{\Sigma}}_{\mathbf{1}} \cdot \overline{\boldsymbol{\Sigma}}_{\mathbf{1}}) \qquad \text{and} \qquad \mathrm{J}_3^{\mathrm{o}} = \frac{1}{3}\,\mathrm{tr}(\overline{\boldsymbol{\Sigma}}_{\mathbf{2}} \cdot \overline{\boldsymbol{\Sigma}}_{\mathbf{2}} \cdot \overline{\boldsymbol{\Sigma}}_{\mathbf{2}}), \tag{3.27}$$

where $\overline{\boldsymbol{\Sigma}}_i = \mathbb{H}_i : \boldsymbol{\Sigma}$ with $i = \{1, 2\}$ are the transformed stress tensors corresponding to the second and the third invariants. The yield function f, thus, reads

$$f = \phi(\overline{\boldsymbol{\Sigma}}_i) - \mathrm{h}(\tau) - \mathrm{h}_{\mathrm{o}} \quad \text{with} \quad \phi = \mathrm{J}_2^{\mathrm{o}\,3/2} - \mathrm{J}_3^{\mathrm{o}} \quad \text{and} \quad \mathrm{h} = \tau^3, \tag{3.28}$$

where $\mathrm{h}(\tau)$ and h_{o} represent quantities related to the isotropic hardening and initial yield limit, respectively.

It is worth mentioning that the defined yield function is a homogeneous function of order three in $\boldsymbol{\Sigma}$ and τ. Therefore, substituting the explicit definition of the yield function into the evolution equations Eq 3.25, the dissipation inequality for associative plastic flow reduces from

$$\mathcal{D} = \dot{\lambda}\, \boldsymbol{\Sigma} : \frac{\partial f}{\partial \boldsymbol{\Sigma}} + \dot{\lambda}\, \mathbb{H} :: \frac{\partial f}{\partial \mathbb{H}} + \dot{\lambda}\, \tau\, \frac{\partial f}{\partial \tau} \geq 0 \tag{3.29}$$

to

$$\mathcal{D} = \underbrace{3\, \dot{\lambda}\, \mathrm{h}_{\mathrm{o}}}_{>0} + \dot{\lambda}\, \mathbb{H} :: \frac{\partial f}{\partial \mathbb{H}} \geq 0. \tag{3.30}$$

The two terms in Eq 3.30 are associated with the isotropic and distortional hardening, respectively. Requiring these terms to satisfy a positive dissipation, separately, leads to a sufficient but not necessary condition. Thus, according to Eq. 3.30, imposing the condition

$$\mathcal{D} = \dot{\lambda}\, \mathbb{H} :: \frac{\partial f}{\partial \mathbb{H}} \geq 0, \tag{3.31}$$

is sufficient to ensure a nonnegative dissipation. Assuming additionally

$$\mathbb{E} = \mathbb{E}(\overline{\varepsilon}^{\mathrm{pl}}), \tag{3.32}$$

see (Dafalias, 1979; Graff, 2007), the dissipation relation can further be simplified to

$$\mathcal{D} = \mathbb{H} : : \frac{\partial \mathbb{E}(\overline{\varepsilon}^{\mathrm{pl}})}{\partial \overline{\varepsilon}^{\mathrm{pl}}} \dot{\overline{\varepsilon}}^{\mathrm{pl}} \geq 0, \tag{3.33}$$

where the equivalent plastic strain $\overline{\varepsilon}^{\mathrm{pl}}$ is interpreted as a representation of the plastic deformation by a single scalar quantity, see Odqvist (1933). Its rate form $\dot{\overline{\varepsilon}}^{\mathrm{pl}}$ can be defined in terms of $\mathbf{L}^{\mathrm{pl}}$ such that

$$\dot{\overline{\varepsilon}}^{\mathrm{pl}} = \sqrt{\mathbf{L}^{\mathrm{pl}} : \mathbf{L}^{\mathrm{pl}}}. \tag{3.34}$$

Hence, the equivalent plastic strain is obtained by integrating Eq 3.34 over the period of the plastic deformation. Furthermore, the internal variable of the isotropic hardening is assumed to exclusively depend on $\overline{\varepsilon}^{\mathrm{pl}}$. As such, a saturating exponential function of the form

$$\alpha = -\Big(1 - \exp(\zeta\, \overline{\varepsilon}^{\mathrm{pl}})\Big), \tag{3.35}$$

is adopted, where ζ is a model parameter determined based on experimental measurements.

Remark 1 *The fulfillment of the principle of material frame indifference lacking in the original model of Cazacu and Barlat is resolved in the current model by the tensorial reformulation in terms of Mandel stresses.*

Remark 2 *In the current model, convexity of the yield function, which is required for the thermodynamic consistency, is not automatically satisfied. This issue is addressed by constraining the model parameters accordingly.*

Remark 3 *A strain rate effect is also included within the model by using a power law-type function,*

$$\alpha = \alpha^{\mathrm{ref}} \left(\frac{\dot{\overline{\varepsilon}}^{\mathrm{pl}}}{\beta} \right)^{n}, \tag{3.36}$$

where α^{ref} represents the strain hardening at a reference strain rate while β and n are model parameters determined based on experimental measurements.

Remark 4 *In addition to the presented hyperelastoplastic constitutive model, its hypoelastoplastic counterpart as briefly discussed in Subsection 3.1.2 is also used within the present thesis. Further details on such a formulation can be found, for instance, in Xiao et al. (2006).*

4 Numerical implementation

The current chapter presents the numerical implementation and verification of the constitutive model developed in the previous chapter. This implementation is performed within the finite element framework following the principle of virtual work introduced in Subsection 2.2.2.2. As such, the user material subroutine (UMAT) interface provided by the commercial finite element program ABAQUS® is employed. A detailed account on the numerical implementations of constitutive models can be found in Simo & Hughes (1998).

4.1 The finite element framework

The purely mechanical and quasi-static equilibrium of a body undergoing deformation is represented by the principle of virtual work defined in Eq 2.22. The numerical solution of this equilibrium relation involves discretization with respect to space and time. In the present work, the spacial discretization is achieved by applying the finite element method. Regardless of the considered discretization method, a system of nonlinear equations is finally obtained. Such equations can be solved by employing a Newton-Raphson scheme. Thus, an approximation for the virtual work at the current time $(t + \Delta t)$ such that

$$\mathfrak{I}(\mathbf{u}_{t+\Delta t}) \approx \mathfrak{I}(\mathbf{u}_t) + \frac{\partial \mathfrak{I}(\mathbf{u})}{\partial \mathbf{u}}|_t \; \Delta \mathbf{u}_t = 0 \tag{4.1}$$

is used, (see Eq. 2.22). Having solved Eq. 4.1, the displacement field at the current time $\mathbf{u}_{t+\Delta t}$ is computed by the relation

$$\mathbf{u}_{t+\Delta t} \approx \mathbf{u}_t^{i+1} = \mathbf{u}_t^i + \Delta \mathbf{u}_t^{i+1}. \tag{4.2}$$

The solution is accepted if the residual of Eq 4.1 converges to zero or if a prescribed tolerance criterion is met. Otherwise, an additional iteration step is required.

Within the finite element framework, solving the equilibrium relation requires the local state variables, such as the stress-like quantities and the plastic strain. These local state variables are obtained through the constitutive relations discussed in the previous chapter. It is worth mentioning that for a displacement

driven analysis, the finite element solver in ABAQUS® provides the total deformation and/or strain at previous (t) and current ($t + \Delta t$) time. In return, the solver requires the updated stress field and tangent operator for a given material point.

4.2 Numerical implementation of the constitutive models

The numerical solution of an elastoplastic problem requires employing an integration scheme for the evolution equations defined in Eq. 3.25. Furthermore, an operator split technique for decoupling the problem into fully elastic predictor and elastoplastic corrector steps is frequently adopted. For the integration, the backward Euler integration scheme is applied. In the following, details about the aforementioned predictor and corrector steps are presented.

4.2.1 Predictor step

For a given incremental deformation, the assumption of a fully elastic problem implies that the plastic deformation at the current state should be the same as that at the previous step, i.e.,

$$\mathbf{F}^{\mathrm{pl}}_{t+\Delta t} = \mathbf{F}^{\mathrm{pl}}_{t}. \tag{4.3}$$

Thus, the equivalent plastic strain at the current state remains unchanged, i.e.,

$$\overline{\varepsilon}^{\mathrm{pl}}_{t+\Delta t} = \overline{\varepsilon}^{\mathrm{pl}}_{t}. \tag{4.4}$$

The hardening terms, which are redefined to depend only on the equivalent plastic strain according to Eq. 3.32 and Eq. 3.35 also take the values at the previous time. Consequently,

$$\begin{array}{rcccl} \mathbb{H}_{t+\Delta t} & = & \mathbb{H}_{t} & = & \mathbb{H}(\overline{\varepsilon}^{\mathrm{pl}}_{t}) \\ \tau_{t+\Delta t} & = & \tau_{t} & = & \tau(\overline{\varepsilon}^{\mathrm{pl}}_{t}) \end{array}. \tag{4.5}$$

Moreover, the elastic deformation at the current state is computed based on the multiplicative split of the deformation gradient in Eq 3.8 such that

$$\mathbf{F}^{\mathrm{e}}_{t+\Delta t} = \mathbf{F}_{t+\Delta t} \cdot {\mathbf{F}^{\mathrm{pl}}_{t}}^{-1}. \tag{4.6}$$

The corresponding Mandel stresses in the intermediate configuration are computed as

$$\mathbf{\Sigma}_{t+\Delta t} = 2\, \mathbf{C}^{\mathrm{e}}_{t+\Delta t} \cdot \partial_{\mathbf{C}^{\mathrm{e}}} \Psi|_{\mathbf{C}^{\mathrm{e}}_{t+\Delta t}} = \lambda \frac{\mathrm{J}^2 - 1}{2}\, \mathbf{I} + \mu\, (\mathbf{C}^{\mathrm{e}}_{t+\Delta t} - \mathbf{I}). \tag{4.7}$$

Here, the elastic response as implied by Eq. 3.5 has been assumed. Since the ABAQUS® solver requires the Cauchy stress, a push-forward is applied to $\boldsymbol{\Sigma}_{t+\Delta t}$, which reads

$$\boldsymbol{\sigma}_{t+\Delta t} = \frac{1}{\mathrm{J}} \left[\mathbf{F}^{\mathrm{e}}_{t+\Delta t} \cdot \left(\mathbf{C}^{\mathrm{e}\,-1}_{t+\Delta t} \cdot \boldsymbol{\Sigma}_{t+\Delta t} \right) \cdot \mathbf{F}^{\mathrm{e}\,\mathrm{T}}_{t+\Delta t} \right]. \tag{4.8}$$

Having computed the stress field and the hardening terms, the yield function is evaluated. If

$$f(\boldsymbol{\Sigma}_{t+\Delta t}, \mathbb{H}_{t+\Delta t}, \tau_{t+\Delta t}) \leq 0, \tag{4.9}$$

the assumption of a fully elastic load step holds and the trial quantities are accepted. Otherwise, the problem is incrementally plastic. Thus, a corrector step is required.

4.2.2 Corrector step

If Eq. 4.9 is not fulfilled, an algorithm for solving an incrementally plastic problem characterized by the relation

$$f(\boldsymbol{\Sigma}_{t+\Delta t}, \mathbb{H}_{t+\Delta t}, \tau_{t+\Delta t}) = 0 \tag{4.10}$$

is employed. For that purpose, the return-mapping algorithm is adopted. This algorithm iteratively corrects the trial stress-like quantities while satisfying the Karush-Kuhn-Tucker conditions. Within this scheme, the normal tensor $\mathbf{N} := \partial_{\boldsymbol{\Sigma}} f$ to the yield surface and the plastic multiplier increment $\Delta\lambda$ are chosen as the unknowns. For instance, the plastic deformation gradient at the current time is computed from the exponential integration scheme of the evolution equation in Eq 3.21, i.e.,

$$\mathbf{F}^{\mathrm{pl}}_{t+\Delta t} = \exp\left(\Delta\lambda\, \mathbf{N}_{t+\Delta t}\right) \cdot \mathbf{F}^{\mathrm{pl}}_{t}. \tag{4.11}$$

The use of the exponential-type integration ensures the isochoric constraints as implied by the underlying flow rule. Applying the multiplicative split, the elastic deformation gradient at the current state reads

$$\mathbf{F}^{\mathrm{e}}_{t+\Delta t} = \mathbf{F}_{t+\Delta t} \cdot {\mathbf{F}^{\mathrm{pl}}_{t+\Delta t}}^{-1}. \tag{4.12}$$

Within the scope of the return-mapping algorithm, the total deformation gradient is constant, hence, $\Delta\mathbf{F} = 0$. Thus, the stress can be described as a function of only the two chosen unknowns, i.e.,

$$\boldsymbol{\Sigma}_{t+\Delta t}(\mathbf{C}^{\mathrm{e}}_{t+\Delta t}) = \boldsymbol{\Sigma}(\Delta\lambda, \mathbf{N}_{t+\Delta t}). \tag{4.13}$$

For reformulating the stress-like quantities related to hardening, the equivalent plastic strain is computed by integrating the relation in Eq 3.34 such that

$$\overline{\varepsilon}^{\mathrm{pl}}_{t+\Delta t} = \overline{\varepsilon}^{\mathrm{pl}}_{t} + \Delta\lambda \sqrt{\mathbf{N}_{t+\Delta t} \colon \mathbf{N}_{t+\Delta t}}. \tag{4.14}$$

Thus, the yield function is described in terms of $\mathbf{N}$ and $\Delta\lambda$, i.e.,

$$f(\boldsymbol{\Sigma}_{t+\Delta t}, \mathbb{H}_{t+\Delta t}, \tau_{t+\Delta t}) = f(\mathbf{N}_{t+\Delta t}, \Delta\lambda) = 0. \tag{4.15}$$

A correct flow direction is enforced by the nonlinear equation

$$\mathbf{N}_{t+\Delta t} - \partial_{\boldsymbol{\Sigma}} f = 0. \tag{4.16}$$

The residuals

$$\begin{array}{lcl} \mathbf{R}_1 & := & \mathbf{N}_{t+\Delta t} - \partial_{\boldsymbol{\Sigma}} f \\ \mathrm{R}_2 & := & f \end{array} \tag{4.17}$$

are taken to be target functions for the return-mapping algorithm. For solving the nonlinear equations in Eq 4.17, a Newton-type method is adopted. Hence, the linearization with respect to $\Delta\lambda$ and $\mathbf{N}$ is necessary. Mathematically stated, this linearization gives the relations

$$\begin{array}{rclcl} \mathrm{d}\mathbf{R}_1 & = & \partial_{\mathbf{N}}\mathbf{R}_1 \bullet\circ \mathrm{d}\mathbf{N} + \partial_{\Delta\lambda}\mathbf{R}_1 \, \mathrm{d}\Delta\lambda & = & -\,\mathbf{R}_1 \\ \mathrm{dR}_2 & = & \partial_{\mathbf{N}}\mathrm{R}_2 \colon \mathrm{d}\mathbf{N} + \partial_{\Delta\lambda}\mathrm{R}_2 \, \mathrm{d}\Delta\lambda & = & -\,\mathrm{R}_2, \end{array} \tag{4.18}$$

where the nonstandard double contraction ($\bullet\circ$) is described in Appendix A. The components in Eq. 4.18 are defined as

$$\begin{array}{rclcrcl} \partial_{\mathbf{N}}\mathbf{R}_1 & = & (\mathbf{I}\otimes\mathbf{I}) - \dfrac{\partial^2 f}{\partial\boldsymbol{\Sigma}\partial\mathbf{N}} & , & \partial_{\mathbf{N}}\mathrm{R}_2 & = & \partial_{\mathbf{N}} f \\ \partial_{\Delta\lambda}\mathbf{R}_1 & = & -\,\dfrac{\partial^2 f}{\partial\boldsymbol{\Sigma}\partial\Delta\lambda} & , & \partial_{\Delta\lambda}\mathrm{R}_2 & = & \partial_{\Delta\lambda} f. \end{array} \tag{4.19}$$

The derivations of $\frac{\partial^2 f}{\partial\boldsymbol{\Sigma}\partial\mathbf{N}}$, $\frac{\partial^2 f}{\partial\boldsymbol{\Sigma}\partial\Delta\lambda}$, $\partial_{\mathbf{N}} f$ and $\partial_{\Delta\lambda} f$ used in Eq 4.19 are presented in Appendix B. For the initial conditions of the Newton-type iteration,

$$\begin{array}{lcl} \mathbf{N}^{\circ}_{t+\Delta t} & := & \partial_{\boldsymbol{\Sigma}} f|_{\{\boldsymbol{\Sigma}_{\mathrm{trial}}, \mathbb{H}_t, \tau_t\}} \\ \Delta\lambda^{\circ} & := & 0. \end{array} \tag{4.20}$$

is assumed. The increments $\mathrm{d}\mathbf{N}$ and $\mathrm{d}\Delta\lambda$ can be computed from Eq. 4.18 by a substitution procedure, i.e.,

$$\begin{array}{rcl} \mathrm{d}\Delta\lambda & = & \dfrac{-\mathrm{R}_2 + \partial_{\mathbf{N}}\mathrm{R}_2 \colon \left((\partial_{\mathbf{N}}\mathbf{R}_1)^{-1} \bullet\circ \mathbf{R}_1 \right)}{\partial_{\Delta\lambda}\mathrm{R}_2 - \partial_{\mathbf{N}}\mathrm{R}_2 \bullet\circ (\partial_{\mathbf{N}}\mathbf{R}_1)^{-1} \bullet\circ \partial_{\Delta\lambda}\mathbf{R}_1} \\ \mathrm{d}\mathbf{N} & = & -\left(\partial_{\mathbf{N}}\mathbf{R}_1\right)^{-1} \bullet\circ \left[\partial_{\Delta\lambda}\mathbf{R}_1 \, \mathrm{d}\Delta\lambda + \mathbf{R}_1\right], \end{array} \tag{4.21}$$

and the respective updates of the unknowns are given by $\mathbf{N}$ and $\Delta\lambda$,

$$\begin{aligned} \mathbf{N}_{t+\Delta t}^{j+1} &= \mathbf{N}_{t+\Delta t}^{j} + \mathrm{d}\mathbf{N} \\ \Delta\lambda^{j+1} &= \Delta\lambda^{j} + \mathrm{d}\Delta\lambda, \end{aligned} \tag{4.22}$$

where the superscript j represents the local iteration step. This update is repeated until the residuals (Eq. 4.17) converge to an acceptable tolerance. Once the local convergence is obtained, attention is turned to the derivation of the tangent operator necessary for an asymptotically quadratic convergence at the structural level.

4.2.3 Tangent operator

The derivation of the algorithmic tangent operator is of great importance for the global convergence of the overriding finite element framework. The material description of the tangent operator is defined as

$$\mathbb{C} = 2\frac{\mathrm{d}\mathbf{S}}{\mathrm{d}\mathbf{C}}. \tag{4.23}$$

With Eq 3.17, Eq. 4.23 can be expanded to

$$\frac{\mathrm{d}\mathbf{S}}{\mathrm{d}\mathbf{C}} = \left(\partial_{\mathbf{C}^{\mathrm{e}}}\mathbf{S} \bullet\circ \partial_{\mathbf{F}^{\mathrm{pl}}}\mathbf{C}^{\mathrm{e}} + \partial_{\mathbf{F}^{\mathrm{pl}}}\mathbf{S}\right) \bullet\circ \frac{\mathrm{d}\mathbf{F}^{\mathrm{pl}}}{\mathrm{d}\mathbf{C}} + \partial_{\mathbf{C}^{\mathrm{e}}}\mathbf{S} \bullet\circ \frac{\mathrm{d}\mathbf{C}^{\mathrm{e}}}{\mathrm{d}\mathbf{C}}. \tag{4.24}$$

Taking into account the dependence of $\mathbf{F}^{\mathrm{pl}}$ on $\mathbf{N}$ and $\Delta\lambda$, the term $\frac{\mathrm{d}\mathbf{F}^{\mathrm{pl}}}{\mathrm{d}\mathbf{C}}$ in the above equation is further expanded as

$$\frac{\mathrm{d}\mathbf{F}^{\mathrm{pl}}}{\mathrm{d}\mathbf{C}} = \partial_{\mathbf{N}}\mathbf{F}^{\mathrm{pl}} \bullet\circ \frac{\mathrm{d}\mathbf{N}}{\mathrm{d}\mathbf{C}} + \partial_{\Delta\lambda}\mathbf{F}^{\mathrm{pl}}\ \frac{\mathrm{d}\Delta\lambda}{\mathrm{d}\mathbf{C}}. \tag{4.25}$$

Moreover, with $\mathbf{C}^{\mathrm{e}}$ reformulated as $\mathbf{C}^{\mathrm{e}} = \mathbf{F}^{\mathrm{pl}\,-\mathrm{T}} \cdot \mathbf{C} \cdot \mathbf{F}^{\mathrm{pl}\,-1}$, the derivative $\frac{\mathrm{d}\mathbf{C}^{\mathrm{e}}}{\mathrm{d}\mathbf{C}}$ is simplified to

$$\frac{\mathrm{d}\mathbf{C}^{\mathrm{e}}}{\mathrm{d}\mathbf{C}} = \mathbf{F}^{\mathrm{pl}\,-\mathrm{T}} \otimes \mathbf{F}^{\mathrm{pl}\,-1}. \tag{4.26}$$

For the derivation of the remaining components in Eq 4.24 such as $\partial_{\mathbf{C}^{\mathrm{e}}}\mathbf{S}$, $\partial_{\mathbf{F}^{\mathrm{pl}}}\mathbf{C}^{\mathrm{e}}$ and $\partial_{\mathbf{F}^{\mathrm{pl}}}\mathbf{S}$ the interested reader is referred to Appendix B.4. Having the general tangent operator a distinction is made for the fully elastic and the elastoplastic case in what follows.

For fully elastic deformation, the terms related to plastic deformation vanish. Consequently, the tangent operator in the material configuration is simplified to,

$$\begin{aligned} \mathbb{C} \;=\; \lambda \Big[\mathrm{J}^2 \left(\mathbf{C}^{\mathrm{e}\,-1}_{t+\Delta t} \,\oplus\, \mathbf{C}^{\mathrm{e}\,-1}_{t+\Delta t} \right) - \left(\mathrm{J}^2 - 1 \right) \\ \left(\mathbf{C}^{\mathrm{e}\,-1}_{t+\Delta t} \,\otimes\, \mathbf{C}^{\mathrm{e}\,-1}_{t+\Delta t} \right) \Big] + 2\,\mu\, \left(\mathbf{C}^{\mathrm{e}\,-1}_{t+\Delta t} \,\otimes\, \mathbf{C}^{\mathrm{e}\,-1}_{t+\Delta t} \right). \end{aligned} \tag{4.27}$$

By way of contrast, the terms $\frac{\mathrm{d}\mathbf{N}}{\mathrm{d}\mathbf{C}}$ and $\frac{\mathrm{d}\Delta\lambda}{\mathrm{d}\mathbf{C}}$ have to be computed in case of elastoplastic deformation. This is done by linearizing the nonlinear system of equations in Eq 4.17 with respect to $\mathbf{C}$ such that

$$\begin{aligned} \frac{\mathrm{d}\mathbf{R}_1}{\mathrm{d}\mathbf{C}} &= \partial_{\mathbf{N}}\mathbf{R}_1 \bullet\circ \frac{\mathrm{d}\mathbf{N}}{\mathrm{d}\mathbf{C}} + \partial_{\Delta\lambda}\mathbf{R}_1 \ \oplus \ \frac{\mathrm{d}\Delta\lambda}{\mathrm{d}\mathbf{C}} + \partial_{\mathbf{C}}\mathbf{R}_1 \\ \frac{\mathrm{dR}_2}{\mathrm{d}\mathbf{C}} &= \partial_{\mathbf{N}}\mathrm{R}_2 \bullet\circ \frac{\mathrm{d}\mathbf{N}}{\mathrm{d}\mathbf{C}} + \partial_{\Delta\lambda}\mathrm{R}_2 \ \frac{\mathrm{d}\Delta\lambda}{\mathrm{d}\mathbf{C}} + \partial_{\mathbf{C}}\mathrm{R}_2, \end{aligned} \tag{4.28}$$

where the nonstandard dyadic product ($\oplus$) is described in Appendix A. The terms $\partial_{\mathbf{C}}\mathbf{R}_1$ and $\partial_{\mathbf{C}}\mathrm{R}_2$ are defined as

$$\begin{aligned} \partial_{\mathbf{C}}\mathbf{R}_1 &= \partial_{\mathbf{\Sigma}}\mathbf{R}_1 \bullet\circ \partial_{\mathbf{C}}\mathbf{\Sigma} &&= \frac{\partial^2 f}{\partial\mathbf{\Sigma}\partial\mathbf{\Sigma}} \bullet\circ \partial_{\mathbf{C}}\mathbf{\Sigma} \\ \partial_{\mathbf{C}}\mathrm{R}_2 &= \partial_{\mathbf{\Sigma}}\mathrm{R}_2 \bullet\circ \partial_{\mathbf{C}}\mathbf{\Sigma} &&= \frac{\partial f}{\partial\mathbf{\Sigma}} \bullet\circ \partial_{\mathbf{C}}\mathbf{\Sigma}. \end{aligned} \tag{4.29}$$

For further details the interested reader is referred to Appendix B. By setting $\frac{\mathrm{d}\mathbf{R}_1}{\mathrm{d}\mathbf{C}} = 0$ and $\frac{\mathrm{dR}_2}{\mathrm{d}\mathbf{C}} = 0$, which is fulfilled for a converged return-mapping step ($\mathbf{R}_1 = 0$ and $\mathrm{R}_2 = 0$),

$$\begin{aligned} \frac{\mathrm{d}\Delta\lambda}{\mathrm{d}\mathbf{C}} &= -\frac{\left[\partial_{\mathbf{C}}\mathrm{R}_2 - \partial_{\mathbf{N}}\mathrm{R}_2 \bullet\circ \left(\partial_{\mathbf{N}}\mathbf{R}_1\right)^{-1} \bullet\circ \partial_{\mathbf{C}}\mathbf{R}_1\right]}{\partial_{\Delta\lambda}\mathrm{R}_2 - \partial_{\mathbf{N}}\mathrm{R}_2 \bullet\circ \left(\partial_{\mathbf{N}}\mathbf{R}_1\right)^{-1} \bullet\circ \partial_{\Delta\lambda}\mathbf{R}_1} \\ \frac{\mathrm{d}\mathbf{N}}{\mathrm{d}\mathbf{C}} &= -\left(\partial_{\mathbf{N}}\mathbf{R}_1\right)^{-1} \bullet\circ \left(\partial_{\Delta\lambda}\mathbf{R}_1 \ \oplus \ \frac{\mathrm{d}\Delta\lambda}{\mathrm{d}\mathbf{C}} + \partial_{\mathbf{C}}\mathbf{R}_1\right), \end{aligned} \tag{4.30}$$

can be derived. With Eq. 4.30, the tangent moduli as defined by Eq. 4.23 can be computed.

It is worth mentioning that the tangent moduli requested by the ABAQUS® solver has the form

$$\mathbb{C}^{\mathrm{ep}} = 1/\mathrm{J} \ \left[\left(\mathbf{F} \otimes \mathbf{F}^{\mathrm{T}}\right) \bullet\circ \mathbb{C} \bullet\circ \left(\mathbf{F}^{\mathrm{T}} \otimes \mathbf{F}\right)\right]^{\mathrm{R}}, \tag{4.31}$$

where the nonstandard tensor transposition $(()^{\mathrm{R}})$ is described in Appendix A. In other words, the elastoplastic tangent operator $\mathbb{C}^{\mathrm{ep}}$ is described by the push-forward of the material description of the tangent operator $\mathbb{C}$ with respect to $\mathbf{F}$. Eq 4.31 can also be rewritten using the index notation such that

$$\mathbb{C}^{\mathrm{ep}}_{\mathrm{abcd}} = 1/\mathrm{J} \ \mathrm{F}_{\mathrm{aA}}\mathrm{F}_{\mathrm{bB}}\mathrm{F}_{\mathrm{cC}}\mathrm{F}_{\mathrm{dD}}\mathbb{C}^{\mathrm{R}}{}_{\mathrm{ABCD}}. \tag{4.32}$$

4.2.4 Consideration for plane stress condition

Up to this point, the numerical implementation of the constitutive model is developed in a general three-dimensional framework. In this section, the projection of this implementation to a plane stress condition (for instance, in the case of shell element formulation) is realized by ensuring a zero stress response in the out of plane direction, i.e.,

$$\mathrm{P}_{3i} = \mathrm{P}_{i3} = 0. \tag{4.33}$$

This is done within the general framework avoiding separate implementations of the three-dimensional and the plane stress model, see also Borst (1991).

For enforcing plane stress conditions the three-dimensional unconstrained deformation gradient has to be modified. For that purpose, the linearization of the stress with respect to the deformation gradient,

$$\mathrm{d}\mathbf{P} = \frac{\mathrm{d}\mathbf{P}}{\mathrm{d}\mathbf{F}} \bullet\circ \mathrm{d}\mathbf{F}, \tag{4.34}$$

is considered. For instance, taking into account only the normal out of plane stress P_{33}, the corresponding modified deformation gradient $\mathrm{F}_{33\mathrm{t}+\Delta\mathrm{t}}$ can be expressed as

$$\mathrm{F}_{33}{}^{j+1}_{\mathrm{t}+\Delta\mathrm{t}} = \mathrm{F}_{33}{}^{j}_{\mathrm{t}+\Delta\mathrm{t}} - \mathrm{P}_{33}{}^{j}_{\mathrm{t}+\Delta\mathrm{t}} \Big/ \left(\frac{\mathrm{d}\mathbf{P}}{\mathrm{d}\mathbf{F}}\right)_{3333\mathrm{t}+\Delta\mathrm{t}}, \tag{4.35}$$

where j is the iteration count. The adjusted deformation gradient is then incorporated into the subsequent return-mapping algorithm to recompute the stress responses. Furthermore, for a global quadratic convergence, the consistent tangent operator is recomputed based on the aforementioned modification. This is performed iteratively until the plane stress conditions are achieved.

4.3 Verification of the numerical implementation

For verifying the correctness of the proposed implementations, all models are compared to each other. An implementation included in the finite element program ABAQUS® is also considered. As a prototype model, associative von Mises plasticity theory with isotropic hardening is considered. Concerning loading, uniaxial tension is applied. Fig. 4.1 shows the stress-strain responses obtained from the simulations. According to this figure, the responses for all implementations are equivalent confirming the correctness of the proposed implementations.

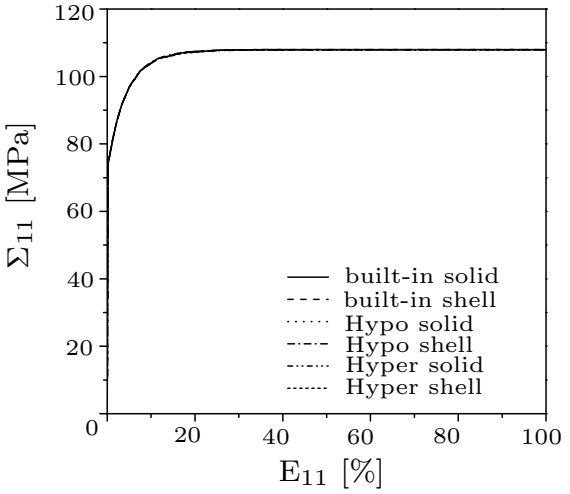

Figure 4.1: Comparison between the stress-strain responses obtained from the proposed hyperelastic and hypoelastic based models as well as from the implementation included in ABAQUS® (isotropic von Mises-type model).

5 Localization criterion

The current chapter presents a localization criterion and its numerical implementation incorporated within the constitutive model developed in the previous chapters. This criterion is employed for the determination of limiting conditions during the production of parts by sheet forming process. There are several theoretical approaches proposed for such application. One possible classification of these methods is based on the order of analysis employed to determine localization. The first category constitutes linear methods, which evaluate the initiation of a localized strain band based on the plastic instability in a homogeneous sheet, cf. (Swift, 1952; Hill, 1952). Another category corresponds to nonlinear methods. These methods establish localization from a plastic instability of a heterogeneous sheet, with the assumption of a preexisting inhomogeneity in the sheet, cf. (Marciniak, 1965; Marciniak & Kuczynski, 1967; Marciniak et al., 1973; Hutchinson & Neale, 1978a,b,c). The inhomogeneity from defects on the sheet develops into necking upon application of deformation. Additionally, there are also semiemperical models, such as the method proposed by (Keeler & Brazier, 1977). Although not always consistent with experimental observations, these methods require computationally little effort. For a comprehensive presentation of the linear and semiemperical methods the reader is referred to (Butuc, 2004; Banabic et al., 2000; Kuroda & Tvergaard, 2000). In what follows, the nonlinear approach, specifically the work of Marciniak and Kuczynski will be detailed.

5.1 Marciniak and Kuczynski localization criterion

For predicting limit strains of sheet forming processes, Marciniak and Kuczynski introduced one of the most frequently applied localization criteria, the so-called MK-criterion, cf. Marciniak & Kuczynski (1967). This method assumes the existence of an infinite length band of inhomogeneity in an otherwise homogeneous work-piece. In the original work, the inhomogeneity band is oriented in the minor principal deformation direction of the work-piece. Localization is assumed to occur once the ratio of the strain in the inhomogeneous to that in the homogeneous region is below a prescribed critical value. The resulting limit strains are presented in the so-called Forming Limit Diagram (FLD), cf. Keeler

& Backofen (1963). The original MK approach span only the positive domain of the FLD, that is, only positive minor principal strains are considered. This model was later improved by assuming an arbitrary orientation of the inhomogeneity, see (Hutchinson & Neale, 1978a,b,c). Such improvement enabled the prediction of the limit strains for both the negative and the positive domain of the FLD. In this work, this improved version of the MK model is employed.

Like the original MK approach, the inhomogeneity band is introduced in terms of a reduced thickness of the work-piece. However, the orientation of the band is represented by an arbitrary rotation angle θ. This angle is measured from the frame of reference defined for the homogeneous region as shown in Fig. 5.1. For the sake of simplicity, quantities characterizing the band of inhomogeneity are represented by the superscript $()^b$, while those characterizing the homogeneous region are represented by the superscript $()^a$. Mathematically, the inhomogeneity is expressed by the ratio of thicknesses of the two regions such that

$$\gamma_o = \frac{\mathrm{t}_o^b}{\mathrm{t}_o^a}, \qquad \gamma = \exp(\mathrm{E}_{zz}^b - \mathrm{E}_{zz}^a)\,\gamma_o, \tag{5.1}$$

where γ_o and γ are the initial and current inhomogeneity of the work-piece, respectively. t_o^b and t_o^a are the initial thicknesses while E_{zz}^b and E_{zz}^a are out-of-plane strains of the respective regions. Additionally, the orientation of the inhomogeneity band evolves with the deformation following the relation

$$\tan(\theta) = \exp(\mathrm{E}_{xx}^a - \mathrm{E}_{yy}^a)\tan(\theta_o), \tag{5.2}$$

with θ_o being the initial orientation of the band provided at the undeformed state.

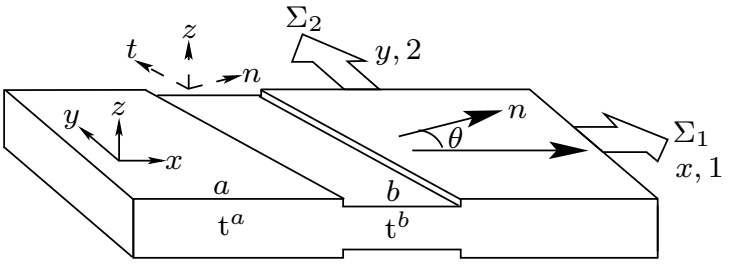

Figure 5.1: Schematic representation of MK model, cf. (Marciniak & Kuczynski, 1967; Hutchinson & Neale, 1978b,c).

The relation between the homogeneous and inhomogeneous regions are established through the conditions of geometrical compatibility and equilibrium. For that purpose, the deformation and stress fields of the two regions are evaluated in the rotated coordinate system, which is consistent with that of

the inhomogeneous region and denoted as ntz, see Fig. 5.1. For transforming these quantities from the reference frame xyz to the rotated coordinate system a second-order rotation tensor $\mathbf{Q}$,

$$\mathbf{Q} = \begin{bmatrix} \cos\theta & \sin\theta & 0 \\ -\sin\theta & \cos\theta & 0 \\ 0 & 0 & 1 \end{bmatrix} \quad , \tag{5.3}$$

is introduced. Subsequently, the transformed deformation in terms of $\boldsymbol{d}^*$ and the stress $\boldsymbol{\Sigma}^*$ quantities take the forms

$$\begin{aligned} \boldsymbol{d}^* &= \mathbf{Q} \cdot \boldsymbol{d} \cdot \mathbf{Q}^{\mathrm{T}} \\ \boldsymbol{\Sigma}^* &= \mathbf{Q} \cdot \boldsymbol{\Sigma} \cdot \mathbf{Q}^{\mathrm{T}}. \end{aligned} \tag{5.4}$$

The geometrical compatibility condition at the boundary between the two regions relates the incremental strains in the rotated coordinate system such that

$$\begin{aligned} d^{*a}_{\ tt} &= d^{*b}_{\ tt} \\ d^{*a}_{\ nt} &= d^{*b}_{\ nt}, \end{aligned} \tag{5.5}$$

where, $d^{*a}_{\ tt}$ and $d^{*b}_{\ tt}$ refer to the deformation velocity gradient components parallel to the band while $d^{*a}_{\ nt}$ and $d^{*b}_{\ nt}$ refer to the shear components. Furthermore, the equilibrium conditions are established by relating the stresses and the inhomogeneity, i.e.,

$$\begin{aligned} \Sigma^{*a}_{\ nn} &= \gamma\, \Sigma^{*b}_{\ nn} \\ \Sigma^{*a}_{\ tn} &= \gamma\, \Sigma^{*b}_{\ tn}. \end{aligned} \tag{5.6}$$

The stress components used in the above equilibrium relation are those normal $\Sigma^{*a}_{\ nn}$ and $\Sigma^{*b}_{\ nn}$ as well as the shear components $\Sigma^{*a}_{\ tn}$ and $\Sigma^{*b}_{\ tn}$ parallel to the inhomogeneity band.

After enforcing the preceding conditions, the ratio of the out-of-plane strain increments in the inhomogeneous to that in the homogeneous region is computed. As mentioned before, localization is considered to occur when this ratio exceeds a prescribed critical value Υ, i.e.,

$$\frac{\mathrm{E}^{\mathrm{b}}_{\mathrm{zz}}}{\mathrm{E}^{\mathrm{a}}_{\mathrm{zz}}} > \Upsilon \quad . \tag{5.7}$$

Here, the recommended value for Υ is 10, cf. Banabic et al. (2000). The choice of this value is rather arbitrary since $\mathrm{E}^{\mathrm{b}}_{\mathrm{zz}}$ changes almost discontinuously (high gradient), cf. (Hutchinson & Neale, 1978b; Kuroda & Tvergaard, 2000). The limit strains are then taken to be the computed principal strains in the homogeneous region.

5.2 Numerical implementation

This section describes the numerical implementation of the MK localization criterion. Initially, the stress and strain responses of the homogeneous region are computed and transformed to the rotated configuration of the inhomogeneous region according to Eq. 5.4. For the computation of the corresponding stress and strain states in the inhomogeneous region, the geometrical compatibility condition in Eq 5.5 and the equilibrium condition in Eq 5.6 along with the yield criterion are exploited. Making use of the constraining conditions, all state variables are described by three basic variables. These are the plastic multiplier $\Delta\lambda^b$ and the components of the normal tensor to the yield surface, namely those parallel to the inhomogeneous band ${\mathrm{N}^*}^b_{nn}$ and the shear term ${\mathrm{N}^*}^b_{tn}$. The nonlinear equations used to solve the basic variables are formulated from the residuals of the equilibrium condition and the yield criterion, which read

$$\begin{aligned} \mathrm{R}_1 : &= {\Sigma^*}^a_{nn} - \gamma\, {\Sigma^*}^b_{nn} \\ \mathrm{R}_2 : &= {\Sigma^*}^a_{tn} - \gamma\, {\Sigma^*}^b_{tn} \\ \mathrm{R}_3 : &= f({\mathrm{N}^*}^b_{nn}, {\mathrm{N}^*}^b_{tn}, \Delta\lambda^b). \end{aligned} \tag{5.8}$$

The solution is then obtained by iteratively solving Eq 5.8. The required linearization is derived with respect to ${\mathrm{N}^*}^b_{nn}$, ${\mathrm{N}^*}^b_{tn}$ and $\Delta\lambda^b$, which reads

$$\begin{aligned} \partial_{{\mathrm{N}^*}^b_{nn}} \mathrm{R}_1\, \mathrm{d}{\mathrm{N}^*}^b_{nn} + \partial_{{\mathrm{N}^*}^b_{tn}} \mathrm{R}_1\, \mathrm{d}{\mathrm{N}^*}^b_{tn} + \partial_{\Delta\lambda^b} \mathrm{R}_1\, \mathrm{d}\Delta\lambda^b &= -\mathrm{R}_1 \\ \partial_{{\mathrm{N}^*}^b_{nn}} \mathrm{R}_2\, \mathrm{d}{\mathrm{N}^*}^b_{nn} + \partial_{{\mathrm{N}^*}^b_{tn}} \mathrm{R}_2\, \mathrm{d}{\mathrm{N}^*}^b_{tn} + \partial_{\Delta\lambda^b} \mathrm{R}_2\, \mathrm{d}\Delta\lambda^b &= -\mathrm{R}_2 \\ \partial_{{\mathrm{N}^*}^b_{nn}} \mathrm{R}_3\, \mathrm{d}{\mathrm{N}^*}^b_{nn} + \partial_{{\mathrm{N}^*}^b_{tn}} \mathrm{R}_3\, \mathrm{d}{\mathrm{N}^*}^b_{tn} + \partial_{\Delta\lambda^b} \mathrm{R}_3\, \mathrm{d}\Delta\lambda^b &= -\mathrm{R}_3, \end{aligned} \tag{5.9}$$

where the components of the linearized terms are described in Appendix B. Following the solution of the linearized equations, the updates are obtained from the relation

$$\begin{aligned} {\mathrm{N}^*}^{b\ j+1}_{nn} &= {\mathrm{N}^*}^{b\ j}_{nn} + \mathrm{d}{\mathrm{N}^*}^b_{nn} \\ {\mathrm{N}^*}^{b\ j+1}_{tn} &= {\mathrm{N}^*}^{b\ j}_{tn} + \mathrm{d}{\mathrm{N}^*}^b_{tn} \\ {\Delta\lambda^b}^{j+1} &= {\Delta\lambda^b}^{j} + \mathrm{d}\Delta\lambda^b, \end{aligned} \tag{5.10}$$

with j representing the iteration count. Solving the linear system of equations and updating continues until convergence. Subsequently, the limit strains are taken to be the principal strains computed in the homogeneous region upon localization.

Remark 5 *The orientation of the inhomogeneous band corresponding to the critical limiting condition is identified by incrementing θ with a value of 1^o*

starting from a zero angle. Within each increment, however, the orientation evolves according to Eq. 5.2.

Remark 6 *In principle, the MK criterion is a post processing technique. Thus, it does not affect the mechanical responses of a given process. This fact, supported by its good predictive capability, makes the criterion very efficient.*

Remark 7 *Plasticity is a path-dependent process. Consequently, the strain response within the band depends on the previous plastic deformation. However, numerical experiments have shown that using the previous plastic strains computed in the homogeneous domain also within the band does not lead to large differences. The reason for this is the thickness of the band, which changes almost discontinuously (high gradient). Therefore and for avoiding unnecessary memory storage, this assumption has also been used in the final implementation.*

6 Mechanical characterization

The calibration of the phenomenological constitutive model described in Chapter 3 strongly depends on the mechanical properties of a given material. In this chapter, the mechanical characterization carried out on magnesium alloys using standardized uniaxial tensile tests is presented. These tests are intended to characterize the materials with respect to test temperature, specimen orientation and strain rates.

6.1 Materials under investigation

The mechanical characterization was performed for two different magnesium alloys. These were the benchmark alloy AZ31 in a heat treated condition (AZ31 O-temper) and a new alloy, ZE10, both having a thickness of 1.3mm. Following the inclusion of rare-earth elements and compared to AZ31, ZE10 shows improved mechanical properties at room temperature, cf. (Bohlen et al., 2007; Stutz et al., 2009; Yi et al., 2010). According to the aforementioned studies, this improvement in the mechanical properties is attributed to the change in the underlying microstructures of the alloy. This is shown in the 0002 pole figures in Fig. 6.1, which demonstrate the distinct textures of the two alloys. In the figures, it is shown that AZ31 has a strong basal texture with preferred orientation towards rolling direction. This translates to a lower formability and an observable level of material anisotropy. On the other hand, ZE10 exhibits a relatively weaker basal texture, thus, implying better formability. The preferred orientation towards transverse direction, however, indicates an even pronounced material anisotropy. For a comprehensive description of textures in relation to the mechanical properties of materials, the reader is referred to Kocks et al. (1998).

6.2 Experimental setup

The experiments were conducted using flat specimens prepared according to the DIN 50125-H standard. As such, each specimen has a gage length of 60mm and a width of 12.5mm. For checking the reproducibility of the experimen-

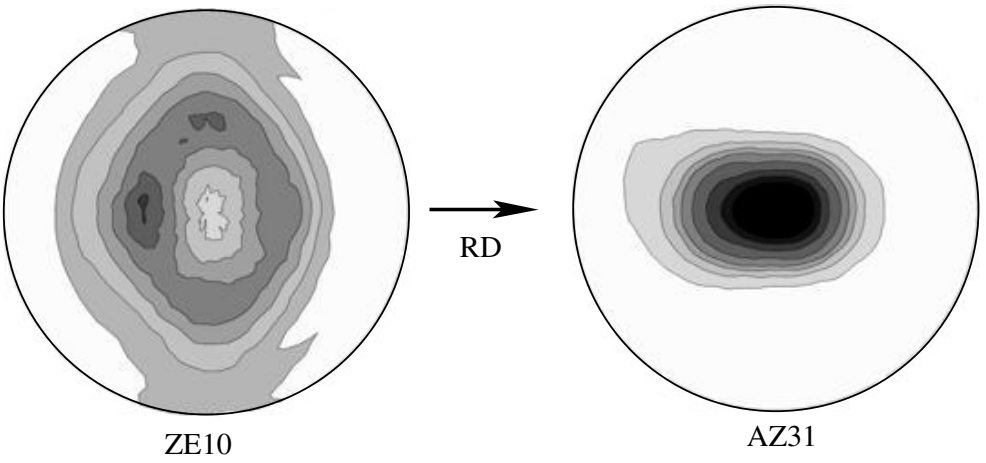

Figure 6.1: 0002 pole figures of ZE10 and AZ31; AZ31 shows strong basal texture, while a relatively weaker basal texture is observed in ZE10

tal results, at least two specimens per orientation were tested. Additionally, the specimens are oriented in rolling direction (RD), 45^o and 90^o (TD) from RD, see Fig. 6.2(a). The tests reported in this work were carried out at room

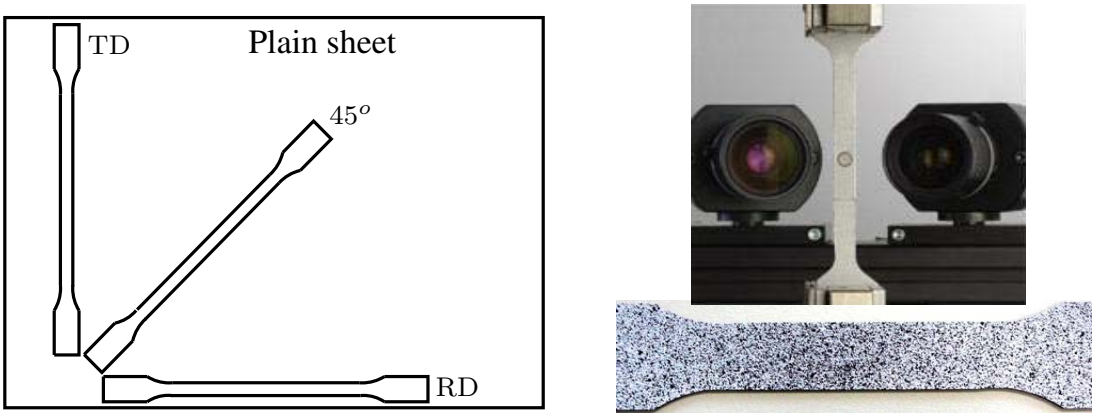

(a) Tensile test specimen geometry

(b) ARAMIS® setup and surface treatment

Figure 6.2: Tensile test specimen geometry, experimental setup and surface treatment for ARAMIS® measurement.

temperature and at an elevated temperature of 200^oC. The choice of the test temperature 200^oC follows from the studies in (Dröder, 1999; Doege & Dröder, 2001). These studies indicate that for commercial magnesium alloys such as AZ31, the forming temperature range that yields sufficient formability lies between 150^oC and 250^oC. The tests at room temperature are considered to be references based on which the tests at 200^oC are evaluated and described. For

quantifying the strain rate effects, additional tests were performed at the three strain rates 0.001/s, 0.02/s and 0.1/s. The tests were conducted by a ZWICK® universal testing machine. For deformation measurement, mechanical extensometer and an optical field deformation measuring system (ARAMIS® system) were used. The use of an ARAMIS® system requires special surface treatment of the test specimens. This is necessary for establishing a stochastic pattern that can be analyzed with image processing tools. This was achieved by applying a white developer spray on the background followed by a graphite spray to create a stochastic pattern with a good contrast, see Fig. 6.2(b). For detailed information on the use of the ARAMIS® system the interested reader is referred to the ARAMIS® manual.

6.3 Mechanical responses

The mechanical responses obtained from the tensile tests are presented in terms of direction-dependent flow curves and r-values. The flow curves relate the true stresses with the logarithmic plastic strains. The true stress is computed from the force-displacement signal assuming material incompressibility during plastic deformation.

The anisotropy of sheets can be conveniently characterized by the r-value. This value is defined as

$$r = \frac{\varepsilon_w^{\mathrm{pl}}}{\varepsilon_t^{\mathrm{pl}}}, \tag{6.1}$$

where $\varepsilon_w^{\mathrm{pl}}$ and $\varepsilon_t^{\mathrm{pl}}$ are the logarithmic plastic strains in the width and thickness direction, respectively. By assuming material incompressibility the strain $\varepsilon_t^{\mathrm{pl}}$ is calculated from the longitudinal and transverse plastic strains, i.e.,

$$\varepsilon_t^{\mathrm{pl}} = -(\varepsilon_l^{\mathrm{pl}} + \varepsilon_w^{\mathrm{pl}}) \qquad \Rightarrow \qquad r = -\frac{\varepsilon_w^{\mathrm{pl}}}{\varepsilon_l^{\mathrm{pl}} + \varepsilon_w^{\mathrm{pl}}}, \tag{6.2}$$

where $\varepsilon_l^{\mathrm{pl}}$ is plastic strain in the longitudinal direction.

Remark 8 *Strictly speaking, Eq. 6.2 is only valid for small plastic deformation or for deformation paths with a constant strain direction. While for RD and TD the latter condition is exactly fulfilled, it is only reasonably approximated in case of specimens with an orientation of 45°. However, it bears emphasis that Eq. 6.2 can also be considered as a definition of the variable $\varepsilon_t^{\mathrm{pl}}$. In this case, the definition Eq. 6.1 does not rely on the aforementioned assumptions.*

Remark 9 *The r-values are computed at all levels of the deformation taking advantage of the continuous measurements of the ARAMIS® system.*

Remark 10 *Out of the multiple tests conducted for checking reproducibility, the results presented here correspond to those tests with responses close to the mean values. The experimental scatter in terms of the stress responses was recorded to be maximum of 5MPa.*

6.3.1 Mechanical responses at room temperature

Following the tests at room temperature, the flow curves obtained for the alloy ZE10 show higher yield stresses in RD than in TD and 45^o, see Fig. 6.3(a). This manifests the anisotropic behavior of the material. The yield stress difference is less pronounced between TD and 45^o. Represented by the hashed region, Fig. 6.3(a) also reveals an observable amount of localized deformation. Here, the localized deformation is defined as that beyond the point of the recorded maximum engineering stress. Similar tests on AZ31 reveal higher yield stresses in TD than in 45^o, which in turn is greater than the response in RD, see Fig. 6.3(b). These differences in the yield stresses confirm the yield anisotropy of the material. Between the two alloys, AZ31 shows a higher stress level, see Table 6.1. On the other hand, although ZE10 undergoes larger localized deformation, the level of ductility for both alloys is similar.

Mat.	Ori.	YS (MPa)	UTS (MPa)	Us (%)	Ms (%)
ZE10	RD	144	229	11.3	16.3
	45^o	121	221	15.2	22.6
	TD	111	220	15.7	18.9
AZ31	RD	163	266	18.3	21.5
	45^o	175	269	16.7	20.3
	TD	187	275	16.0	17.4

Table 6.1: Yield (YS) and ultimate (UTS) tensile stresses together with uniform (Us) and maximum (Ms) strains measured for ZE10 and AZ31 at RT.

A comparison of the r-values is also carried out for the two alloys. These r-values are evaluated based on the strain measurements obtained from the ARAMIS® system. In Fig. 6.4(a), it is shown that the r-values for ZE10 at RT are found to be below or around one. The different orientations indicate only a slight difference in r-values. This reveals the existence of a small planar anisotropy. Moreover, the curves describing the r-values as a function of the strain reveal a slight strain-dependency. This strain-dependency further decreases with increasing strain. The r-values for AZ31 are plotted in

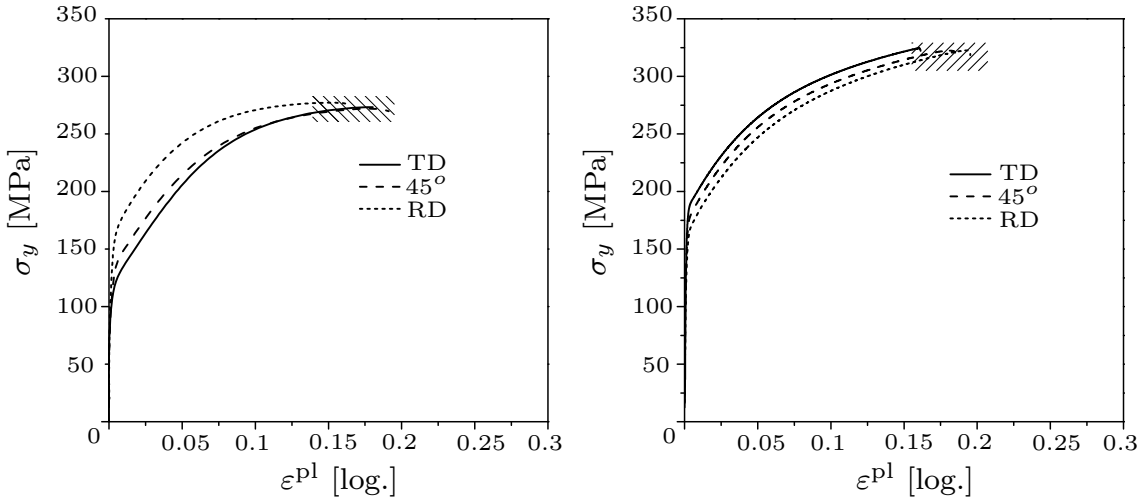

(a) Flow curve of ZE10

(b) Flow curve of AZ31

Figure 6.3: Flow curves measured for ZE10 and AZ31 at room temperature; the hashed section corresponds to localized deformation.

Fig. 6.4(b). From the figure, it can be seen that the different r-values for the different orientations confirm the existence of a stronger planar anisotropy of the material. In a strain range between 5 and 12 percent, the r-values are found to be slightly strain-dependent. Such behavior is not in line with the conventional approach of adopting a constant r-value, often taken within a strain range of 5 to 20 percent, cf. (Banabic et al., 2000; Hosford & Caddell, 2007). Overall, it is observed that the r-values of AZ31 are much higher than those of ZE10. Thus, AZ31 reveals a stronger planar anisotropy in terms of r-values than ZE10. This, however, does not hold for the stresses.

6.3.2 Mechanical responses at 200^oC

The effect of temperature on the mechanical response is quantified based on uniaxial tensile tests conducted at 200^oC and a strain rate of 0.02/s. In the following, this effect is discussed for both materials, ZE10 and AZ31, in comparison to the measurements at room temperature. Concerning ZE10, the first observation is a significant increase in the maximum strain attained in testing, which implies an increase in ductility, see Table 6.2. However, as indicated by the hashed region in Fig. 6.5(a), a significant increase in localized deformation is also recorded. Another observation is a significant drop in the yield stress. It can also be seen that the yield anisotropy is lower. Similar observations regarding the stress-strain responses for AZ31 have also been made. A large increase in the maximum strain attained in testing indicates an improved ductility, see Table 6.2. However, the uniform deformation range decreases along

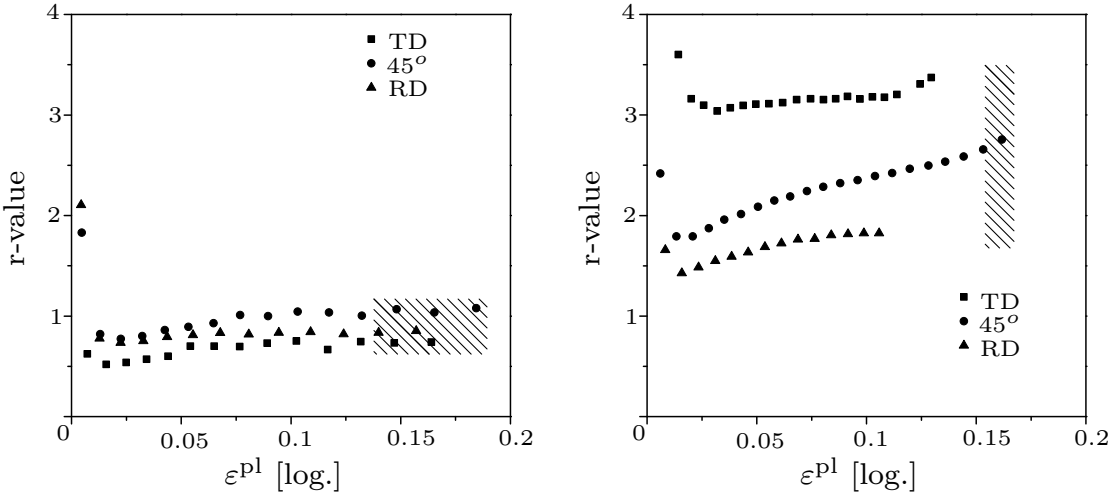

(a) r-value ZE10 (b) r-value of AZ31

Figure 6.4: r-values measured for ZE10 and AZ31 at room temperature; the hashed section corresponds to localized deformation.

with the yield stress, which diminishes by more than 50 percent of the stress at RT. Fig. 6.5(b) also shows a less pronounced yield anisotropy.

Mat.	Ori.	YS (MPa)	UTS (MPa)	Us (%)	Ms (%)
ZE10	RD	86	112	17.1	50.7
	45^o	78	104	19.5	73.7
	TD	80	105	19.3	64.4
AZ31	RD	80	119	12.1	53.8
	45^o	81	118	10.9	53.7
	TD	86	122	10.3	52.5

Table 6.2: Yield (YS) and ultimate (UTS) tensile stresses together with uniform (Us) and maximum (Ms) strains measured for ZE10 and AZ31 at 200^oC.

Following the strain measurements of the ARAMIS® system at 200^oC, the r-values have been computed for both ZE10 and AZ31. In Fig. 6.6, it is shown that the r-values of the two alloys are influenced differently by the test temperature. The r-values for ZE10 show a slight increase compared to those measured at RT. Similar measurements for AZ31, however, show a decrease in r-values within the same strain range, see Fig. 6.6(b). These values show no saturation within the uniform deformation range. This suggests that the r-values have a stronger dependence on strain at 200^oC than at RT.

For demonstrating the strain rate effect of the analyzed alloys additional uniaxial tensile tests at strain rates of 0.001/s and 0.1/s were conducted. The

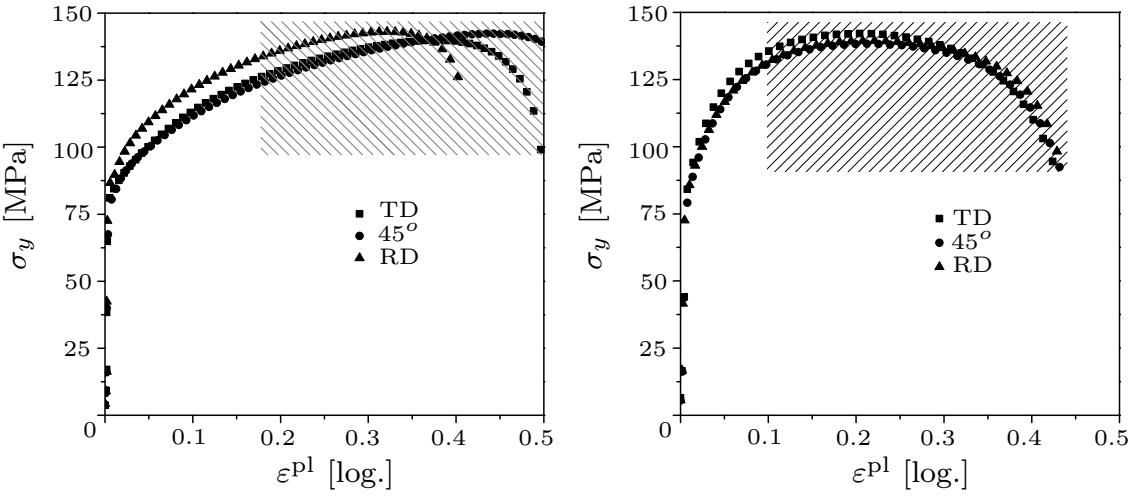

(a) Flow curve of ZE10 (b) Flow curve of AZ31

Figure 6.5: Flow curves measured for ZE10 and AZ31 at 200^oC and strain rate of 0.02/s; the hashed section corresponds to localized deformation.

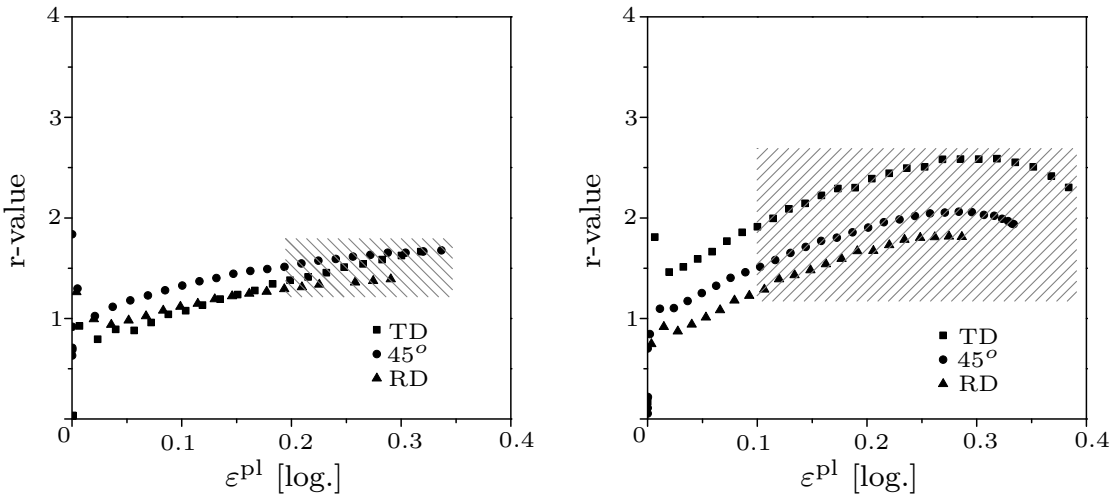

(a) r-value ZE10 (b) r-value of AZ31

Figure 6.6: r-values measured for ZE10 and AZ31 at 200^oC and strain rate of 0.02/s; the hashed section corresponds to localized deformation.

resulting effects are shown for all three orientations, but will be discussed mainly in terms of the stress response for a specimen orientation of 45^o, see Fig. 6.5. The figures indicate the standard effect that increasing the strain rate increases the stress response. The logarithmically scaled quantities of the yield and ultimate stresses and the strain rates is depicted in Fig. 6.7. The linear relation between the logarithmically scaled quantities in Fig. 6.7 implies a power law relation between the unscaled quantities. The effect of strain rate

on ductility is shown in Table 6.3. Accordingly, in case of AZ31 this effect is small. Fig. 6.9(a) for ZE10 and Fig. 6.9(b) for AZ31 demonstrate the effect

Mat.	Rate	YS (MPa)	UTS (MPa)	Us (%)	Ms (%)
ZE10	0.001/s	73	91	19.4	87.6
	0.02/s	78	104	19.5	73.7
	0.1/s	81	109	18.6	61.8
AZ31	0.001/s	72	94	10.0	59.7
	0.02/s	81	118	10.9	53.7
	0.1/s	84	136	12.3	60.6

Table 6.3: Strain rate effect on yield stress, ultimate stress, uniform strain and the maximum strain measured for ZE10 and AZ31 at 200^oC; orientation 45^o.

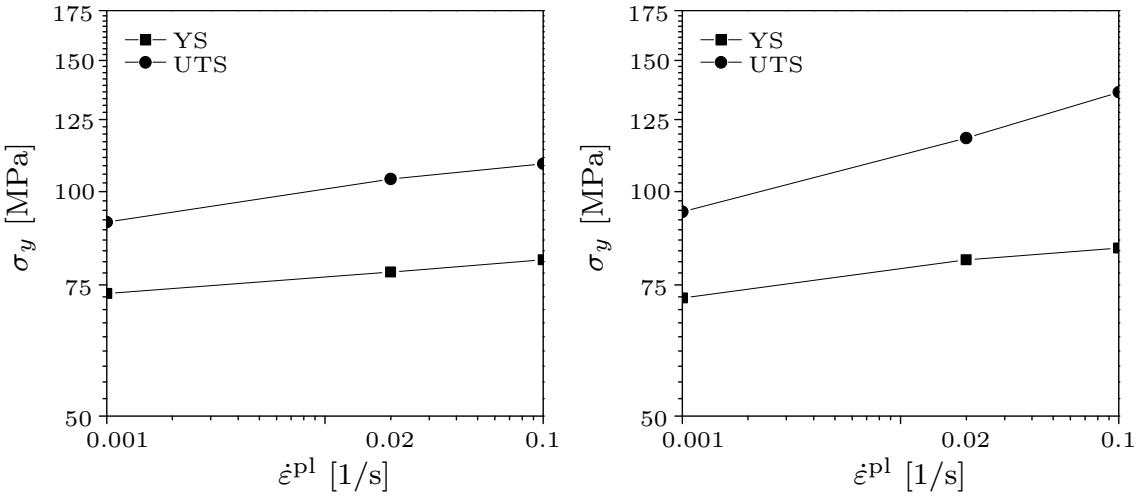

(a) Rate effect ZE10

(b) Rate effect AZ31

Figure 6.7: Effect of strain rate on the yield and ultimate stresses at 200^oC; orientation 45^o.

of strain rates on the r-values. It is observed that in case of AZ31 and similar to the observation made for the stress response, the increase in strain rate increases the r-values. This also implies a considerable effect on the material anisotropy in terms of the strain ratio. In contrast, for ZE10 the increase in strain rate reduces the r-values. For evaluating the effect of strain rate on the yield anisotropy the engineering stress responses from specimens oriented in RD and 45^o for ZE10 and TD and 45^o for AZ31 are plotted in Fig. 6.10. These responses reveal that the strain rate has a relatively small effect on the material anisotropy in terms of the stress response. Thus, the rate effect on the material anisotropy can be neglected.

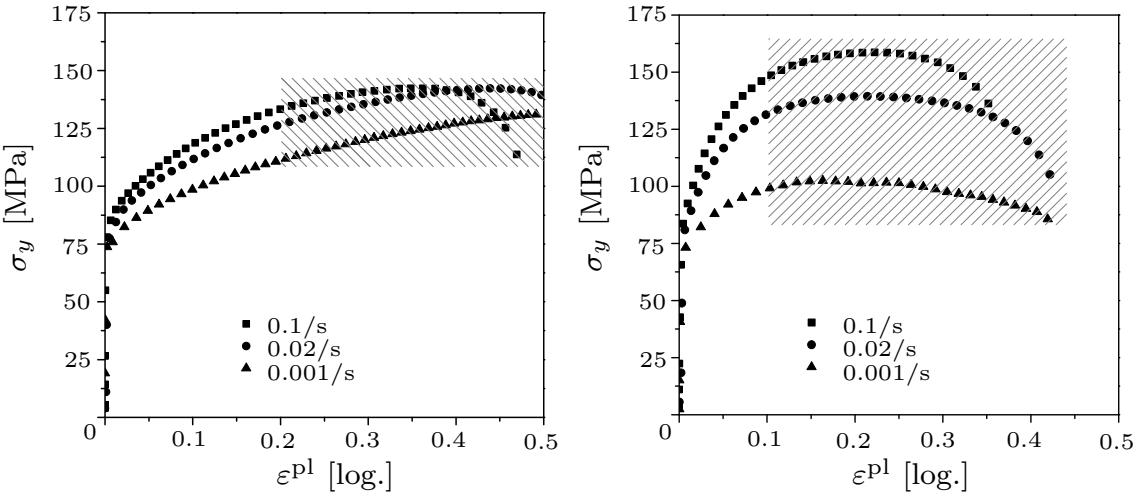

(a) Rate effect ZE10 (b) Rate effect AZ31

Figure 6.8: Effect of strain rate on the flow curves for ZE10 and AZ31 for strain rates of 0.1/s, 0.02/s and 0.001/s at 200^oC; the hashed section corresponds to localized deformation; orientation 45^o.

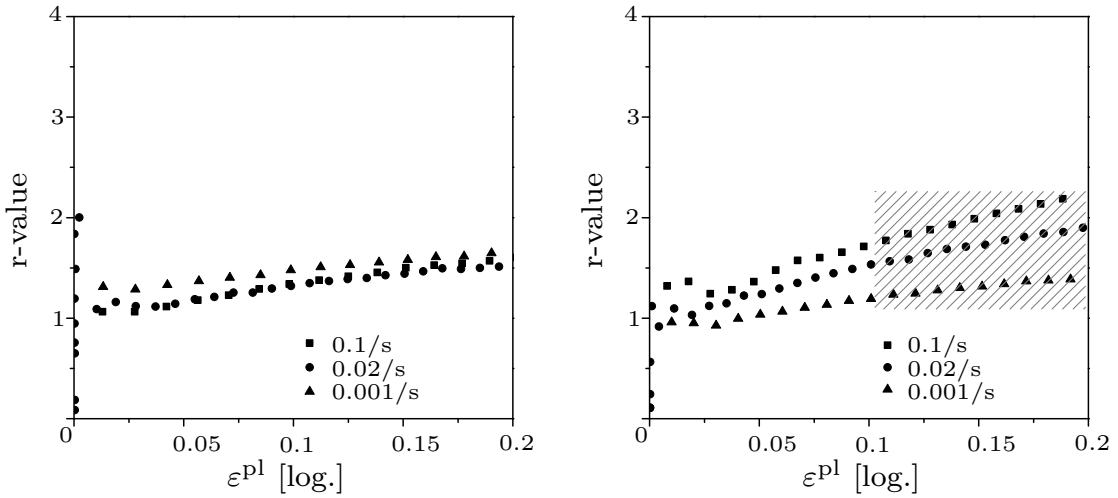

(a) Rate effect ZE10 (b) Rate effect AZ31

Figure 6.9: Effect of strain rate on r-values for ZE10 and AZ31 for strain rates of 0.1/s, 0.02/s and 0.001/s at 200^oC; the hashed section corresponds to localized deformation; orientation 45^o.

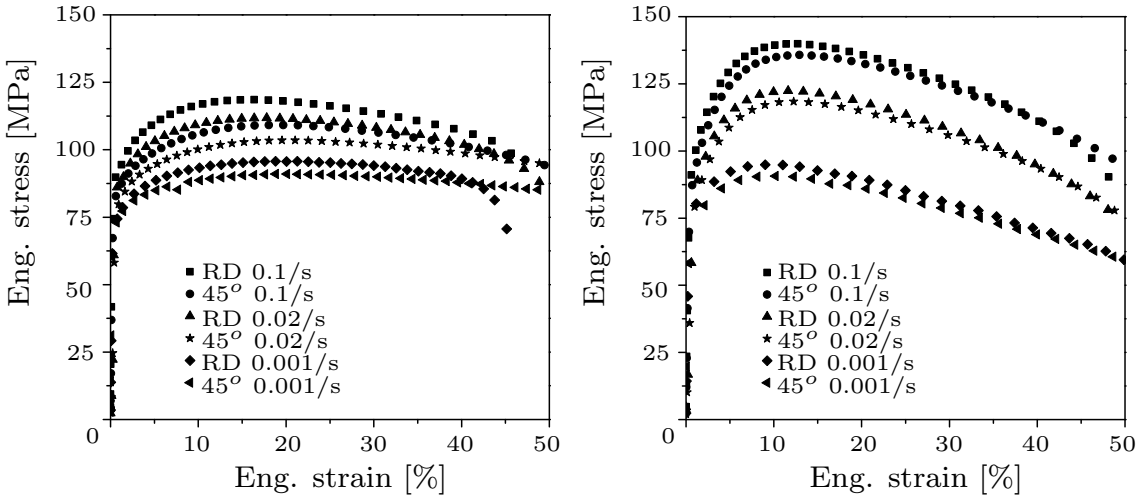

(a) Rate effect ZE10

(b) Rate effect AZ31

Figure 6.10: Effect of strain rate on yield anisotropy for ZE10 and AZ31 for strain rates of 0.1/s, 0.02/s and 0.001/s at 200^oC.

7 Forming limit test

In this chapter, the experimental setup and the resulting responses of sheet forming limit tests for magnesium alloys are presented. There is a large number of experimental methods proposed for such applications. A comprehensive description of these methods can be found in Banabic et al. (2000). The history of the experimental determination of formability dates back to Erichsen (1914). In the method proposed by Erichsen, a hemispherical punch is applied on a work-piece until fracture is observed. During this process, the work-piece is clamped in place by dies. Thus, the formability is judged based on the size of the punch indentation on the work-piece. Mainly attributed to the small tool sizes employed in the method, the accuracy of the resulting formability measures was reported to be limited, see Kokkonen & Hygren (1959). In response to this limitation, several other methods have been proposed. Such details can be found in Banabic et al. (2000). Among these methods, the Nakazima-type forming test is adopted in the current work, cf. (Nakazima et al., 1971; Banabic et al., 2000). To avoid wrinkling, caused by the rectangular work-piece geometry employed in the Nakazima setup, Hasek proposed a set of circular work-pieces having different sizes of recesses, cf. (Hasek, 1973). In this work, the combination of the Nakazima tools and the Hasek work-pieces, which from here onwards referred to as Nakazima-type setup is employed. The results of such formability tests are commonly represented by the forming limit diagram (FLD), as proposed by Keeler & Backofen (1963). This diagram constitutes plots of the maximum and minimum principal in-plane strains, also known as limit strains, obtained at the onset of localization. In addition to the FLD, the results of the forming limit tests are presented in terms of force-displacement plots and strain paths in what follows.

7.1 Experimental setup

The Nakazima-type forming limit tests were conducted based on the ISO 12004 standard. The tests constitute seven circular work-pieces having an initial diameter of 200mm and recesses of different radii ranging from 0 to 80mm as proposed by Hasek (1973), see Fig. 7.1. It is worth to mention that, in this work, the recesses on the work-pieces are all made perpendicular to the rolling

direction. As pointed out in Banabic et al. (2000), the desired ratios of maxi-

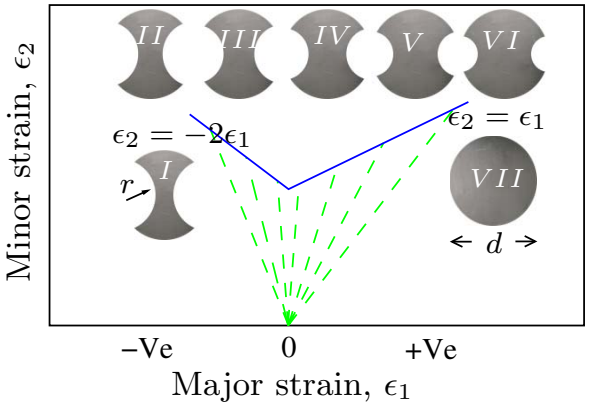

Geo.	$r(mm)$
I	80
II	72.5
III	65
IV	57.5
V	50
VI	40
VII	0

Figure 7.1: Typical FLD plot together with the work-piece geometries having an initial diameter d of 200mm and different recess radii r as proposed by Hasek (1973).

mum (major) and minimum (minor) principal in-plane strains obtained from the tests of the different geometries should range between -2 to 1. Evidently, such bounds are only fulfilled for certain material symmetries. The tests cover the negative as well as positive domain of the FLD, see Fig. 7.1. Additionally, the strain responses obtained from the different geometries during the forming tests should follow linear paths in the FLD, cf. Banabic et al. (2000). Similar to the uniaxial tensile tests described in Chapter 6, the forming limit tests were conducted for the two magnesium alloys, namely ZE10 and AZ31. The test temperature was maintained at 200^oC. This was established by heating up the tools, which constitute the die, holder and punch, along with the work-piece in a separate furnace prior to forming. As recommended by the ISO standard, the punch speed was set to 1mm/s. The clamping force applied to hold the work-piece in place without causing edge fracture was identified to be around 300kN. The lubrication between the punch and the work-piece was established by the use of Teflon placed between two layers of lubrication oil. This follows from the recommendation of the ISO standard to establish a polar localization. For checking the reproducibility of the test results, at least two work-pieces per geometry were tested. In addition to the force response and punch displacement, the history of the deformation field was recorded by the ARAMIS® system. The tests were performed using a universal sheet metal testing machine (ERICHSEN® 145).

7.2 Methods for establishing the forming limits

In this section, two methods for establishing forming limits are detailed. The first of these follows the ISO 12004 standard. According to the ISO standard, the forming limit curve (FLC) is established based on the major and minor in-plane principal strain profiles along sections drawn perpendicular to the crack direction on the work-piece, see Fig. 7.2(a). Subsequently, these profiles are fitted with approximating smooth functions, see Fig. 7.2(b). The maximum of the major in-plane principal strain on the fitted function and the corresponding minor strain, which are marked by the bold dots on the figure, are considered to be limit strains. These quantities also represent the onset of necking in the respective work-piece.

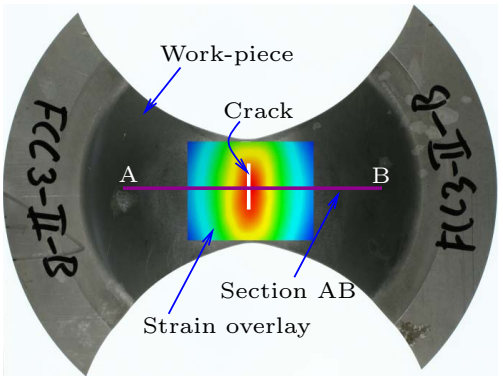

(a) Section AB perpendicular to the crack path and parallel to the localized major strain field ranging from the highest (red) to lowest (blue)

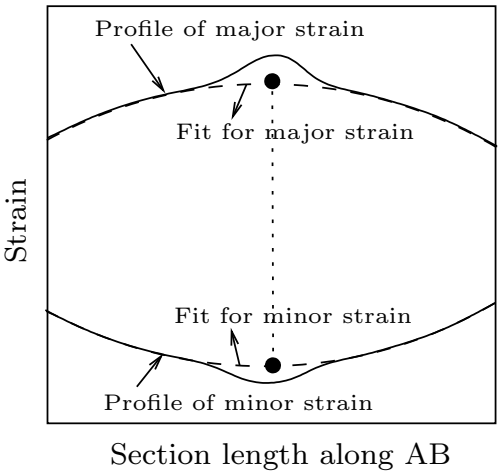

(b) Forming limit (FL) strains obtained from strain profiles

Figure 7.2: Determination of forming limit strains based on the ISO 12004 standard.

Within the present thesis, a new method for establishing the forming limits is advocated. It uses the force-displacement signal of the forming test. A synchronization procedure is then applied to the force-displacement and strain-displacement curves. In this method, the maximum point of the force-displacement curve is assumed to be the point of localization, also referred to as softening point, see Fig. 7.3. This method has the advantage of avoiding fitting or using approximation functions.

As a reference to the forming limit curve, a failure curve is established through a visual inspection of the deformation history. This failure curve indicates the strain levels at the onset of failure defined by the initiation of macro cracks. Additionally, taking advantage of the continuous deformation field measurement from the ARAMIS® system, it was possible to obtain strain

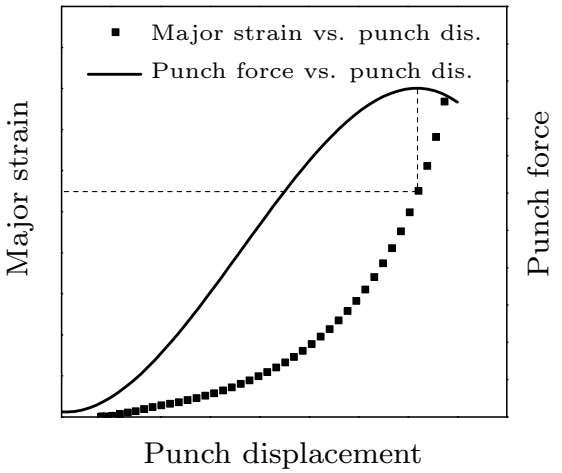

Figure 7.3: New method for the determination of forming limit strains based on synchronization of force and the strain responses.

paths for each work-piece employed in the forming limit tests. These strain paths are established by computing the major and minor in-plane principal strain for selected points in the neighborhood of a crack located at the center of the work-pieces.

7.3 Mechanical response

This section discusses the mechanical responses obtained from the forming limit tests in terms of punch force-displacement curves, strain paths, limit and failure strain curves. The punch force-displacement curves in Fig. 7.4 demonstrate the effects of the work-piece geometries on the force response and the extent of formability. The general observation for both ZE10 and AZ31 is that a decrease in the size of the recess increases the force response. This is a direct result of an increased constraint associated with a decrease in recessed portion of the work-piece.

The linear strain paths obtained from the optical system in Fig. 7.5 are consistent with the constraint imposed by the geometries of the different work-pieces. The small deviation at the early stage of the forming results from bending of the sheet over the hemispherical punch. Thus, the limit strains at the center of the work-pieces can be approximated by offsetting the measured limit strains on the surface of the work-pieces by the positive bending strains.

The fully circular work-piece, for which an equi-biaxial loading condition is assumed, revealed a difference in the magnitudes of the maximum and minimum in-plane principal strains. Similarly, the work-piece with the largest recess, which corresponds to uniaxial-like loading states, resulted in a strain

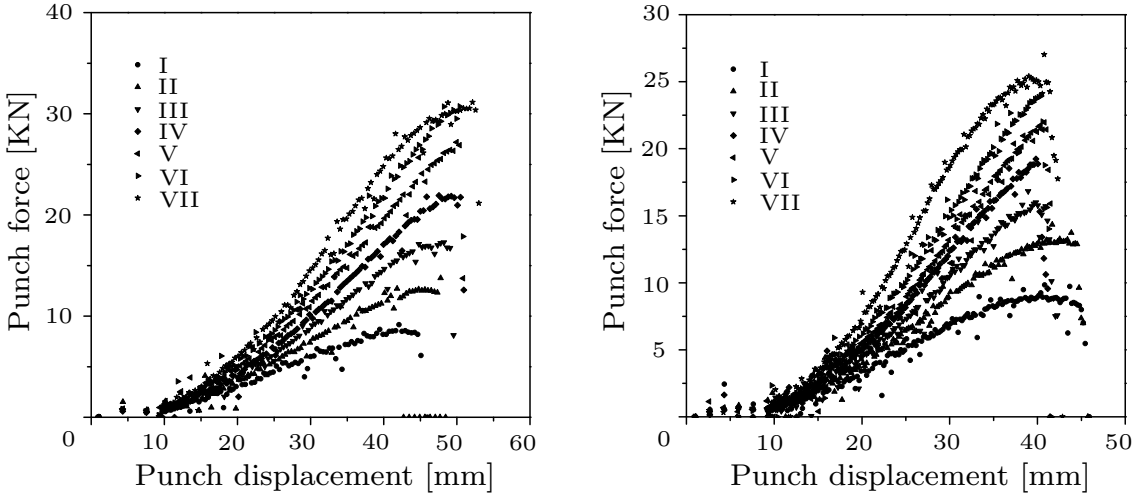

(a) ZE10 Force-displacement (b) AZ31 Force-displacement

Figure 7.4: Force-displacement response of the forming limit tests for ZE10 and AZ31 at 200^oC.

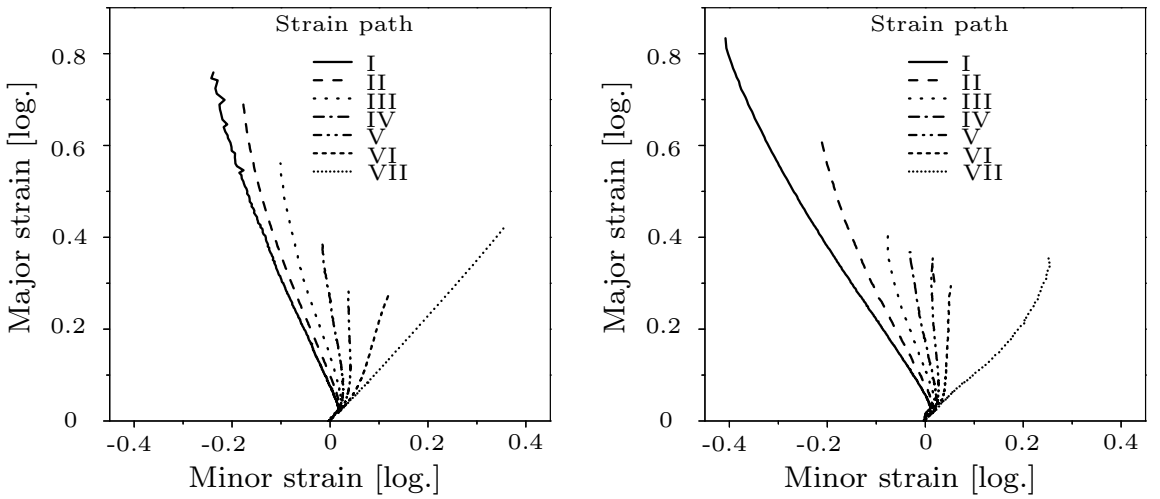

(a) ZE10 strain path (b) AZ31 strain path

Figure 7.5: Strain paths for ZE10 and AZ31 plotted in the in-plane principal strain domain at 200^oC.

ratio different from -2. These observations reaffirm the anisotropic behavior of the materials considered. The FLC in Fig. 7.6 indicates a level of limit strain as high as 0.5 in the uniaxial-like state while about 0.3 for AZ31 and 0.4 for ZE10 limit strain in the equi-biaxial state of deformation. This reveals a level of deformation large enough for a practical forming application. Additionally, it is observed that the difference between the failure strain and the forming limit strain is larger in the negative domain of the FLD than in the positive

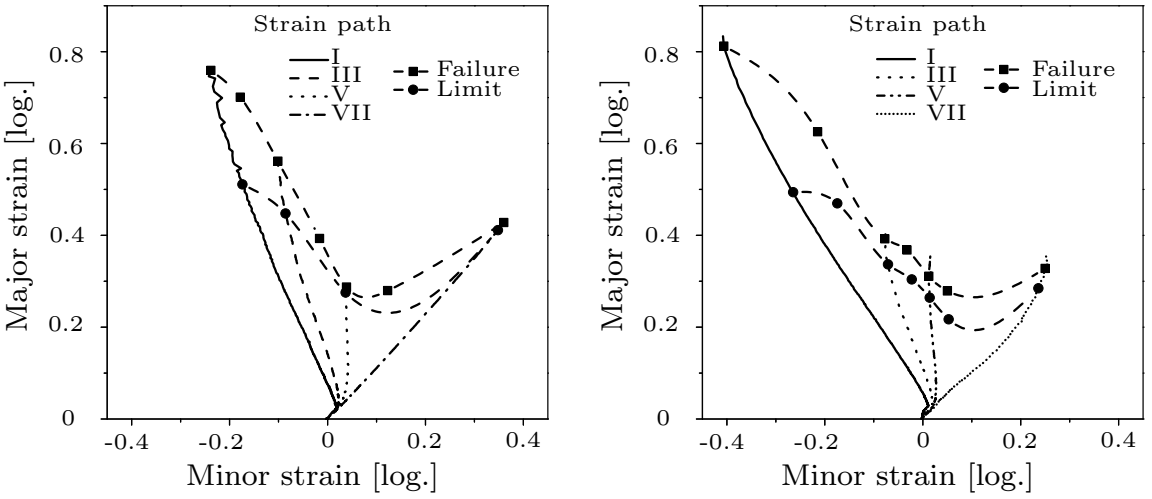

(a) ZE10 strain path

(b) AZ31 strain path

Figure 7.6: Limit and failure strain curves for ZE10 and AZ31 plotted in the in-plane principal strain domain.

domain. This is consistent with the large amount of nonuniform deformation reported during the uniaxial tensile test presented in Chapter 6. However, the strain at localization of the forming test, which is about 0.5, and the strain at the start of the diffused necking of the uniaxial tensile test, which is about 0.1, differ from one another significantly. This observation can be explained by uncertainties, for instance boundary conditions, temperature variations and also a change in the hardening mechanism during the forming test.

8 Model parameter identification

The current chapter deals with the identification of the parameters corresponding to the constitutive model developed in Chapter 3. This is achieved by minimizing the difference between the experimentally observed mechanical response (see Chapter 6 and Chapter 7) and that predicted by the model (see Chapter 3 and Chapter 5).

8.1 Isotropic hardening including strain rate effects

The parameters h_{iso}, ζ, $\Sigma_{\mathrm{o}}^{\mathrm{ref}}$, β and n corresponding to isotropic hardening including strain rate effects are computed by minimizing the target function

$$R_{\Sigma_y} = \sum_k \sum_p \left[{\Sigma_y^{\mathrm{Exp}}}_{kp} - {\Sigma_y^{\mathrm{ref}}}_{p} \left(\frac{{\dot{\overline{\varepsilon}}^{\mathrm{pl}}}_k}{\beta} \right)^n \right]^2 = 0, \tag{8.1}$$

with

$$\Sigma_y^{\mathrm{ref}} = h_{\mathrm{iso}} \left(1 - \exp(\zeta\, \overline{\varepsilon}^{\mathrm{pl}}) \right) + \Sigma_{\mathrm{o}}^{\mathrm{ref}}, \tag{8.2}$$

where the usage of the Mandel stresses (Σ_y^{Exp}) as a representation of the experimentally obtained yield stresses is explained in Remark 11. As a reminder, h_{iso}, ζ, β and n are hardening and rate sensitivity parameters defined in Eq. 3.14, Eq. 3.35 and Eq. 3.36 while $\Sigma_{\mathrm{o}}^{\mathrm{ref}}$ represent the initial yield stress at a reference strain rate β. The target function constitutes the differences between the experimentally measured stress responses ${\Sigma_y^{\mathrm{Exp}}}_{kp}$ and the respective model predictions Σ_y^{ref}. These differences are summed over the number of strain rate measures $k = \{1, 2, 3\}$ (corresponding to the strain rates 0.001/s, 0.02/s and 0.1/s) and the selected discrete points of the equivalent plastic strain p accounting for the evolution of the yield stress. The experimental values employed in the optimization of Eq. 8.1 are obtained from the uniaxial tensile tests within the unform deformation range at an incremental strain value of 0.01 for the specimen oriented in the RD.

Following the optimization of the target function, the identified parameters are presented in Table 8.1 for both ZE10 and AZ31. Moreover, the fitted stress

	h_{iso}(MPa)	$\zeta()$	$\Sigma_{\text{o}}^{\text{ref}}$(MPa)	β(1/s)	$n()$
ZE10	59.212	-8.752	87.385	2.384E−2	0.0454
AZ31	42.069	-21.147	52.140	2.185E−4	0.0841

Table 8.1: Parameters obtained based on minimization of Eq. 8.1.

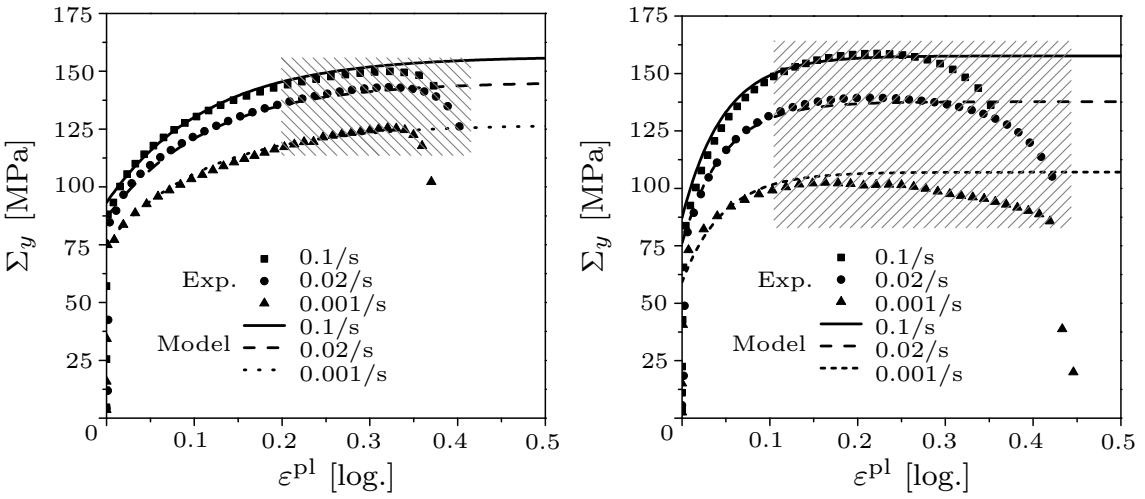

(a) ZE10 (b) AZ31

Figure 8.1: Fitted curves of the true stress responses of the specimens oriented in RD at strain rates of 0.1/s, 0.02/s and 0.001/s for ZE10 and AZ31.

responses established based on the identified parameters are plotted in Fig. 8.1 for the three different strain rates. The parameters resulted in a reasonable fit within the uniform deformation range while the localized deformation is approximated by the extrapolation of the saturating exponential function. Making use of the described computations at the material point level, the uniaxial tensile test has been reanalyzed as a structure. Thus, geometrical effects such as necking are consistently included within the resulting force-displacement. The corresponding engineering stress responses (Force/undeformed cross sectional area) and those of the experiments are compared in Fig. 8.2. Having calibrated the material parameters for uniaxial tension, focus is next on the anisotropy of the material.

Remark 11 *According to Eq. 4.8, for small elastic strains* $\mathbf{F}^{\text{e}} \rightarrow \mathbf{I}$ *and isochoric plastic deformation as implied by the flow rule Eq. 3.25, the determinant of the deformation gradient yields*

$$\text{J} = \text{J}^{\text{e}}\ \text{J}^{\text{pl}} = 1 \ \text{ since } \ \text{J}^{\text{pl}} = 1 \quad \text{and} \quad \text{J}^{\text{e}} = 1.$$

Accordingly, the true stresses (σ_y) *are equivalent to the corresponding Mandel stresses* (Σ_y). *Therefore, the Mandel stresses* (Σ_y) *can be used in the opti-*

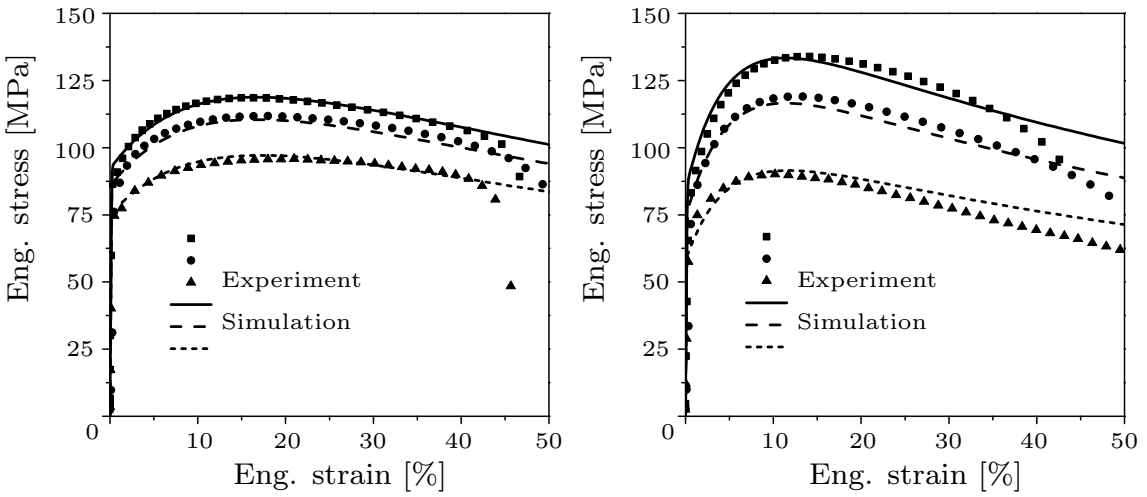

(a) ZE10 (b) AZ31

Figure 8.2: Comparison between experimental and numerically predicted engineering stress responses (Force/undeformed cross sectional area) for uniaxial tensile tests of ZE10 and AZ31 at strain rates of 0.1/s, 0.02/s and 0.001/s for specimens oriented in RD.

mization scheme. However, it bears emphasis that this simplification is only used for computing the Mandel stresses from the uniaxial exerperiments. The final model does account for large strain effects - also for large elastic strains.

8.2 Material anisotropy and distortional hardening

The model parameters discussed here are correlated to the components of the transformation tensors $\mathbb{H}_1$ and $\mathbb{H}_2$ which in turn represent the distortional hardening. These tensors exhibit certain properties corresponding to the material symmetry and pressure invariance, cf. (Dafalias, 1979; Cazacu & Barlat, 2003).

8.2.1 Properties of the distortional hardening tensors

Assuming the existence of a hardening potential describing the distortional effects implies major symmetry of $\mathbb{H}_1$ and $\mathbb{H}_2$. Furthermore, since the Mandel stresses are symmetric (isotropic elastic neo-Hookean model is used), $\mathbb{H}_1$ and $\mathbb{H}_2$ have also a minor symmetry. Thus,

$$\mathbb{H}_{klmn} = \mathbb{H}_{lkmn} = \mathbb{H}_{klnm} = \mathbb{H}_{mnkl} \quad \text{for} \quad \mathbb{H}_1 \quad \text{and} \quad \mathbb{H}_2 \tag{8.3}$$

holds. Additionally, the pressure invariance results in the condition

$$\mathbb{H}_{kkmn} = 0, \tag{8.4}$$

with $k, l, m, n = \{1, 2, 3\}$. The aforementioned conditions are explored to reduce the large number of model parameters. More specifically, the eighty-one components in each transformation tensors can be reduced to fifteen. Moreover, assuming invariance with respect to any transformation belonging to the orthotropic symmetry group of the material, the components are further reduced to six. Thus, the simplified fourth-order tensors $\mathbb{H}_i$ in their Voigt form $\mathcal{H}_i$ can be represented as

$$\mathcal{H}_i = \begin{bmatrix} (c_2+c_3)/3 & -c_3/3 & -c_2/3 & 0 & 0 & 0 \\ -c_3/3 & (c_3+c_1)/3 & -c_1/3 & 0 & 0 & 0 \\ -c_2/3 & -c_1/3 & (c_1+c_2)/3 & 0 & 0 & 0 \\ 0 & 0 & 0 & c_4 & 0 & 0 \\ 0 & 0 & 0 & 0 & c_5 & 0 \\ 0 & 0 & 0 & 0 & 0 & c_6 \end{bmatrix} \text{ with } \; i = 1, 2, \tag{8.5}$$

where c_j with $j = 1...6$ are the reduced six components of the transformation tensors different for $\mathcal{H}_1$ and $\mathcal{H}_2$. The relations between the model parameters corresponding to the second invariant of CaBa2004 model (a_i with $i = \{1, ..., 6\}$) and those of the current model take the form

$$\begin{bmatrix} a_1 \\ a_2 \\ a_3 \\ a_4 \\ a_5 \\ a_6 \end{bmatrix} = \begin{bmatrix} 1/3(2{c_3}^2 - c_1c_2 + c_1c_3 + c_2c_3) \\ 1/3(2{c_1}^2 - c_2c_3 + c_1c_2 + c_1c_3) \\ 1/3(2{c_2}^2 - c_1c_3 + c_1c_2 + c_2c_3) \\ {c_4}^2 \\ {c_5}^2 \\ {c_6}^2 \end{bmatrix}. \tag{8.6}$$

According to Eq. 8.6, although both models show the same number of parameters,the relations are established through second order functions. For the third invariant, however, the eleven parameters of CaBa2004 (b_j with $j = \{1, ..., 11\}$) are reduced to six in the current model due to additional constraints. Thus, c_j with $j = \{1, ..., 6\}$ of $\mathcal{H}_2$ represent a subset of the eleven parameters of the

CaBa2004 model through third order functions, i.e.,

$$\begin{bmatrix} b_1 \\ b_2 \\ b_3 \\ b_4 \\ b_5 \\ b_6 \\ b_7 \\ b_8 \\ b_9 \\ b_{10} \\ b_{11} \end{bmatrix} = \begin{bmatrix} 1/3(2c_2{c_3}^2 - c_1{c_3}^2 + c_1{c_2}^2 + c_3{c_2}^2) \\ 1/3(2c_3{c_2}^2 - c_1{c_2}^2 + c_1{c_3}^2 + c_2{c_3}^2) \\ 1/3(2c_3{c_1}^2 - c_2{c_1}^2 + c_1{c_3}^2 + c_2{c_3}^2) \\ 1/3(2c_1{c_3}^2 - c_2{c_3}^2 + c_2{c_1}^2 + c_3{c_1}^2) \\ {c_1{c_4}^2} \\ {c_3{c_6}^2} \\ {c_2{c_6}^2} \\ {c_1{c_5}^2} \\ 1/2(c_1{c_5}^2 + {c_5}^2c_3) \\ 1/2(c_1{c_4}^2 + {c_4}^2c_2) \\ (c_4c_5c_6) \end{bmatrix}. \tag{8.7}$$

Based on the conjugacy relation in Eq. 3.14 and Eq. 3.32, the transformation tensors $\mathbb{H}_i$ can be rewritten as

$$\mathbb{H}(\bar{\varepsilon}^{\mathrm{pl}}) = h_{\mathrm{d}}\ \mathbb{E}(\bar{\varepsilon}^{\mathrm{pl}}). \tag{8.8}$$

Furthermore, assuming a unit value for the distortional hardening modulus $h_{\mathrm{d}} = 1$, c_j can be expressed as a function of the equivalent plastic strain, cf. Graff (2007). For that purpose, a suitable function is employed. In this work, an exponential function of the type

$$c_j = A_j + B_j \left(1 - \exp(-C_j\ \bar{\varepsilon}^{\mathrm{pl}})\right) \tag{8.9}$$

is adopted, where A_j, B_j and C_j with $j = \{1...6\}$ are the model parameters different for $\mathbb{H}_1$ and $\mathbb{H}_2$.

Remark 12 *The special case of the model parameters $c_j = 1$ results in an isotropic model.*

Remark 13 *For a plane stress condition, which is a reasonable assumption in most sheet forming processes, the six components of the transformation tensor can further be reduced to four.*

8.2.2 Method of identification

The identification of the parameters defining the fourth-order tensors $\mathbb{H}_i$ is performed through an optimization procedure. More precisely, a constrained genetic algorithm is adopted. A detailed description of such methods can be

found in Banabic (2007) (Section 2). The optimization method employs an objective function of the least square-type

$$\Gamma = \sum_q \sum_p \left[\mu_{qp}^{\Sigma} \left(\Sigma_{qp}^{\mathrm{Set}} / \Sigma_{qp}^{\mathrm{Exp}} - 1 \right)^2 + \mu_{qp}^{r'} \left(r'^{\mathrm{Set}}_{qp} / r'^{\mathrm{Exp}}_{qp} - 1 \right)^2 \right]. \quad (8.10)$$

This function incorporates sums accounting for stresses $\Sigma_{qp}^{()}$ as well as r-values. The sums run over the number of specimen orientations q considered during the uniaxial tensile tests and the selected discrete points of the equivalent plastic strain p accounting for the evolution of the yield loci. μ_{qp}^{Σ} and $\mu_{qp}^{r'}$ are weighting factors to control the contribution from the stress and r-value, respectively. The superscripts Exp and Set refer to the reference values obtained from experiment and those related to the predictions of the model, respectively. In Eq. 8.10, r' is a modified r-value obtained from the ratio of the strain rates. This can be approximated by the derivatives of the yield function as

$$r' = \frac{\dot{\varepsilon}_w^{\mathrm{pl}}}{\dot{\varepsilon}_t^{\mathrm{pl}}} \approx -\frac{\sin^2\theta\, \partial_{\Sigma_{xx}} f - \sin 2\theta\, \partial_{\Sigma_{xy}} f + \cos^2\theta\, \partial_{\Sigma_{yy}} f}{\partial_{\Sigma_{xx}} f + \partial_{\Sigma_{yy}} f}, \quad (8.11)$$

where $\dot{\varepsilon}_w^{\mathrm{pl}}$ and $\dot{\varepsilon}_t^{\mathrm{pl}}$ are the rates of the plastic strains in width and thickness direction of the tensile test specimens. The angle θ is the orientation of the tensile test specimens with respect to the rolling direction. Evidently, in case of a constant r-value Eq. 8.11 leads to the conventional r-value computed from the ratio of strains.

The optimization of the objective function in Eq. 8.10 is complemented by constraints imposed to ensure the validity of the identified model constants. These constraints include the convexity of the yield function and the dissipation inequality required for the thermodynamic consistency, as mentioned in Section 3.2.2.3. Details about the incorporation of such constraints into the optimization problem Eq. 8.10 are given in Remark 14. For guaranteeing the convexity of the yield surfaces, the Hessian matrix (represented by the second-order derivative of the yield function with respect to the stress tensor) is required to be positive semi-definite. Equivalently, this can be achieved by requiring nonnegative eigenvalues η of the Hessian matrix, i.e.,

$$\det\left(\frac{\partial^2 f}{\partial \boldsymbol{\Sigma}^2} - \eta \mathbb{I} \right) = 0. \quad (8.12)$$

The nonnegative mechanical dissipation is also enforced by imposing Eq. 3.33. Additionally, the parameters are constrained so that the yield loci do not intersect with each other.

Remark 14 *Within the optimization scheme the different constraining conditions such as the convexity of the yield function, the nonnegative dissipation as well as nonintersecting yield surfaces are implemented as follows.*

- *The **convexity** constraint is imposed by two different approaches. The first approach evaluates the Hessian matrix Eq. 8.12 for the two in-plane principal stresses at prescribed discrete strain levels and loading cases. Then the computed eigenvalues are ensured to be greater or equal to zero. The second approach considers a set of three different but closely positioned discrete points on the yield surface and at a given loading interval. Convexity is fulfilled if the straight line connecting the two end points of the interval intersect or cross a line drawn between the origin of the yield surface and the third point on the interval.*
- *The **nonnegative dissipation** is ensured by evaluating Eq. 3.33 for all discrete strain and loading cases corresponding to the yield surfaces.*
- ***Intersections** of the yield surfaces are prevented by ensuring non-softening stress responses for all loading cases. This is achieved by computing the stress components at a given loading direction for discrete but monotonically increasing strains.*

8.3 Mechanical response of the calibrated constitutive models

This section illustrates the mechanical response as predicted by the calibrated material model. Following the relatively small strain rate effect on the material anisotropy, the results are only shown for a strain rate of 0.02/s.

8.3.1 Isotropic von Mises-type and Drucker-type models

As it has been pointed out in Remark 12, isotropic versions of the current model can be established by setting the model parameters to the values in Tables 8.2(a) for von Mises and 8.2(b) for isotropic Drucker-type models capturing the stress-differential effect. The resulting responses from the model are presented in terms of iso-strain curves of the in-plane principal stresses, see Fig. 8.3 and Fig. 8.4. The observed mismatch between the experimental and the computed stresses in transverse direction in case of ZE10 is more pronounced than AZ31. Even more importantly, the disregard to properly account for r-values in the isotropic models justifies the need for anisotropic model.

(a) von Mises

Iso-von Mises	$\mathbb{H}_1$	$\mathbb{H}_2$
c_1	1	0
c_2	1	0
c_3	1	0
c_4	1	0
c_5	1	0
c_6	1	0

(b) Drucker

Iso-Drucker	$\mathbb{H}_1$	$\mathbb{H}_2$
c_1	1	1
c_2	1	1
c_3	1	1
c_4	1	1
c_5	1	1
c_6	1	1

Table 8.2: Parameter sets corresponding to the von Mises and Drucker-type isotropic material models.

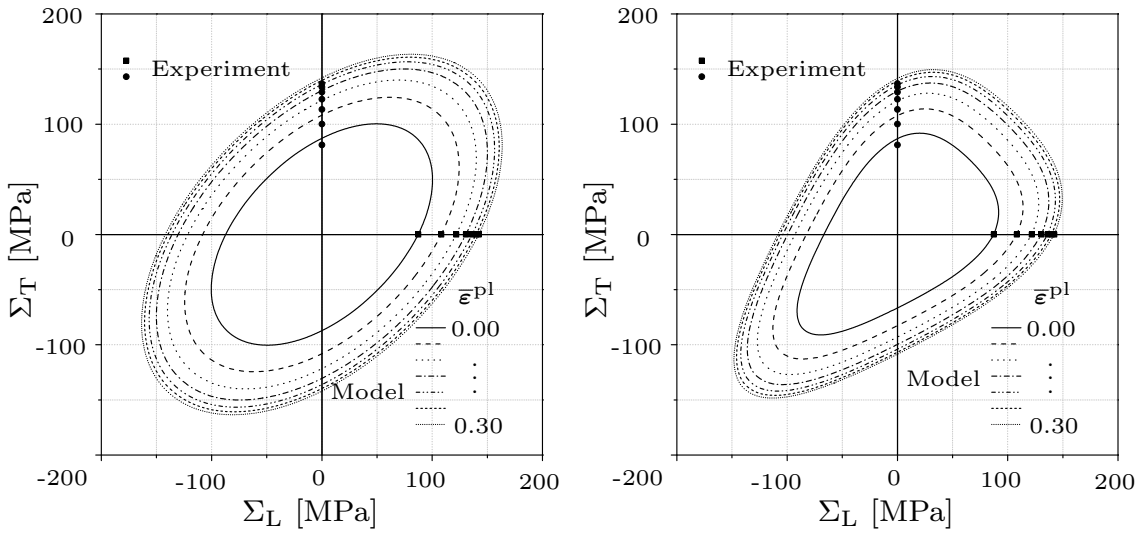

(a) von Mises (b) Drucker

Figure 8.3: Iso-strain curves of in-plane principal stresses from isotropic von Mises and Drucker-type models compared to experimental stress responses of ZE10.

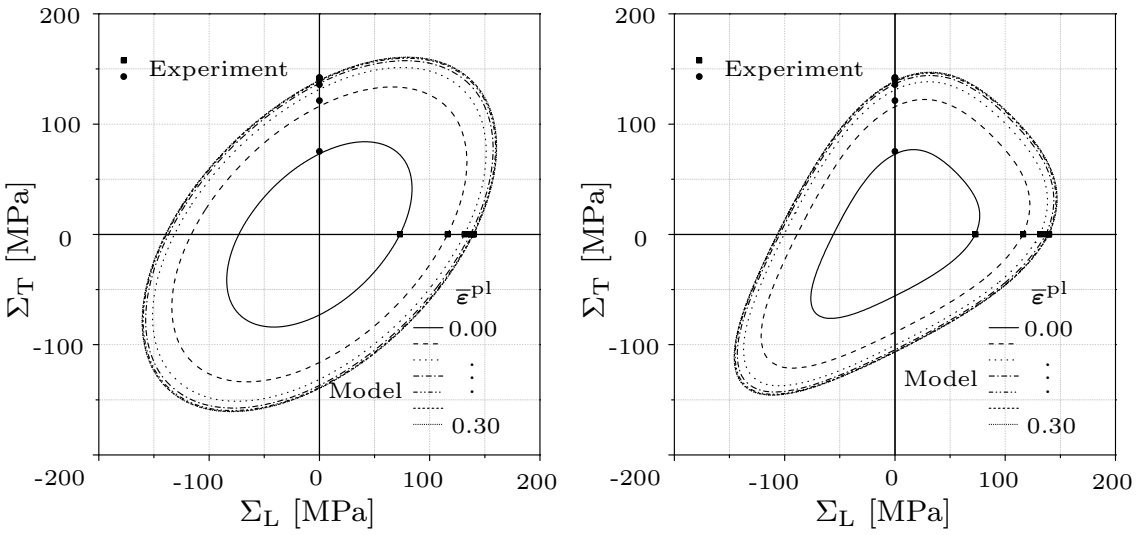

(a) von Mises (b) Drucker

Figure 8.4: Iso-strain curves of in-plane principal stresses from isotropic von Mises and Drucker-type models compared to experimental stress responses of AZ31.

8.3.2 Modified anisotropic Cazacu and Barlat-type model combined with distortional hardening

The parameters of the novel model are identified for both ZE10 and AZ31, see Table 8.3. The corresponding iso-strain curves of the stress responses are plotted in Fig. 8.5. From the figure, it can be seen that the model captures the anisotropic stress responses well. Moreover, the modified r-values (r') are reproduced and compared to those obtained from the experiment, see Fig. 8.7. The comparison shows a good agreement between the experiment and the prediction. It should also be noted that the model is capable of capturing the plastic strain-dependency of the computed r-values. Additionally, Fig. 8.6 demonstrates the comparison of the predicted stress responses as a function of the specimen orientations with those measured experimentally. From the figure, it can be seen that the model captures the stress response in the 45^o direction for the specified strain range very well. The convexity constraint imposed during the optimization procedure was indeed satisfied as shown in Fig. 8.8. The figure shows convex three-dimensional plots of the evolving yield surface.

(a) ZE10

	$\mathbb{H}_1$			$\mathbb{H}_2$		
	A	B	C	A	B	C
c_1	-4.5	2.7	0	1.0	-5.9	6.5
c_2	-4.1	-6.5	0.1	1.2	-2.2	3.2
c_3	-3.5	-3.1	8.8	5.8	0.0	3.1
c_4	4.1	1.9	10.4	-5.4	3.4	3.9
c_5	1	0	0	0	0	0
c_6	1	0	0	0	0	0

(b) AZ31

	$\mathbb{H}_1$			$\mathbb{H}_2$		
	A	B	C	A	B	C
c_1	1.7	-1.9	0.3	2.1	-0.8	4.4
c_2	1.6	2.5	0.0	-1.5	0.6	0.8
c_3	-3.2	-2.4	3.1	0.5	2.5	1.0
c_4	1.6	1.7	2.8	-0.9	-1.2	3.3
c_5	1	0	0	0	0	0
c_6	1	0	0	0	0	0

Table 8.3: Parameter sets corresponding to the novel anisotropic material model.

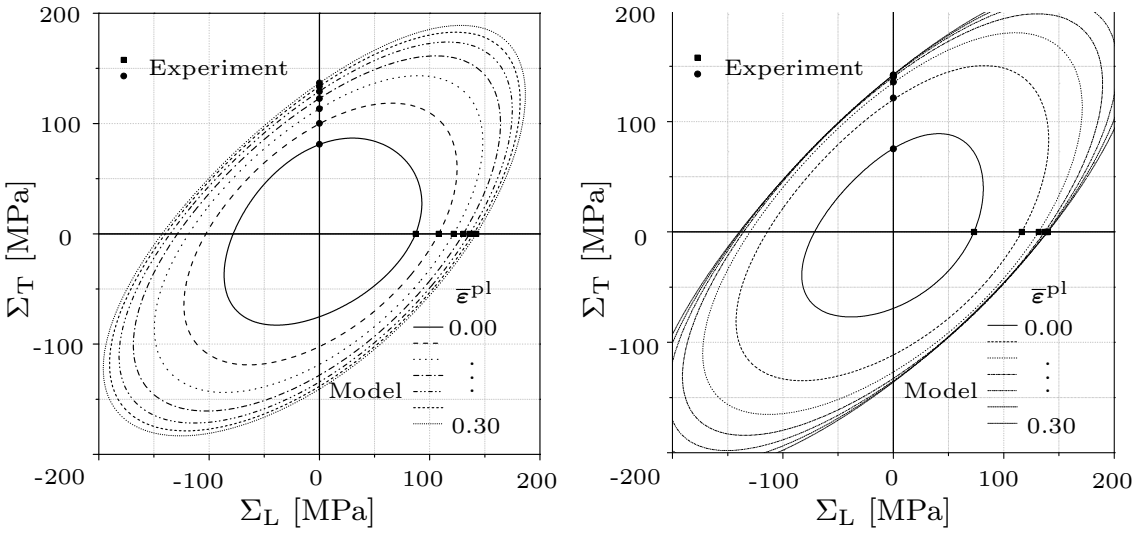

(a) ZE10 (b) AZ31

Figure 8.5: Iso-strain curves of in-plane principal stresses based on the novel anisotropic constitutive model, see Table 8.3.

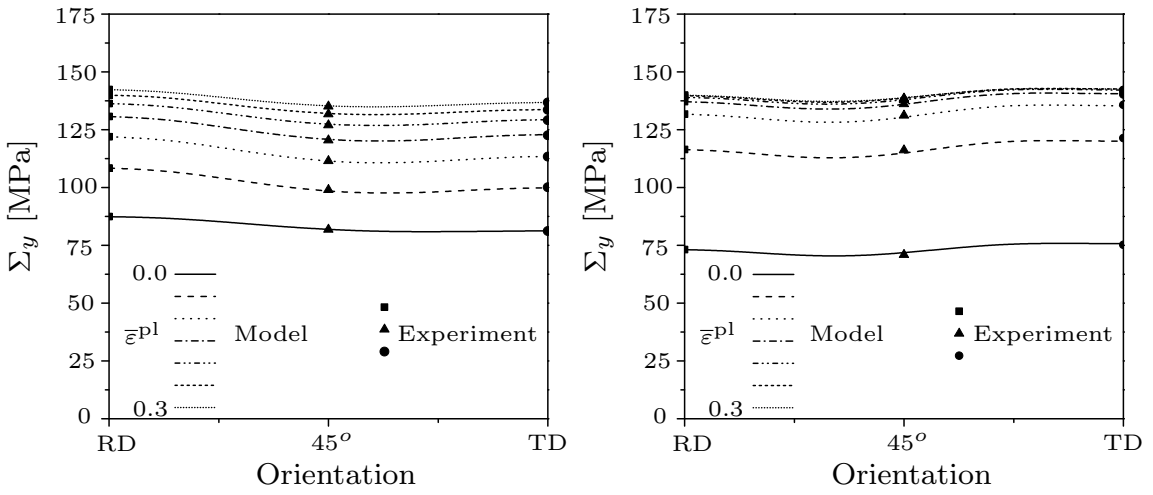

(a) ZE10 (b) AZ31

Figure 8.6: Stress responses predicted by the novel anisotropic material model (see Table 8.3 for the material parameters) as a function of specimen orientation for strain levels ranging from 0 to 0.3 at a strain rate of 0.02/s.

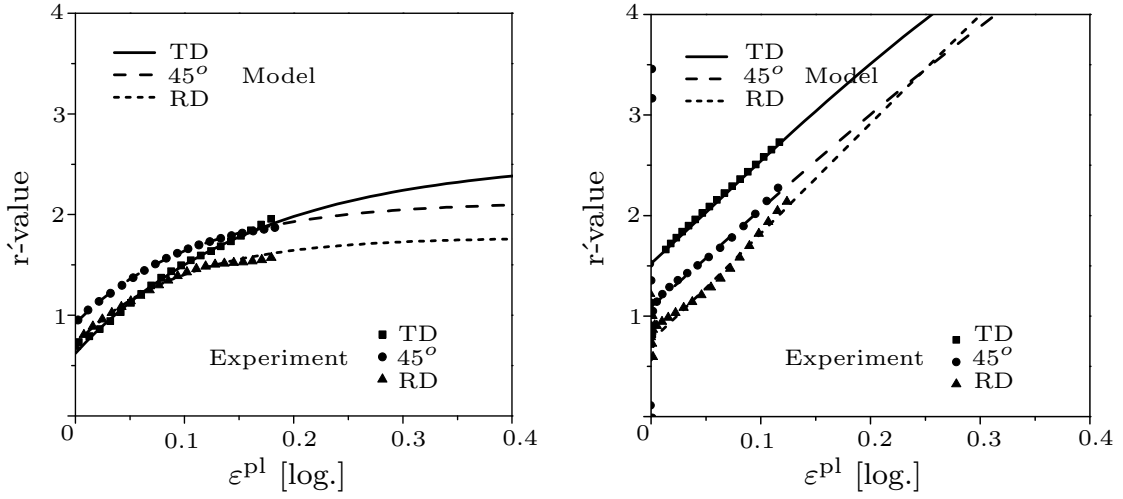

(a) r'-value ZE10 (b) r'-value of AZ31

Figure 8.7: r'-values predicted by the novel anisotropic material model (see Table 8.3 for the material parameters) as a function of the plastic strain at a strain rate of 0.02/s.

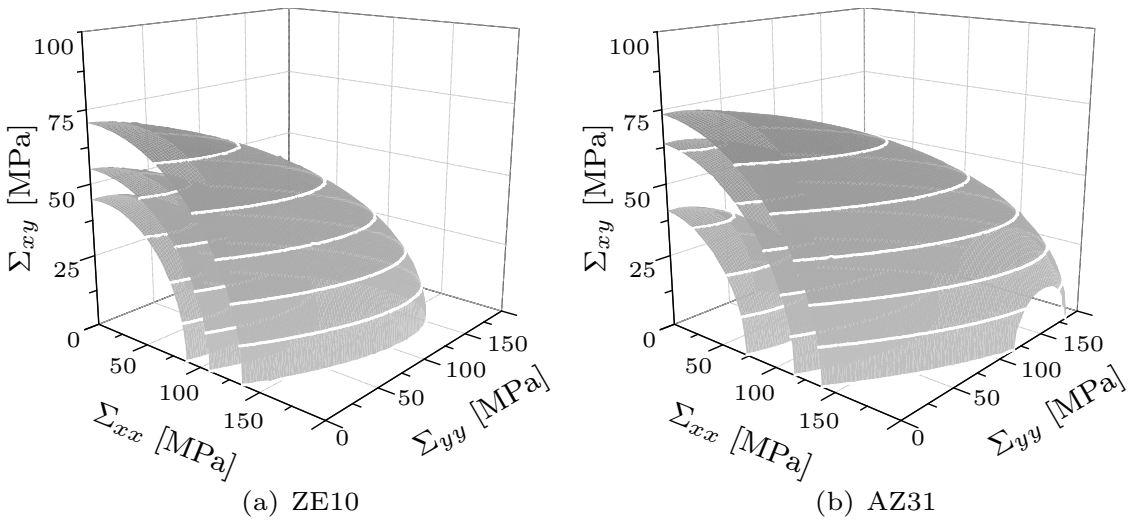

(a) ZE10 (b) AZ31

Figure 8.8: Convex iso-strain contour surfaces of the stress response predicted by the novel anisotropic material model (see Table 8.3 for the material parameters) at a strain rate of 0.02/s.

It is observed that the linearly increasing r-value for AZ31 at large strain levels results in significantly high tensile biaxial stress responses, see Fig. 8.5(b) and Fig. 8.7(b). This can be explained by the change in the normals to the yield loci at the uniaxial stress states, which in turn are correlated to the increasing r-value. To further demonstrate the aforementioned effect of the r-value, the model is re-calibrated based on a set of constant r-values taken at strain levels of 0.03, 0.08 and 0.12, see Table 8.4. Based on the re-calibration, the yield loci obtained at a strain level of 0.15 for the different r-values are compared in Fig. 8.9. From the figure, it can be concluded that the higher the r-value the higher the tensile biaxial stresses become. The corresponding model parameters together with the observed responses can be found in Appendix C.

r at the respective orientation			
$\overline{\varepsilon}^{\mathrm{pl}}$	RD	45^o	TD
0.03	0.88	1.09	1.49
0.08	1.18	1.40	1.86
0.12	1.39	1.58	2.09

Table 8.4: r-values taken at strain levels of 0.03, 0.08 and 0.12 considered during re-calibration of the model for AZ31, see Appendix C.

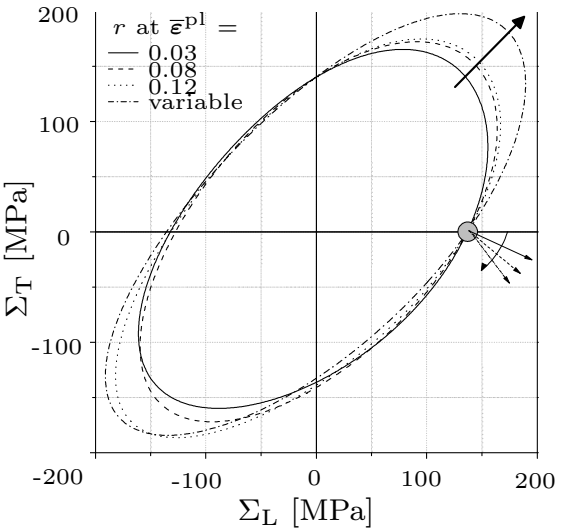

Figure 8.9: Effect of the r-value on the biaxial tensile stress responses predicted by the novel anisotropic material model (see Table 8.3 and Appendix C for the material parameters) at a strain level of 0.15 for AZ31.

Remark 15 *It should be noted that, for a more accurate description of the mechanical response including the biaxial yield behavior and the tension-compression asymmetry, additional data from biaxial tension and compression experiments are required.*

9 Application of the constitutive models

The current chapter deals with the application of the calibrated constitutive models in sheet forming simulations. The simulations correspond to the Nakazima-type forming limit tests detailed in Chapter 7. First, the general aspects considered in sheet forming simulations are discussed briefly. This is followed by comparisons of the mechanical responses obtained from the forming simulations based on the hyper- and hypoelasoplastic models. Finally, the capability of the constitutive models for predicting forming limits is evaluated.

9.1 General aspects of sheet forming simulations

Sheet forming is a fairly complex process. The responses obtained from such processes are influenced by several aspects such as finite element modeling of the forming process, forming temperature, loading condition and friction. Within the description of the finite element modeling, special attention is given to the interaction conditions between the forming tools and the work-piece. Numerical aspects, such as the chosen type of finite elements and mesh size are also considered.

9.1.1 Finite element modeling of the forming process

The finite element modeling of the forming process follows directly from the forming limit experimental setup described in Chapter 7. Thus, the model is composed of three tools, namely the die, the holder and the punch, together with a work-piece, see Fig. 9.1(a). According to Fig. 9.1(b), the work-piece adopts seven different geometries for covering the complete range of the forming limit diagram. The tools and the work-pieces are assembled in a 3D modeling space and for reducing the computational costs, an orthogonal symmetry is assumed. In practice, the tools undergo a negligible deformation. Therefore and in contrast to the work-piece, they are represented by rigid bodies. It should also be pointed out that isothermal conditions are assumed within the simulations.

The interaction between the tools and the work-piece is an important aspect

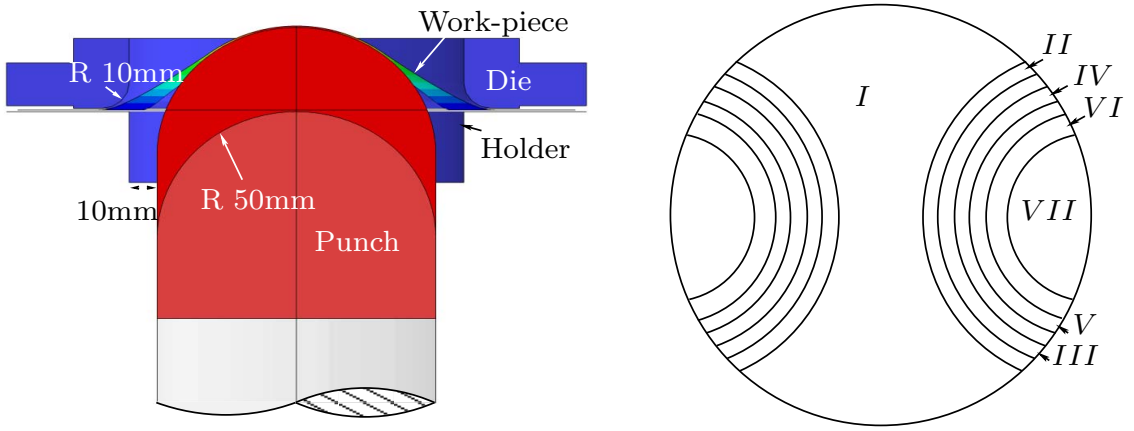

(a) Geometric setup

(b) Work-piece geometries

Figure 9.1: Forming limit test setup as proposed by Nakazima (see. Nakazima et al. (1971)) and work-piece geometries by Hasek (see. Hasek (1973)).

in the forming process. The simulations performed in this work adopt the so-called soft contact condition with an exponentially applied pressure as a function of clearance, see ABAQUS® manual.

In order to clamp the work-piece, a normal force of 300kN is exerted by the flat region of the die onto the work-piece with the holder fixed in place. The tangential constraint is applied by introducing a Coulomb-type friction. The interaction between the punch and the work-piece is also governed by friction and a pressure exerted by the motion of the punch. The magnitude of friction is identified by comparing mechanical responses obtained from numerical simulation to those measured experimentally. Finally, the constraint conditions are expected to ensure a polar localization as recommended by the ISO standard.

9.1.2 Element-type and mesh size

Sheet forming processes can be conveniently modeled by shell-type finite elements. For this reason, the standard ABAQUS® elements S4 are used. These are four node shell elements having three translational and three rotational degrees of freedom at each node. In order to increase the computational efficiency the finite element type S4R based on a reduced integration is employed in the present work. For justifying the choice of the element type, additional fully three-dimensional computations based on the standard eight node element C3D8 are also considered. The bending effect in the fully 3D discretization is considered by introducing at least two layers of elements across the thickness. The responses obtained from the different finite element formulations in

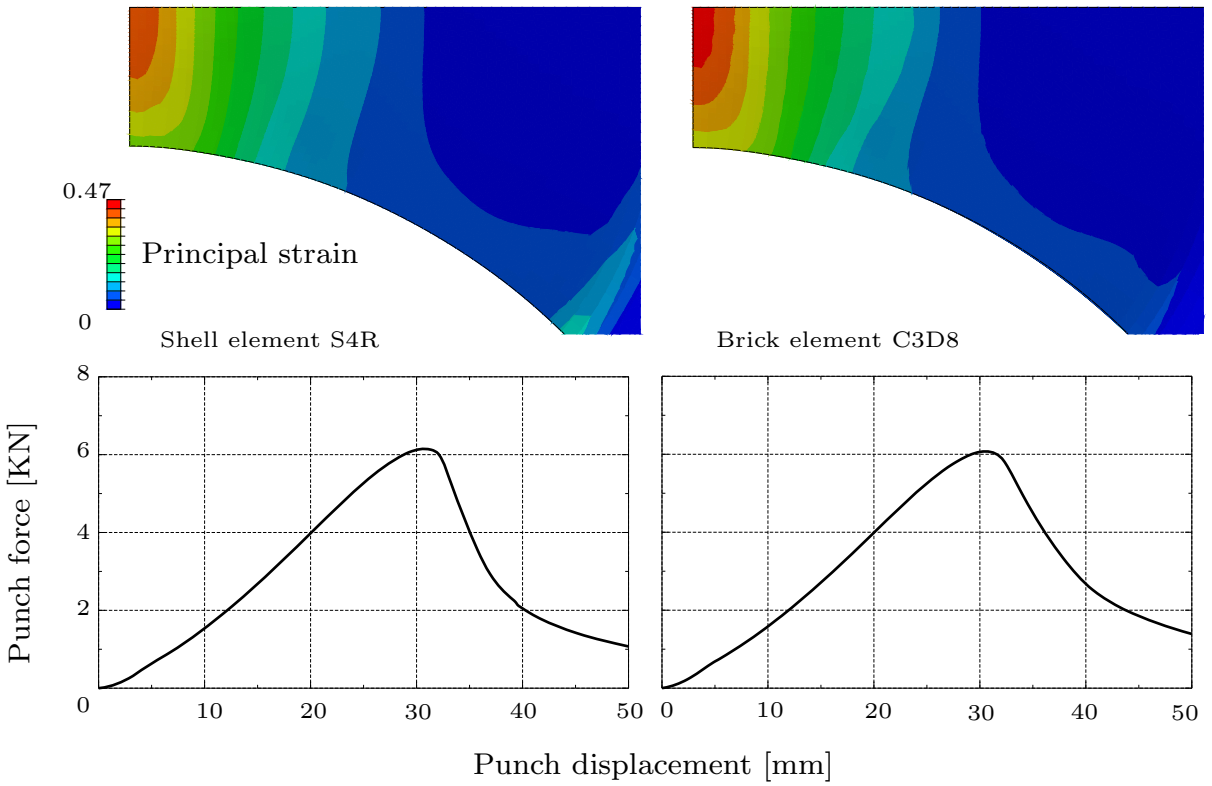

Figure 9.2: Effect of element-type on the computed mechanical response. Upper pictures: distribution of the principal strain at a punch displacement of 30mm. Lower pictures: punch force vs. punch displacement (work-piece geometry I).

terms of the force-displacement curves and the strain field taken at the punch displacement of 30mm are presented in Fig. 9.2. Accordingly, the choice of a conventional shell element is considered to be reasonable. Thus, all subsequent forming simulations adopt the S4R shell elements.

Furthermore, simulations for different mesh sizes are performed in order to optimize the computational cost against the accuracy of the simulation results. For that purpose, three mesh sizes corresponding to 30, 50 and 70 percent of the 1.3mm work-piece thickness designated as MS30, MS50 and MS70, respectively are employed. The corresponding stress fields and punch forces are plotted in Fig. 9.3. From the contour figures, it can be seen that there is only a small difference in the responses of MS30 and MS50. This difference, however, slightly increases in case of MS70. Thus, all following simulations adopt a mesh size MS50.

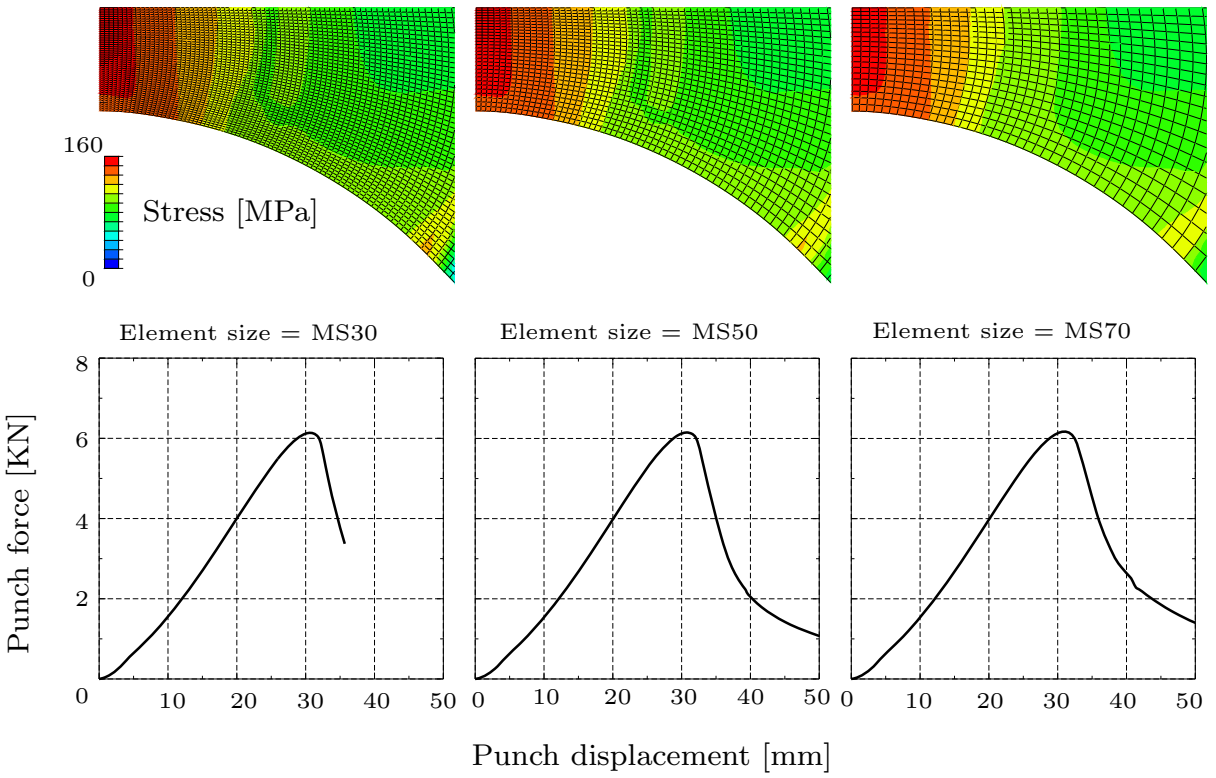

Figure 9.3: Effect of mesh size on the the computed mechanical response. Upper pictures: distribution of the stress at a punch displacement of 30mm. Lower pictures: punch force vs. punch displacement (work-piece geometry I).

9.1.3 Process parameters

A forming process is affected by a set of process parameters, such as temperature, loading history and friction between the punch and the work-piece. Since the tests have been performed at nearly constant temperatures the effect of temperature variation is not considered. Moreover, loading is controlled by the specific shape of the work-pieces and the constant punch stroke. Having defined the temperature together with the loading through the work-piece geometry and punch stroke, the friction effect can be investigated by performing simulations with different friction coefficients. Fig. 9.4 shows the major principal strain field on the surface of the symmetric quarter of the work-piece together with the punch force for different friction coefficients, namely 0.00, 0.05 and 0.10. The displayed strain fields correspond to the peak points within the punch force vs. punch displacement curves. From the figure, it can be seen that the point of strain concentration, hence localization, moves away from the center of the work-piece with an increasing friction coefficient. It is also observed that the increase in friction increases the punch force. Additionally, the effects of friction was also analyzed experimentally. The results of such

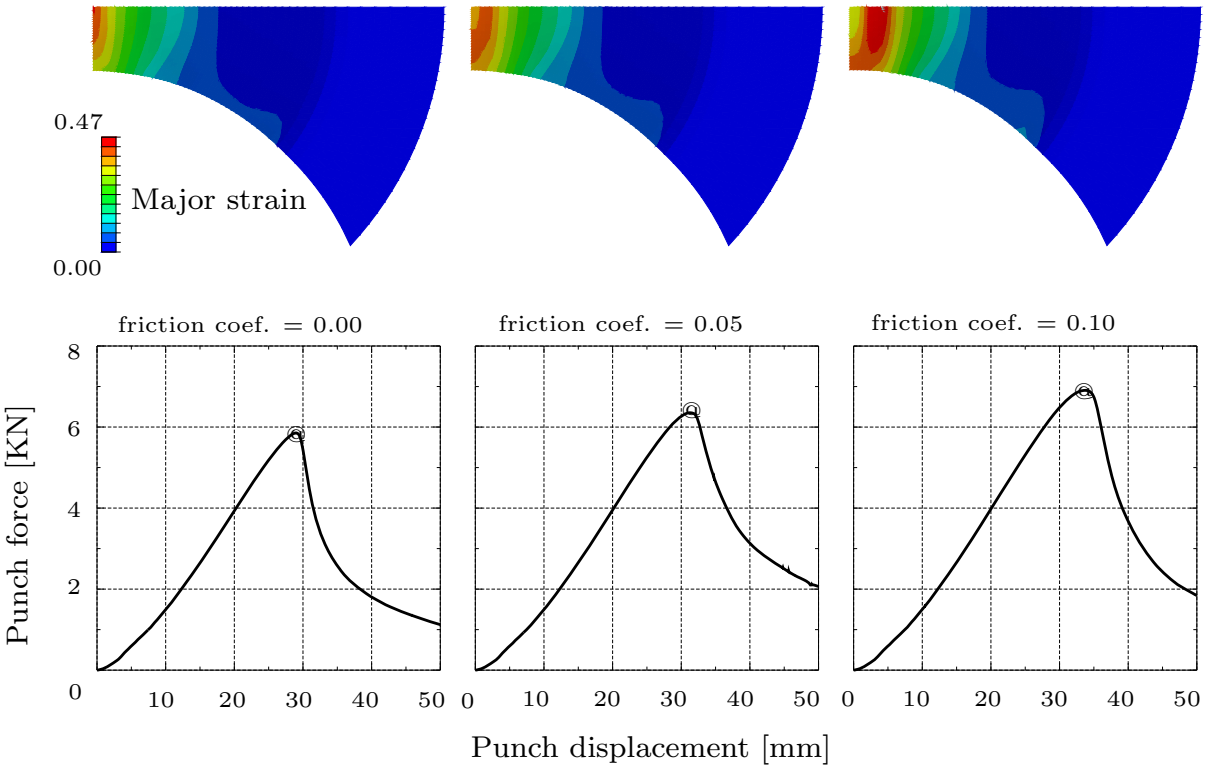

Figure 9.4: Effect of the friction coefficient between the work-piece and the punch on the computed mechanical response. Upper pictures: distribution of the principal strain at a punch displacement of 30mm. Lower pictures: punch force vs. punch displacement (work-piece geometry I).

experiments are shown in Fig. 9.5 for two methods of lubrication and the corresponding friction coefficients, namely a single layer of Boron-Nitride (BN) and three layers of lubricants (Tribo system with Teflon and Oil). From the figure it can be seen that the BN lubrication led to a higher friction coefficient in the simulation. Consequently, the strain localization occurred far from the center and thus the visible crack on the formed work-piece. In contrast, the Tribo system of lubrications resulted in the desired strain localization right at the center of the work-piece. The corresponding well matched responses from the simulation are obtained for a friction coefficient close to zero.

9.2 Comparison of hyperelastoplastic and hypoelastoplastic models

The hypo- as well as the hyperelastoplastic constitutive models have been employed for simulating the Nakazima-type sheet forming tests. As plotted in

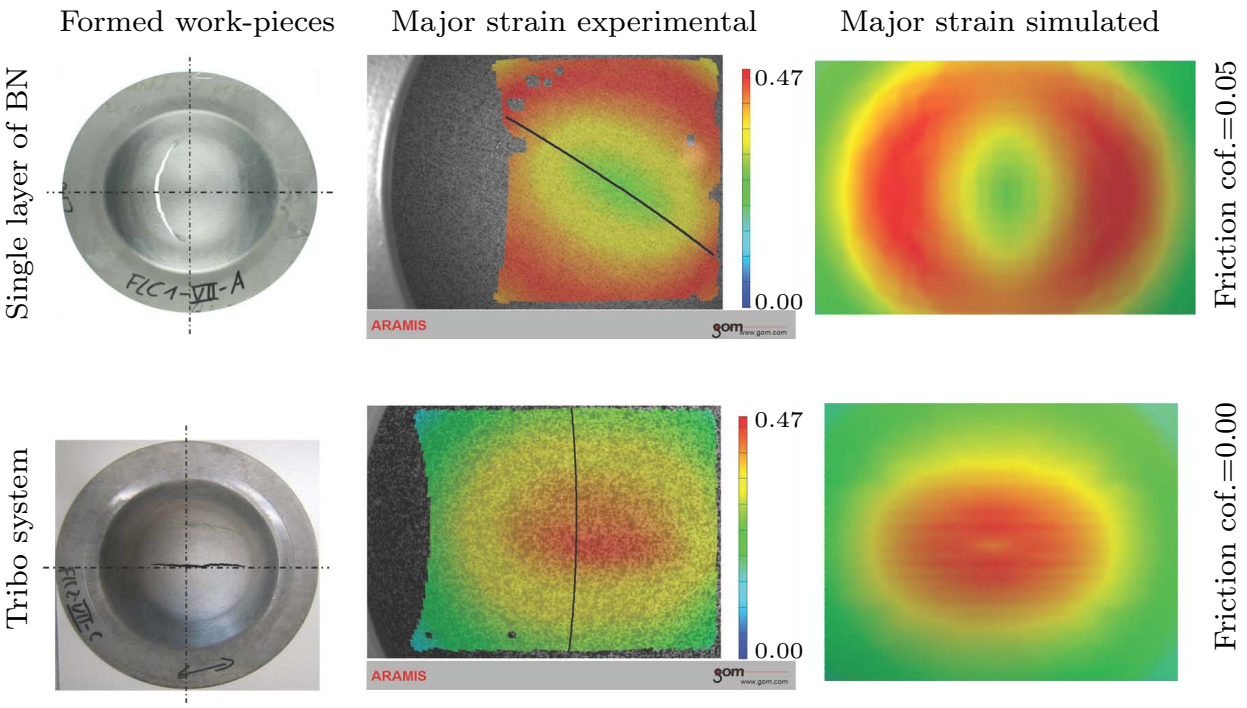

Figure 9.5: Effect of the lubrication/friction between the work-piece and the punch on the mechanical response. Upper pictures: formed work-piece, experimentally measured distribution of the principal strain and those of the model for a single layer of lubrication with Boron-Nitride (BN). Lower pictures: formed work-piece, experimentally measured distribution of the principal strain and those of the model for three layer of lubrication (Tribo system). (work-piece geometry VII). The lines drawn over the experimentally measured strain distributions correspond to sections perpendicular to the visible cracks on the work-pieces.

Fig. 9.6, the punch force-displacement responses obtained from both models are in good agreement. As can be seen from this figure, the physical inconsistencies implied by the hypoelastoplastic model are not pronounced here. This can be explained by a relatively small elastic deformation compared to the plastic deformation. Thus, the hypoelastoplastic model can also be used.

9.3 Forming limit prediction

In this section forming limits are numerically computed by using the novel anisotropic constitutive models. The sensitivity of the limit strains with respect to the magnitude of the initial imperfection required within the Marciniak and Kuczynski criterion is also studied. Subsequently, the corresponding limit strains are evaluated and compared to those obtained from the experiment by

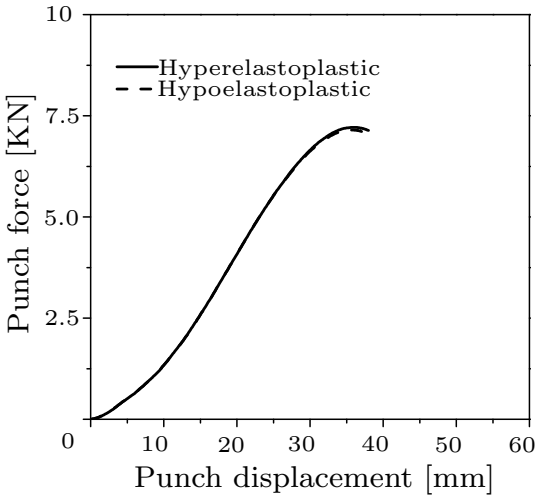

Figure 9.6: Comparison between the punch force-displacement diagram obtained from the hyper- and the hypoelastoplastic constitutive models for model parameters corresponding to the isotropic von Mises-type model, see Table 8.1(a).

means of forming limit diagrams.

9.3.1 Punch force-displacement response

This subsection presents the responses of the forming limit simulations in terms of the punch force-displacement. In order to demonstrate the capability of the constitutive model to capture the mechanical anisotropy of the materials, simulations based on the isotropic von Mises model are also performed. These simulations adopt the model parameter set presented in Table 8.2(a) together with the strain hardening and rate sensitivity parameters in Table 8.1. As shown in Fig. 9.7(b), the results corresponding to the isotropic model underestimate the force response for AZ31. This may be explained by the higher yield strength recorded in transverse than in rolling direction. A comparison for ZE10 indicates a better prediction. However, the maximum punch forces are still underestimated, see Fig. 9.7(a). Additionally and contrary to what has been concluded from AZ31, the higher yield strength observed in rolling direction of ZE10 does not lead to an overestimation of the force response as one might expect. One possible reason for this discrepancy is the exclusion of the distortional hardening during the forming simulation.

The force responses computed from the simulations utilizing the anisotropic material model show an improvement, see Fig. 9.8. However, the forces for higher deformation levels are either underestimated in the cases of geometry I and III or overestimated in cases of geometry V and VII. This is more pro-

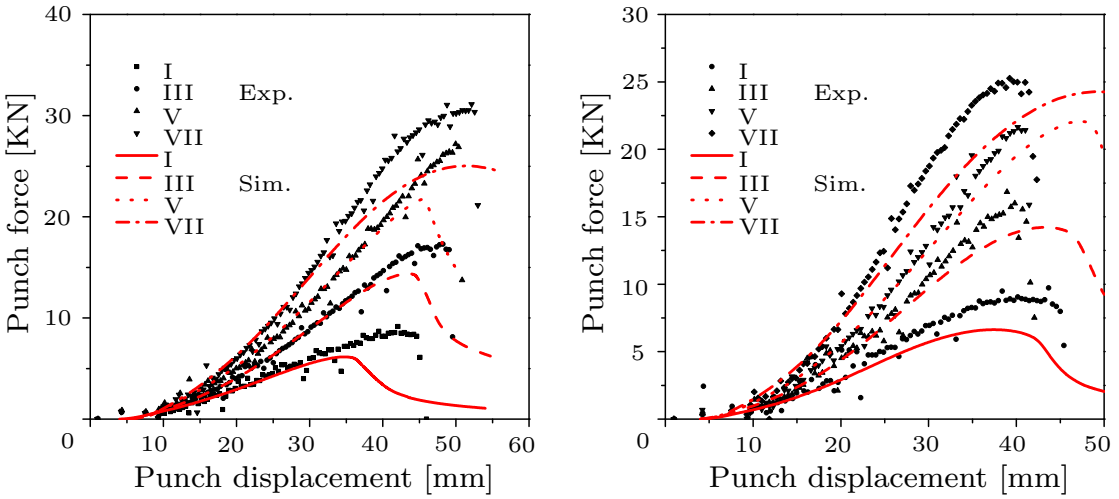

(a) ZE10 (b) AZ31

Figure 9.7: Comparison of punch force-displacement response of the forming limit simulation (fully isotropic von Mises model) and that observed in experiments.

nounced for AZ31 than for ZE10. At this point, it is assumed that the high level of extrapolated r-values shown in Fig. 8.7(b) may have contributed to this overestimation. Thus, improvement of the responses could possibly be achieved by an accurate measurement of the r-values at a high level of deformation.

To further investigate this effect on AZ31, simulations based on the re-calibrated constitutive model assuming constant r-values taken at strain levels of 0.03, 0.08 and 0.12 were performed, see Table 8.4 for the r-values and Appendix C Table C for the model parameters. The force-displacement curves for geometry I reveal that a change in the r-value has a relatively small effect on the force response. The simulation with a variable r-value results in a higher force response, see Fig. 9.9(a). In contrast to the geometry I, the figure shows considerable differences in the force responses for geometry VII.

Subsequently, simulations for work-piece geometries of I up to VII were conducted based on constant r-values taken at a strain level of 0.12. The resulting responses, presented in Fig. 9.9, show a reduced punch force and the peak values for geometries I and III are underestimated. The underestimated force response of geometry I in all cases could be related to the assumption of isothermal test conditions, while in reality a temperature drop up to 10^oC is observed during the experiment. Moreover, the absence of experimental data regarding the biaxial states of deformation (from biaxial tension tests) is also assumed to contribute to this effect.

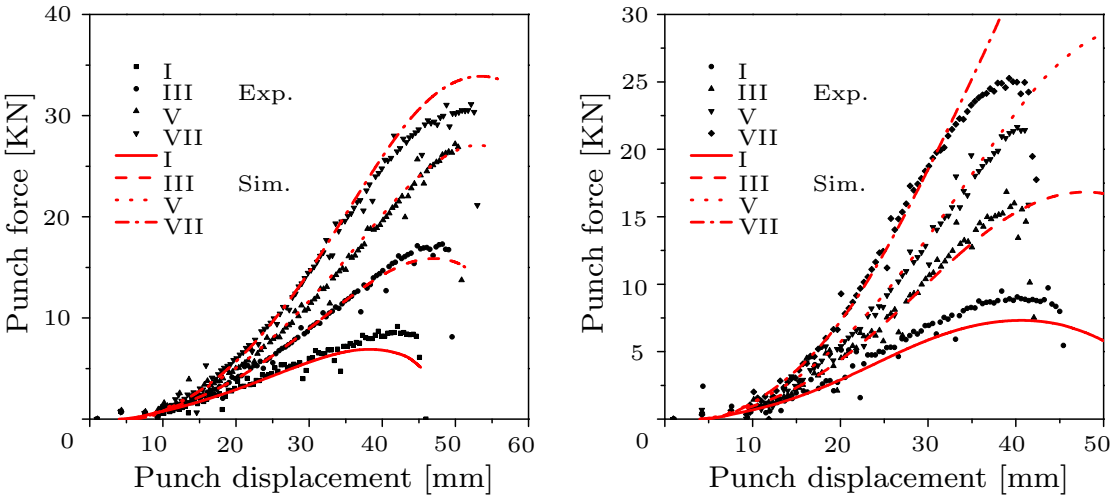

(a) ZE10 (b) AZ31

Figure 9.8: Comparison of punch force-displacement response of the forming limit simulation (novel anisotropic constitutive model including distortional hardening) and that observed in experiments.

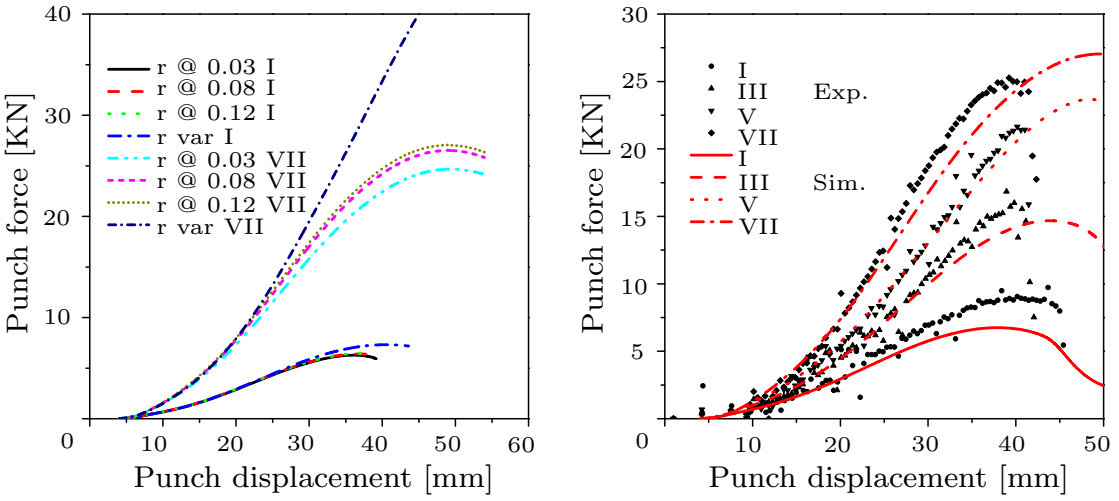

(a) r-value influence on punch force

(b) AZ31 punch force-displacement for a constant r-value taken at strain level of 0.12

Figure 9.9: Comparison of punch force-displacement response of the forming limit simulations for a constant r-value taken at a strain level of 0.12 and that observed in experiments for AZ31.

9.3.2 Strain path

In this subsection, the computed strain paths are analyzed. These strain paths are described by the history of the in-plane principal strains measured at the middle of the upper surface of the work-piece. As it is shown in Fig. 9.10, all work-piece geometries result in linear strain paths for higher deformation levels. Consistent with the experimental response, an offset in the minor principal strain into the positive domain of the forming limit diagram is also observed. This is particularly pronounced for geometries which should exhibit negative minor strain values, such as geometries I, II, III and IV. Such effects can be explained by the bending of the work-piece. According to Fig. 9.10(b), the strain paths for geometries I and VII of AZ31 are better captured compared to geometries III and V. The significant difference in the strain paths for geometries III and V for AZ31 can possibly be explained by the extrapolated r-values at high deformation.

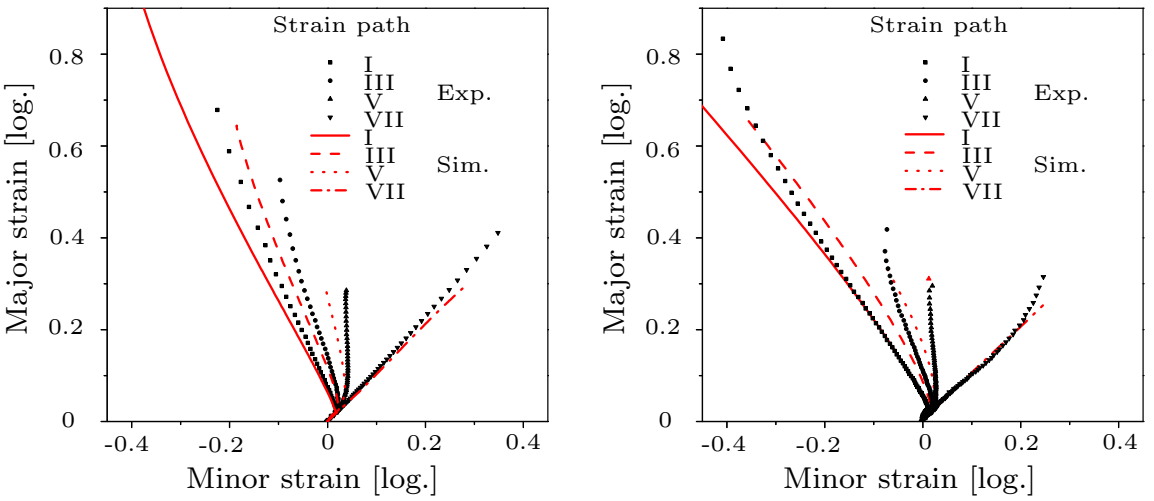

(a) ZE10 strain path

(b) AZ31 strain path

Figure 9.10: Comparison of experimentally measured and numerically predicted strain paths for ZE10 and AZ31.

Therefore, as employed for the force responses, the strain paths were recomputed based on constant r-values taken at strain levels of 0.03, 0.08 and 0.12. The simulation results plotted in Fig. 9.11(a) indicate that the strain paths obtained for work-piece geometry I shift to the left of the FLD domain with an increasing r-value. This effect is more pronounced in the case in which the r-value increases with increasing strain. For geometry VII, the change in r-value showed no significant effect on the strain path. Furthermore, the strain paths of the complete set of work-piece geometries for constant r-values taken at strain level of 0.12 are plotted in Fig. 9.11(b). In the figure, it is shown that the responses corresponding to geometries III and V of AZ31 are captured

well. By way of contrast, the predictions for geometry I are not as good.

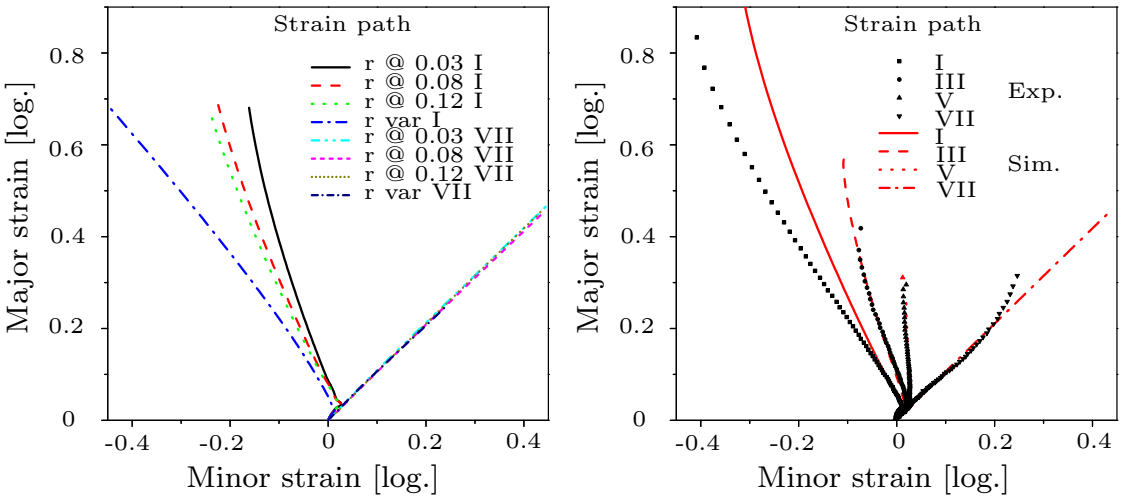

(a) r-value influence on strain path

(b) AZ31 strain path for constant r-value at a strain value of 0.12

Figure 9.11: Comparison of experimentally measured and numerically predicted strain paths for AZ31 for a constant r-value taken at a strain value of 0.12.

9.3.3 Forming limit diagram

The final subsection discusses the numerical prediction of the forming limit strains employing the MK localization criterion, see Chapter 5. Such predictions require a proper definition of a geometrical imperfection in the homogeneous work-piece. The magnitude of this imperfection is often calibrated based on a simple uniaxial tensile test. However, following the relatively early localization observed during the uniaxial tensile test, the reference limit strain data are taken from the equivalent forming test responses, specifically from geometry I. The required imperfection is obtained by performing simulations with different imperfection magnitudes. In general, a proper imperfection is chosen based on how close the predicted limit values are in comparison to the limit values of the selected forming test response (in this case those of geometry I). Subsequently, this same imperfection value shall be applied for the prediction of the remaining limit values (more specifically, those corresponding to geometries II-VII). In what follows, taking advantage of the available full set of experimental data, the effect of the different imperfection values on the limit values as obtained from the simulation is compared to all experimentally available limit values, see Fig. 9.12. From the figures and as expected it can be seen that the higher the imperfection the earlier the localization occurs.

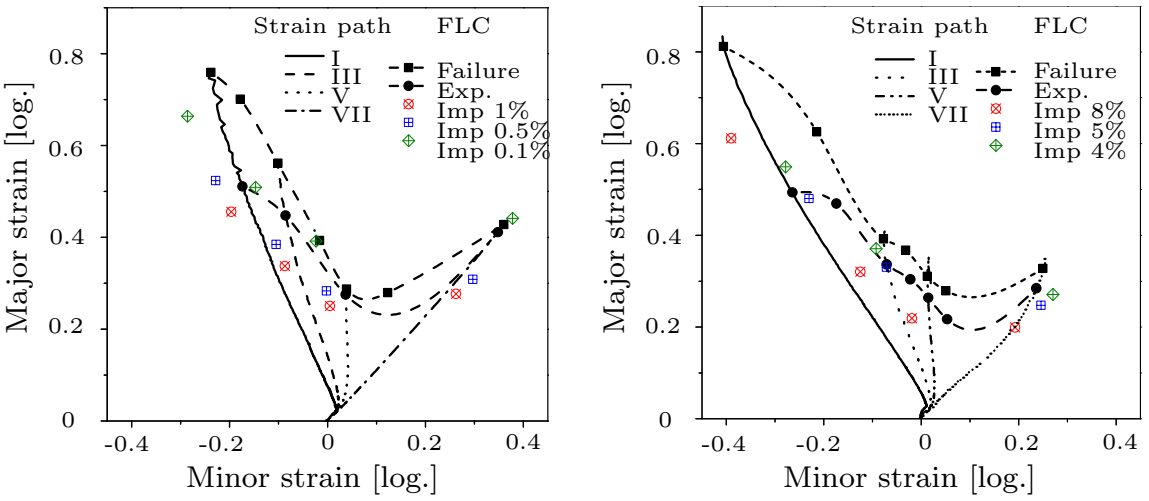

(a) ZE10 FLD (b) AZ31 FLD

Figure 9.12: Comparison of experimentally measured and numerically predicted limit strains for ZE10 and AZ31.

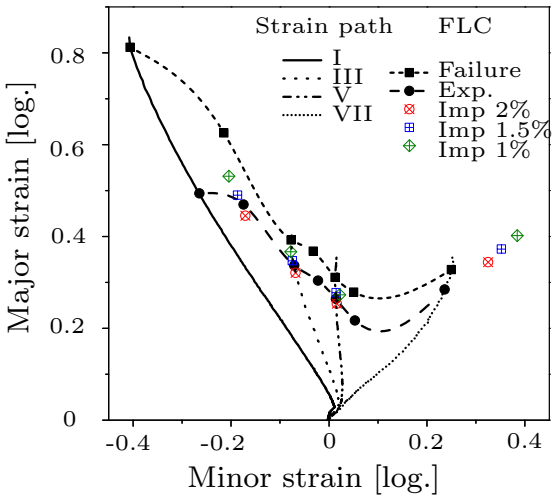

Figure 9.13: Comparison of experimentally measured and numerically predicted limit strains for AZ31 with a constant r-value taken at a strain level of 0.12.

The range of imperfection values used for the different model calibration was found to be different. For instance, in case of AZ31 with the model calibrated based on strain-dependent r-values, the required imperfection reaches as high as 10%. For the remaining cases, values between 1.5% to 0.1% lead to limit strains within the range of the reference values observed in the respective experiments, see Fig. 9.12. Improved forming limit values are established for AZ31 from simulations employing a constant r-value at a strain level of 0.12, see Fig. 9.13. This is again related to the extrapolation of the r-value for large

strain amplitudes. Computations for ZE10 based on a constant r-value have not been performed, since the observed r-values for ZE10 are close to one.

10 Summary and conclusion

In this thesis, a constitutive model for numerical analyses of sheet forming processes of magnesium alloys was developed, calibrated and implemented. This model has the capability to quantify and thus optimize process parameters that play an important role in sheet forming.

The development of the material model followed from the experimental investigations that helped understanding sheet forming processes. For that purpose, mechanical characterization through standardized uniaxial tensile tests with different test temperatures, material orientations and loading rates as well as formability tests were performed for AZ31 and ZE10.

From the resulting mechanical responses an increase in ductility for higher test temperatures could be confirmed. This effect is accompanied by the classical reduction in yield stress. Furthermore, the yield stresses increase for higher strain rates and they depend on the loading direction complying with the expected material anisotropy as observed in tensile tests for specimens having different orientations. This anisotropy is less pronounced in case of elevated temperatures. For analyzing the anisotropy in a more detailed manner, the r-values have been computed. From such analyses and in contrast to the aforementioned expected mechanical responses, it was observed that such values showed a strain-dependence. This dependency increases at elevated temperature. It is more pronounced for AZ31 due to its strong material anisotropy. It has also been observed that in case of AZ31 the r-values increased with increasing strain rate, while ZE10 showed a less pronounced but opposite effect.

The formability behavior of the magnesium alloys was analyzed through Nakazima-type forming tests at 200^oC. For the identification of the limit strains a new approach was advocated. Within this approach, the force-displacement and principal strain-displacement responses of the forming test are synchronized. By doing so, the artificial interpolation procedures required in the ISO standard for the identification of limit strains can be avoided.

The results of the forming tests revealed a sufficient formability at an elevated temperature of 200^oC. This was illustrated by a 0.5 limit strain in the uniaxial-like state and a 0.3 limit strain in the equi-biaxial state of deforma-

tion. Moreover and consistent with the large amount of nonuniform deformation recorded during the uniaxial tensile test, a large difference between the failure strain and the forming limit strain was observed in the negative domain of the FLD. The differences in the major and minor strains in the equi-biaxial loading condition for geometry VII as well as the recorded ratio of the strains for geometry I different from -2 reaffirmed the material anisotropy of AZ31 and ZE10.

The large number of process parameters involved in sheet forming make experimental investigations of the process very expensive. Therefore, numerical analyses are efficient and promising substitutes. For that purpose, a novel model was developed, calibrated and implemented within the finite element program ABAQUS® using an implicit integration scheme.

The novel constitutive model was developed based on the Cazacu & Barlat (2004) model to account for the complexity in the yielding behavior of magnesium alloys. In contrast to the Cazacu & Barlat (2004) model, the novel model is frame indifferent arising from the tensorial reformulation in terms of Mandel stresses. The evolution of the shape of the yield locus was also accommodated by expressing the model parameters as a function of the equivalent plastic strain. Furthermore, the constitutive model was recast into a thermodynamically consistent form by imposing a nonnegative dissipation. The Marciniak and Kuczynski localization criterion, which analyzes plastic instability triggered by geometrical imperfection, was also incorporated into the model for the prediction of sheet forming limits.

Finally, the calibrated model was employed in the numerical analyses of sheet forming processes. One of the primary objectives in these numerical analyses was the investigation of process parameters affecting the outcome of the Nakazima-type forming test such as friction and material anisotropy. On one hand, it was demonstrated that an increasing friction between the punch and the work-piece offsets the position of localization from the center of the work-piece. The added constraint due to the increase in friction was also accommodated by an increase in the force response. On the other hand, the change in the normal anisotropy was shown to result in a shift in the strain path mainly for work-piece geometries having negative minor strain. By way of contrast, the work-piece geometries having positive minor strain accommodate the change in the normal anisotropy only through their force response. For the sake of comparison, an isotropic von Mises was also used. From the respective numerical results it could clearly be seen that the novel anisotropic model leads to significantly better predictions. In summary, the novel model is very promising for getting further insight in sheet forming processes and it will be used in the future for optimizing forming processes.

A Tensorial algebra and differentiation

In this section, the tensor algebra and tensorial differentiation used within the present thesis are briefly introduced, see (Wu, 2005; Kintzel, 2007).

A.1 Tensorial products

A vector $\boldsymbol{x}$ can be described by scalar-valued quantities x_i along the base vectors $\mathbf{e}_i$ through the expression

$$\boldsymbol{x} = x_i \mathbf{e}_i.$$

Here, Einstein convention has been used. The classical cross product $\times$ of two vectors $\boldsymbol{x}$ and $\boldsymbol{v}$ is defined as

$$\boldsymbol{w} = w_k \, \mathbf{e}_k = x_i \, v_j \, \mathbf{e}_i \times \mathbf{e}_j,$$

with $\mathbf{e}_1 \times \mathbf{e}_2 = \mathbf{e}_3$, $\mathbf{e}_3 \times \mathbf{e}_1 = \mathbf{e}_2$, $\mathbf{e}_2 \times \mathbf{e}_1 = -\mathbf{e}_3$, $\mathbf{e}_3 \times \mathbf{e}_2 = -\mathbf{e}_1$, $\mathbf{e}_1 \times \mathbf{e}_3 = -\mathbf{e}_2$ and $\mathbf{e}_i \times \mathbf{e}_j = 0$ for $i = j$.

A second-order tensorial quantity $\mathbf{F}$ can be derived from the dyadic product $\otimes$ of vectors, i.e.,

$$\mathbf{F} = \mathrm{F}_{ij} \mathbf{e}_i \otimes \mathbf{e}_j,$$

with the scalar quantity F_{ij} along the base vectors $\mathbf{e}_i$ and $\mathbf{e}_j$, respectively. Again, Einstein convention has been used here. With this definition, the second-order identity tensor is defined as $\mathbf{I} = \mathbf{e}_i \otimes \mathbf{e}_j$ for $i = j$. Higher-order tensors such as the fourth-order tensor $\mathbb{C}$ can be written as

$$\mathbb{C} = \mathrm{C}_{ijkl} \mathbf{e}_i \otimes \mathbf{e}_j \otimes \mathbf{e}_k \otimes \mathbf{e}_l.$$

The dyadic product between two second-order tensors $\mathbf{A}$ and $\mathbf{B}$ take the form

$$\mathbf{A} \otimes \mathbf{B} = \mathrm{A}_{ij} \mathrm{B}_{kl} \mathbf{e}_i \otimes \mathbf{e}_j \otimes \mathbf{e}_k \otimes \mathbf{e}_l = \mathbb{C} = \mathrm{C}_{ijkl} \mathbf{e}_i \otimes \mathbf{e}_j \otimes \mathbf{e}_k \otimes \mathbf{e}_l.$$

In the present thesis, the two nonclassical dyadic products $\oplus$ and $\boxtimes$

$$\mathbf{A} \oplus \mathbf{B} = \mathrm{A}_{il} \mathrm{B}_{jk} \mathbf{e}_i \otimes \mathbf{e}_j \otimes \mathbf{e}_k \otimes \mathbf{e}_l = \mathbb{D} = \mathrm{D}_{ijkl} \mathbf{e}_i \otimes \mathbf{e}_j \otimes \mathbf{e}_k \otimes \mathbf{e}_l,$$

$$\mathbf{A} \boxtimes \mathbf{B} = \mathrm{A}_{ik} \mathrm{B}_{jl} \mathbf{e}_i \otimes \mathbf{e}_j \otimes \mathbf{e}_k \otimes \mathbf{e}_l = \mathbb{E} = \mathrm{E}_{ijkl} \mathbf{e}_i \otimes \mathbf{e}_j \otimes \mathbf{e}_k \otimes \mathbf{e}_l,$$

are also used.

A.2 Tensorial contractions

A.2.1 Conventional tensorial contractions

The simple contraction $(\cdot)$ is defined in standard manner. For instance, for the two second-order tensors $\mathbf{P}$ and $\mathbf{F}$ it reads

$$\mathbf{P} \cdot \mathbf{F} = \mathrm{P}_{ij}\mathrm{F}_{kl}(\mathbf{e}_j.\mathbf{e}_k)(\mathbf{e}_i \otimes \mathbf{e}_l) = \mathrm{P}_{ij}\mathrm{F}_{jl}\mathbf{e}_i \otimes \mathbf{e}_l = \mathbf{W}.$$

Similarly, the standard double contraction $(:)$ is introduced by

$$\mathbf{P} : \mathbf{F} = \mathrm{P}_{ij}\mathrm{F}_{kl}(\mathbf{e}_i.\mathbf{e}_k)(\mathbf{e}_j.\mathbf{e}_l) = \mathrm{P}_{ij}\mathrm{F}_{kl}\delta_{ik}\delta_{jl} = \mathrm{P}_{ij}\mathrm{F}_{ij} = w.$$

Finally, a quadruple contraction $(::)$ is defined as

$$\mathbb{C} :: \mathbb{D} = \mathrm{C}_{ijkl}\mathrm{D}_{mnop}(\mathbf{e}_i.\mathbf{e}_m)(\mathbf{e}_j.\mathbf{e}_n)(\mathbf{e}_k.\mathbf{e}_o)(\mathbf{e}_l.\mathbf{e}_p) = \mathrm{C}_{ijkl}\mathrm{D}_{ijkl}.$$

A.2.2 Non-conventional tensorial contractions

In addition to the standard contractions explained before, the two nonconventional contractions $(\bullet\circ)$ and $(\circ\bullet)$

$$\mathbb{C}\bullet\circ\mathbf{F} = \mathrm{C}_{ijkl}\mathrm{F}_{mn}(\mathbf{e}_j.\mathbf{e}_m)(\mathbf{e}_k.\mathbf{e}_n)(\mathbf{e}_i \otimes \mathbf{e}_l) = \mathrm{C}_{ijkl}\mathrm{F}_{jk}\mathbf{e}_i \otimes \mathbf{e}_l,$$

$$\mathbb{C}\circ\bullet\mathbf{F} = \mathrm{C}_{ijkl}\mathrm{F}_{mn}(\mathbf{e}_i.\mathbf{e}_m)(\mathbf{e}_l.\mathbf{e}_n)(\mathbf{e}_j \otimes \mathbf{e}_k) = \mathrm{C}_{ijkl}\mathrm{F}_{il}\mathbf{e}_j \otimes \mathbf{e}_k.$$

are also considered in the present thesis. The consistent generalization for two fourth-order tensors $\mathbb{C}$ and $\mathbb{D}$ is given by

$$\begin{aligned}
\mathbb{C}\bullet\circ\mathbb{D} &= \mathrm{C}_{ijkl}\mathrm{D}_{mnop}(\mathbf{e}_j.\mathbf{e}_m)(\mathbf{e}_k.\mathbf{e}_p)(\mathbf{e}_i \otimes \mathbf{e}_n \otimes \mathbf{e}_o \otimes \mathbf{e}_l) \\
&= \mathrm{C}_{ijkl}\mathrm{D}_{jnok}\mathbf{e}_i \otimes \mathbf{e}_n \otimes \mathbf{e}_o \otimes \mathbf{e}_l, \\
\mathbb{C}\circ\bullet\mathbb{D} &= \mathrm{C}_{ijkl}\mathrm{D}_{mnop}(\mathbf{e}_i.\mathbf{e}_n)(\mathbf{e}_l.\mathbf{e}_o)(\mathbf{e}_m \otimes \mathbf{e}_j \otimes \mathbf{e}_k \otimes \mathbf{e}_p) \\
&= \mathrm{C}_{ijkl}\mathrm{D}_{milp}\mathbf{e}_m \otimes \mathbf{e}_j \otimes \mathbf{e}_k \otimes \mathbf{e}_p.
\end{aligned}$$

A.3 Tensorial transposition

While for second-order tensors, the definition of the transposed is uniquely defined by

$$\mathbf{F}^{\mathrm{T}} = (\mathrm{F}_{ij}\mathbf{e}_i \otimes \mathbf{e}_j)^{\mathrm{T}} = \mathrm{F}_{ij}\mathbf{e}_j \otimes \mathbf{e}_i = \mathrm{F}_{ji}\mathbf{e}_i \otimes \mathbf{e}_j,$$

different definitions are possible for fourth-order tensors. In the present thesis, the following three notations $()^{\mathrm{T}}$, $()^{\mathrm{L}}$ and $()^{\mathrm{R}}$ are used:

$$\begin{aligned}
\mathbb{C}^{\mathrm{T}} &= (\mathrm{C}_{ijkl}\mathbf{e}_i \otimes \mathbf{e}_j \otimes \mathbf{e}_k \otimes \mathbf{e}_l)^{\mathrm{T}} = \mathrm{C}_{ijkl}\mathbf{e}_j \otimes \mathbf{e}_i \otimes \mathbf{e}_l \otimes \mathbf{e}_k \\
&= \mathrm{C}_{jilk}\mathbf{e}_i \otimes \mathbf{e}_j \otimes \mathbf{e}_k \otimes \mathbf{e}_l, \\
\mathbb{C}^{\mathrm{L}} &= (\mathrm{C}_{ijkl}\mathbf{e}_i \otimes \mathbf{e}_j \otimes \mathbf{e}_k \otimes \mathbf{e}_l)^{\mathrm{L}} = \mathrm{C}_{ijkl}\mathbf{e}_i \otimes \mathbf{e}_k \otimes \mathbf{e}_l \otimes \mathbf{e}_j \\
&= \mathrm{C}_{iklj}\mathbf{e}_j \otimes \mathbf{e}_i \otimes \mathbf{e}_l \otimes \mathbf{e}_k, \\
\mathbb{C}^{\mathrm{R}} &= (\mathrm{C}_{ijkl}\mathbf{e}_i \otimes \mathbf{e}_j \otimes \mathbf{e}_k \otimes \mathbf{e}_l)^{\mathrm{R}} = \mathrm{C}_{ijkl}\mathbf{e}_i \otimes \mathbf{e}_l \otimes \mathbf{e}_j \otimes \mathbf{e}_k \\
&= \mathrm{C}_{iljk}\mathbf{e}_i \otimes \mathbf{e}_j \otimes \mathbf{e}_k \otimes \mathbf{e}_l.
\end{aligned}$$

A.4 Tensorial differentiation

The gradient grad(•) and div(•) operations follow the standard relations

$$\mathrm{grad}(\boldsymbol{w}) = \frac{\partial w_i}{\partial x_j}\, \boldsymbol{e}_i \cdot \boldsymbol{e}_j, \qquad \mathrm{div}(\boldsymbol{\sigma}) = \frac{\partial \sigma_{ij}}{\partial x_j}\, \boldsymbol{e}_i.$$

The partial derivative of a scalar function $f(\mathbf{\Sigma})$ with respect to the second-order tensor $\mathbf{\Sigma}$ is written as

$$\partial_{\mathbf{\Sigma}} f = \partial_{\Sigma_{ij}} f \mathbf{e}_i \otimes \mathbf{e}_j = \mathrm{N}_{ij}\mathbf{e}_i \otimes \mathbf{e}_j = \mathbf{N},$$

while the derivative of a tensor-valued function $\mathbf{N}(\mathbf{\Sigma})$ with respect to the second-order tensor $\mathbf{\Sigma}$ is given by

$$\partial_{\mathbf{\Sigma}} \mathbf{N} = \partial_{\Sigma_{kl}} \mathrm{N}_{ij}\mathbf{e}_i \otimes \mathbf{e}_k \otimes \mathbf{e}_l \otimes \mathbf{e}_j = \mathrm{D}_{iklj}\mathbf{e}_i \otimes \mathbf{e}_j \otimes \mathbf{e}_k \otimes \mathbf{e}_l = \mathbb{D}.$$

Consequently,

$$\begin{aligned}
\partial_{\mathbf{N}} \mathbf{N} &= \partial_{\mathbf{N}^{\mathrm{T}}} \mathbf{N}^{\mathrm{T}} = \partial_{\mathrm{N}_{kl}} \mathrm{N}_{ij}\mathbf{e}_i \otimes \mathbf{e}_k \otimes \mathbf{e}_l \otimes \mathbf{e}_j = \mathbf{I} \otimes \mathbf{I}, \\
\partial_{\mathbf{N}^{\mathrm{T}}} \mathbf{N} &= \partial_{\mathbf{N}} \mathbf{N}^{\mathrm{T}} = \partial_{\mathrm{N}_{kl}} \mathrm{N}_{ij}\mathbf{e}_i \otimes \mathbf{e}_l \otimes \mathbf{e}_k \otimes \mathbf{e}_j = \mathbf{I} \boxtimes \mathbf{I}, \\
\partial_{\mathbf{N}^{-1}} \mathbf{N} &= -(\mathbf{N} \otimes \mathbf{N}), \qquad \partial_{\mathbf{N}} \mathbf{N}^{-1} = -(\mathbf{N}^{-1} \otimes \mathbf{N}^{-1}).
\end{aligned}$$

Furthermore, with the newly introduced tensor products, the product rule (depending on the order of the involved tensors) can be written as

$$\partial_{\mathbf{\Sigma}}(f(\mathbf{\Sigma})\mathbf{N}) = \partial_{\Sigma_{kl}}(f(\mathbf{\Sigma})\mathrm{N}_{ij})\mathbf{e}_i \otimes \mathbf{e}_k \otimes \mathbf{e}_l \otimes \mathbf{e}_j = \mathbf{N} \oplus \partial_{\mathbf{\Sigma}} f + f\partial_{\mathbf{\Sigma}} \mathbf{N},$$

$$\begin{aligned}
\partial_{\mathbf{F}}(\mathbf{\Sigma} \cdot \mathbf{N}) &= \partial_{\Sigma_{mn}}(\Sigma_{ij}\mathrm{N}_{kl})(\mathbf{e}_j \cdot \mathbf{e}_k)(\mathbf{e}_i \otimes \mathbf{e}_m \otimes \mathbf{e}_n \otimes \mathbf{e}_l) \\
&= \partial_{\mathbf{F}} \mathbf{\Sigma} \cdot \mathbf{N} + \mathbf{\Sigma} \cdot \partial_{\mathbf{F}} \mathbf{N},
\end{aligned}$$

$$\begin{aligned}\partial_{\mathbf{F}}(\boldsymbol{\Sigma}\colon \mathbf{N}) &= \partial_{\Sigma_{mn}}(\Sigma_{ij}\mathrm{N}_{kl})(\mathbf{e}_i\cdot\mathbf{e}_k)(\mathbf{e}_j\cdot\mathbf{e}_l)(\mathbf{e}_m\otimes\mathbf{e}_n)\\ &= \partial_{\mathbf{F}}\boldsymbol{\Sigma}\circ\bullet\mathbf{N}+\boldsymbol{\Sigma}\bullet\circ\partial_{\mathbf{F}}\mathbf{N}.\end{aligned}$$

For further details the interested reader is referred to the works of Kintzel (2007); Kintzel & Basar (2006); Wu (2005).

B Derivatives necessary for the numerical implementation

This appendix presents a detailed derivation of the derivatives necessary for the numerical implementation of the constitutive model discussed in chapter 4.

B.1 First-order derivatives of the yield function

By combining

$$\partial_{\boldsymbol{\Sigma}} f = \partial_{\mathrm{J}_2^{\circ}} f \; \partial_{\boldsymbol{\Sigma}} \mathrm{J}_2^{\circ} - \partial_{\boldsymbol{\Sigma}} \mathrm{J}_3^{\circ}$$

with

$$\begin{aligned} \partial_{\mathrm{J}_2^{\circ}} f &= 3/2 \; \mathrm{J}_2^{\circ 1/2} \\ \partial_{\boldsymbol{\Sigma}} \mathrm{J}_2^{\circ} &= \mathbb{H}_1^{\mathrm{L}} \circ \bullet \overline{\boldsymbol{\Sigma}}_1 \\ \partial_{\boldsymbol{\Sigma}} \mathrm{J}_3^{\circ} &= \mathrm{J}_3^{\circ} \; \overline{\boldsymbol{\Sigma}}_2^{-\mathrm{T}} \bullet \circ \mathbb{H}_2^{\mathrm{L}}, \end{aligned}$$

the derivative of the yield function with respect to the Mandel stresses can be computed.

Similarly, the partial derivative of the yield function with respect to the flow direction $\mathbf{N}$ is derived as

$$\partial_{\mathbf{N}} f = \partial_{\mathrm{J}_2} f \; \partial_{\mathbf{N}} \mathrm{J}_2^{\circ} - \partial_{\mathbf{N}} \mathrm{J}_3^{\circ}$$

with

$$\begin{aligned} \partial_{\mathbf{N}} \mathrm{J}_2^{\circ} &= \partial_{\mathbf{N}} \overline{\boldsymbol{\Sigma}}_1 \circ \bullet \overline{\boldsymbol{\Sigma}}_1 \\ \partial_{\mathbf{N}} \mathrm{J}_3^{\circ} &= \mathrm{J}_3^{\circ} \; \overline{\boldsymbol{\Sigma}}_2^{-\mathrm{T}} \bullet \circ \partial_{\mathbf{N}} \overline{\boldsymbol{\Sigma}}_2 \\ \partial_{\mathbf{N}} \mathrm{h} &= \partial_{\mathbf{N}} \mathrm{J}_{2_{\mathrm{o}}}^{\circ} - \partial_{\mathbf{N}} \mathrm{J}_{3_{\mathrm{o}}}^{\circ}, \end{aligned}$$

where,

$$\begin{aligned} \partial_{\mathbf{N}} \mathrm{J}_{2_{\mathrm{o}}}^{\circ} &= \partial_{\mathbf{N}} \overline{\boldsymbol{\Sigma}}_{1_{\mathrm{o}}} \circ \bullet \overline{\boldsymbol{\Sigma}}_{1_{\mathrm{o}}} \\ \partial_{\mathbf{N}} \mathrm{J}_{3_{\mathrm{o}}}^{\circ} &= \mathrm{J}_{3_{\mathrm{o}}}^{\circ} \; \overline{\boldsymbol{\Sigma}}_{2_{\mathrm{o}}}^{-\mathrm{T}} \bullet \circ \partial_{\mathbf{N}} \overline{\boldsymbol{\Sigma}}_{2_{\mathrm{o}}}. \end{aligned}$$

The partial derivative of the yield function with respect to the plastic multiplier takes the form

$$\partial_{\Delta\lambda} f = \partial_{\mathrm{J}_2} f \; \partial_{\Delta\lambda} \mathrm{J}_2^{\mathrm{o}} - \partial_{\Delta\lambda} \mathrm{J}_3^{\mathrm{o}} - \partial_{\Delta\lambda} \mathrm{h}$$

with

$$\begin{aligned}
\partial_{\Delta\lambda} \mathrm{J}_2^{\mathrm{o}} &= 1/2 \; \left(\partial_{\Delta\lambda} \overline{\boldsymbol{\Sigma}}_1 : \overline{\boldsymbol{\Sigma}}_1 + \overline{\boldsymbol{\Sigma}}_1 : \partial_{\Delta\lambda} \overline{\boldsymbol{\Sigma}}_1 \right) \\
\partial_{\Delta\lambda} \mathrm{J}_3^{\mathrm{o}} &= \mathrm{J}_3^{\mathrm{o}} \; \overline{\boldsymbol{\Sigma}}_2^{-\mathrm{T}} : \partial_{\Delta\lambda} \overline{\boldsymbol{\Sigma}}_2 \\
\partial_{\Delta\lambda} \mathrm{h} &= \partial_{\mathrm{J}_{2_{\mathrm{o}}}^{\mathrm{o}}} \mathrm{h} \; \partial_{\Delta\lambda} \mathrm{J}_{2_{\mathrm{o}}}^{\mathrm{o}} - \partial_{\Delta\lambda} \mathrm{J}_{3_{\mathrm{o}}}^{\mathrm{o}},
\end{aligned}$$

where,

$$\begin{aligned}
\partial_{\mathrm{J}_{2_{\mathrm{o}}}^{\mathrm{o}}} \mathrm{h} &= 3/2 \mathrm{J}_{2_{\mathrm{o}}}^{\mathrm{o}}{}^{1/2} \\
\partial_{\Delta\lambda} \mathrm{J}_{2_{\mathrm{o}}}^{\mathrm{o}} &= 1/2 \; \left(\partial_{\Delta\lambda} \overline{\boldsymbol{\Sigma}}_{1_{\mathrm{o}}} : \overline{\boldsymbol{\Sigma}}_{1_{\mathrm{o}}} + \overline{\boldsymbol{\Sigma}}_{1_{\mathrm{o}}} : \partial_{\Delta\lambda} \overline{\boldsymbol{\Sigma}}_{1_{\mathrm{o}}} \right) \\
\partial_{\Delta\lambda} \mathrm{J}_{3_{\mathrm{o}}}^{\mathrm{o}} &= \mathrm{J}_{3_{\mathrm{o}}}^{\mathrm{o}} \; \overline{\boldsymbol{\Sigma}}_{2_{\mathrm{o}}}{}^{-\mathrm{T}} : \partial_{\Delta\lambda} \overline{\boldsymbol{\Sigma}}_{2_{\mathrm{o}}}.
\end{aligned}$$

B.2 Derivatives of the stress tensor and the distortional hardening tensors $\mathbb{H}_i$

The partial derivatives of the stress tensor with respect to the flow direction $\mathbf{N}$ is computed as

$$\begin{aligned}
\partial_{\mathbf{N}} \overline{\boldsymbol{\Sigma}}_i &= \left(\partial_{\mathbf{N}} \mathbb{H}_i^{\mathrm{L}^{\mathrm{T}}} \circ\bullet \boldsymbol{\Sigma} \right) + \left(\mathbb{H}_i^{\mathrm{L}} \bullet\circ \partial_{\mathbf{N}} \boldsymbol{\Sigma} \right) \\
\partial_{\mathbf{N}} \overline{\boldsymbol{\Sigma}}_{i_{\mathrm{o}}} &= \left(\partial_{\mathbf{N}} \mathbb{H}_i^{\mathrm{L}^{\mathrm{T}}} \circ\bullet \boldsymbol{\Sigma}_{\mathrm{o}} \right) + \left(\mathbb{H}_i^{\mathrm{L}} \bullet\circ \partial_{\mathbf{N}} \boldsymbol{\Sigma}_{\mathrm{o}} \right),
\end{aligned}$$

where,

$$\begin{aligned}
\partial_{\mathbf{N}} \mathbb{H}_i^{\mathrm{L}^{\mathrm{T}}} &= \partial_{\bar{\varepsilon}^{\mathrm{pl}}} \mathbb{H}_i^{\mathrm{L}^{\mathrm{T}}} \; \oplus \; \partial_{\mathbf{N}} \bar{\varepsilon}^{\mathrm{pl}} \\
\partial_{\mathbf{N}} \boldsymbol{\Sigma} &= \partial_{\mathbf{F}^{\mathrm{pl}}} \boldsymbol{\Sigma} \bullet\circ \partial_{\mathbf{N}} \mathbf{F}^{\mathrm{pl}} \\
\partial_{\mathbf{N}} \boldsymbol{\Sigma}_{\mathrm{o}} &= \partial_{\bar{\varepsilon}^{\mathrm{pl}}} \boldsymbol{\Sigma}_{\mathrm{o}} \; \oplus \; \partial_{\mathbf{N}} \bar{\varepsilon}^{\mathrm{pl}},
\end{aligned}$$

while the derivative with respect to the plastic multiplier reads

$$\begin{aligned}
\partial_{\Delta\lambda} \overline{\boldsymbol{\Sigma}}_i &= \left(\partial_{\Delta\lambda} \mathbb{H}_i : \boldsymbol{\Sigma} \right) + \left(\mathbb{H}_i : \partial_{\Delta\lambda} \boldsymbol{\Sigma} \right) \\
\partial_{\Delta\lambda} \overline{\boldsymbol{\Sigma}}_{i_{\mathrm{o}}} &= \left(\partial_{\Delta\lambda} \mathbb{H}_i : \boldsymbol{\Sigma}_{\mathrm{o}} \right) + \left(\mathbb{H}_i : \partial_{\Delta\lambda} \boldsymbol{\Sigma}_{\mathrm{o}} \right),
\end{aligned}$$

where,

$$\begin{aligned}
\partial_{\Delta\lambda} \boldsymbol{\Sigma} &= \partial_{\mathbf{F}^{\mathrm{pl}}} \boldsymbol{\Sigma} \bullet\circ \partial_{\Delta\lambda} \mathbf{F}^{\mathrm{pl}} \\
\partial_{\Delta\lambda} \boldsymbol{\Sigma}_{\mathrm{o}} &= \partial_{\bar{\varepsilon}^{\mathrm{pl}}} \boldsymbol{\Sigma}_{\mathrm{o}} \; \partial_{\Delta\lambda} \bar{\varepsilon}^{\mathrm{pl}} \\
\partial_{\Delta\lambda} \mathbb{H}_i &= \partial_{\bar{\varepsilon}^{\mathrm{pl}}} \mathbb{H}_i \; \partial_{\Delta\lambda} \bar{\varepsilon}^{\mathrm{pl}}.
\end{aligned}$$

Assuming a neo-Hooke model characterized by the Mandel stresses

$$\boldsymbol{\Sigma} = 2\, \boldsymbol{C}^{\mathrm{e}} \cdot \partial_{\mathbf{C}^{\mathrm{e}}} \Psi = \lambda \frac{\mathrm{J}^2 - 1}{2}\, \mathbf{I} + \mu\, (\boldsymbol{C}^{\mathrm{e}} - \mathbf{I})\,,$$

the derivatives of the stresses with respect to the elastic and the plastic part of the deformation gradient are given by

$$\begin{aligned}
\partial_{\mathbf{F}^{\mathrm{pl}}} \boldsymbol{\Sigma} &= \partial_{\mathbf{F}^{\mathrm{e}}} \boldsymbol{\Sigma} \bullet\circ \partial_{\mathbf{F}^{\mathrm{pl}}} \mathbf{F}^{\mathrm{e}} \\
\partial_{\mathbf{F}^{\mathrm{pl}}} \mathbf{F}^{\mathrm{e}} &= -\,\mathbf{F}\, \left(\mathbf{F}^{\mathrm{pl}\,-1} \otimes \mathbf{F}^{\mathrm{pl}\,-1} \right) \\
\partial_{\mathbf{F}^{\mathrm{e}}} \boldsymbol{\Sigma} &= \lambda\, \mathrm{J}^2 \Big(\mathbf{I} \,\oplus\, \mathbf{F}^{\mathrm{e}\,-\mathrm{T}} \Big) + \mu\, \Big[(\mathbf{I} \boxtimes \mathbf{F}^{\mathrm{e}}) + \Big(\mathbf{F}^{\mathrm{e}\,\mathrm{T}} \otimes \mathbf{I} \Big) \Big]\,.
\end{aligned}$$

Finally, the closed-form solutions for the derivatives of the plastic part of the deformation gradient $\mathbf{F}^{\mathrm{pl}}$ and the equivalent plastic strain $\overline{\varepsilon}^{\mathrm{pl}}$ yield

$$\mathbf{F}^{\mathrm{p}}_{t+\Delta t} := \exp(\Delta\lambda\, \mathbf{N}) \cdot \mathbf{F}^{\mathrm{p}}_{t}$$

$$\begin{aligned}
\partial_{\mathbf{N}} \mathbf{F}^{\mathrm{pl}}_{t+\Delta t} &= \Delta\lambda\, \mathrm{D} \exp(\Delta\lambda\, \mathbf{N}) \cdot \mathbf{F}^{\mathrm{pl}}_{t} \\
\partial_{\Delta\lambda} \mathbf{F}^{\mathrm{pl}}_{t+\Delta t} &= [\mathrm{D} \exp(\Delta\lambda\, \mathbf{N}) \bullet\circ \mathbf{N}] \cdot \mathbf{F}^{\mathrm{pl}}_{t}
\end{aligned}$$

$$\dot{\overline{\varepsilon}}^{\mathrm{pl}} = \dot{\lambda}\, \|\mathbf{N}\|, \qquad \overline{\varepsilon}^{\mathrm{pl}}{}_{t+\Delta t} = \overline{\varepsilon}^{\mathrm{pl}}{}_{t} + \Delta\overline{\varepsilon}^{\mathrm{pl}}$$

$$\partial_{\mathbf{N}} \overline{\varepsilon}^{\mathrm{pl}} = \Delta\lambda\, \frac{\mathbf{N}}{\|\mathbf{N}\|}, \qquad \partial_{\Delta\lambda} \overline{\varepsilon}^{\mathrm{pl}} = \|\mathbf{N}\|.$$

B.3 Second-order derivatives of the yield function

The second-order partial derivatives of the yield function with respect to the stress tensor and the flow direction $\mathbf{N}$ are given by

$$\frac{\partial^2 f}{\partial \boldsymbol{\Sigma} \partial \mathbf{N}} = \left(\frac{\partial \mathrm{J}^{\mathrm{o}}_2}{\partial \boldsymbol{\Sigma}} \,\oplus\, \frac{\partial^2 f}{\partial \mathrm{J}^{\mathrm{o}}_2 \partial \mathbf{N}} \right) + \partial_{\mathrm{J}^{\mathrm{o}}_2} f\, \frac{\partial^2 \mathrm{J}^{\mathrm{o}}_2}{\partial \boldsymbol{\Sigma} \partial \mathbf{N}} - \frac{\partial^2 \mathrm{J}^{\mathrm{o}}_3}{\partial \boldsymbol{\Sigma} \partial \mathbf{N}},$$

where,

$$\begin{aligned}
\frac{\partial^2 f}{\partial \mathrm{J}^{\mathrm{o}}_2 \partial \mathbf{N}} &= 3/4 \mathrm{J}^{\mathrm{o}\,-1/2}_2\, \partial_{\mathbf{N}} \mathrm{J}^{\mathrm{o}}_2 \\
\frac{\partial^2 \mathrm{J}^{\mathrm{o}}_2}{\partial \boldsymbol{\Sigma} \partial \mathbf{N}} &= \Big(\partial_{\mathbf{N}} \mathbb{H}^{\mathrm{L}}_1 \bullet\circ \overline{\boldsymbol{\Sigma}}_1 \Big) + \Big(\mathbb{H}^{\mathrm{L}\,\mathrm{T}}_1 \bullet\circ \partial_{\mathbf{N}} \overline{\boldsymbol{\Sigma}}_1 \Big) \\
\frac{\partial^2 \mathrm{J}^{\mathrm{o}}_3}{\partial \boldsymbol{\Sigma} \partial \mathbf{N}} &= \Big[\Big(\overline{\boldsymbol{\Sigma}}^{-\mathrm{T}}_2 \bullet\circ \mathbb{H}^{\mathrm{L}}_2 \Big) \,\oplus\, \partial_{\mathbf{N}} \mathrm{J}^{\mathrm{o}}_3 \Big] + \mathrm{J}^{\mathrm{o}}_3\, \partial_{\mathbf{N}} \Big(\overline{\boldsymbol{\Sigma}}^{-\mathrm{T}}_2 \bullet\circ \mathbb{H}^{\mathrm{L}}_2 \Big)
\end{aligned}$$

$$\begin{aligned}\partial_{\mathbf{N}}\left(\overline{\mathbf{\Sigma}}_2^{-\mathrm{T}} \bullet\circ \mathbb{H}_2^{\mathrm{L}}\right) &= \left(\partial_{\mathbf{N}}\overline{\mathbf{\Sigma}}_2^{-\mathrm{T}} \circ\bullet \mathbb{H}_2^{\mathrm{L}^{\mathrm{T}}}\right) + \left(\overline{\mathbf{\Sigma}}_2^{-\mathrm{T}} \bullet\circ \partial_{\mathbf{N}}\mathbb{H}_2^{\mathrm{L}}\right)\\ \partial_{\mathbf{N}}\overline{\mathbf{\Sigma}}_2^{-\mathrm{T}} &= -\left(\overline{\mathbf{\Sigma}}_2^{-\mathrm{T}} \boxtimes \overline{\mathbf{\Sigma}}_2^{-\mathrm{T}}\right) \bullet\circ \partial_{\mathbf{N}}\overline{\mathbf{\Sigma}}_2.\end{aligned}$$

The second-order partial derivative of the yield function with respect to the stress tensor reads

$$\frac{\partial^2 f}{\partial\mathbf{\Sigma}\partial\mathbf{\Sigma}} = \left(\frac{\partial \mathrm{J}_2^{\mathrm{o}}}{\partial\mathbf{\Sigma}} \oplus \frac{\partial^2 f}{\partial \mathrm{J}_2^{\mathrm{o}}\partial\mathbf{\Sigma}}\right) + \partial_{\mathrm{J}_2^{\mathrm{o}}} f \, \frac{\partial^2 \mathrm{J}_2^{\mathrm{o}}}{\partial\mathbf{\Sigma}\partial\mathbf{\Sigma}} - \frac{\partial^2 \mathrm{J}_3^{\mathrm{o}}}{\partial\mathbf{\Sigma}\partial\mathbf{\Sigma}},$$

where,

$$\begin{aligned}\frac{\partial^2 f}{\partial \mathrm{J}_2^{\mathrm{o}}\partial\mathbf{\Sigma}} &= 3/4\mathrm{J}_2^{\mathrm{o}\,-1/2}\, \partial_{\mathbf{\Sigma}}\mathrm{J}_2^{\mathrm{o}}\\ \frac{\partial^2 \mathrm{J}_2^{\mathrm{o}}}{\partial\mathbf{\Sigma}\partial\mathbf{\Sigma}} &= \mathbb{H}_1^{\mathrm{L}^{\mathrm{T}}} \bullet\circ \partial_{\mathbf{\Sigma}}\overline{\mathbf{\Sigma}}_1\\ \frac{\partial^2 \mathrm{J}_3^{\mathrm{o}}}{\partial\mathbf{\Sigma}\partial\mathbf{\Sigma}} &= \left[\left(\overline{\mathbf{\Sigma}}_2^{-\mathrm{T}} \bullet\circ \mathbb{H}_2^{\mathrm{L}}\right) \oplus \partial_{\mathbf{\Sigma}}\mathrm{J}_3^{\mathrm{o}}\right] + \mathrm{J}_3^{\mathrm{o}}\, \partial_{\mathbf{\Sigma}}\left(\overline{\mathbf{\Sigma}}_2^{-\mathrm{T}} \bullet\circ \mathbb{H}_2^{\mathrm{L}}\right)\end{aligned}$$

$$\begin{aligned}\partial_{\mathbf{\Sigma}}\left(\overline{\mathbf{\Sigma}}_2^{-\mathrm{T}} \bullet\circ \mathbb{H}_2^{\mathrm{L}}\right) &= \partial_{\mathbf{\Sigma}}\overline{\mathbf{\Sigma}}_2^{-\mathrm{T}} \circ\bullet \mathbb{H}_2^{\mathrm{L}^{\mathrm{T}}}\\ \partial_{\mathbf{\Sigma}}\overline{\mathbf{\Sigma}}_2^{-\mathrm{T}} &= -\left(\overline{\mathbf{\Sigma}}_2^{-\mathrm{T}} \boxtimes \overline{\mathbf{\Sigma}}_2^{-\mathrm{T}}\right) \bullet\circ \partial_{\mathbf{\Sigma}}\overline{\mathbf{\Sigma}}_2.\end{aligned}$$

Finally, a partial derivative of the yield function with respect to the stress tensor and the plastic multiplier results in

$$\frac{\partial^2 f}{\partial\mathbf{\Sigma}\partial\Delta\lambda} = \frac{\partial^2 f}{\partial \mathrm{J}_2^{\mathrm{o}}\partial\Delta\lambda}\, \frac{\partial \mathrm{J}_2^{\mathrm{o}}}{\partial\mathbf{\Sigma}} + \partial_{\mathrm{J}_2^{\mathrm{o}}} f \, \frac{\partial^2 \mathrm{J}_2^{\mathrm{o}}}{\partial\mathbf{\Sigma}\partial\Delta\lambda} - \frac{\partial^2 \mathrm{J}_3^{\mathrm{o}}}{\partial\mathbf{\Sigma}\partial\Delta\lambda},$$

where,

$$\begin{aligned}\frac{\partial^2 f}{\partial \mathrm{J}_2^{\mathrm{o}}\partial\Delta\lambda} &= 3/4\mathrm{J}_2^{\mathrm{o}\,-1/2}\, \partial_{\Delta\lambda}\mathrm{J}_2^{\mathrm{o}}\\ \frac{\partial^2 \mathrm{J}_2^{\mathrm{o}}}{\partial\mathbf{\Sigma}\partial\Delta\lambda} &= \left(\partial_{\Delta\lambda}\mathbb{H}_1^{\mathrm{L}} \circ\bullet \overline{\mathbf{\Sigma}}_1\right) + \left(\mathbb{H}_1^{\mathrm{L}} \circ\bullet \partial_{\Delta\lambda}\overline{\mathbf{\Sigma}}_1\right)\\ \frac{\partial^2 \mathrm{J}_3^{\mathrm{o}}}{\partial\mathbf{\Sigma}\partial\Delta\lambda} &= \partial_{\Delta\lambda}\mathrm{J}_3^{\mathrm{o}}\, \left(\overline{\mathbf{\Sigma}}_2^{-\mathrm{T}} \bullet\circ \mathbb{H}_2^{\mathrm{L}}\right) + \mathrm{J}_3^{\mathrm{o}}\, \partial_{\Delta\lambda}\left(\overline{\mathbf{\Sigma}}_2^{-\mathrm{T}} \bullet\circ \mathbb{H}_2^{\mathrm{L}}\right)\end{aligned}$$

$$\begin{aligned}\partial_{\Delta\lambda}\left(\overline{\mathbf{\Sigma}}_2^{-\mathrm{T}} \bullet\circ \mathbb{H}_2^{\mathrm{L}}\right) &= \left(\partial_{\Delta\lambda}\overline{\mathbf{\Sigma}}_2^{-\mathrm{T}} \bullet\circ \mathbb{H}_2^{\mathrm{L}}\right) + \left(\overline{\mathbf{\Sigma}}_2^{-\mathrm{T}} \bullet\circ \partial_{\Delta\lambda}\mathbb{H}_2^{\mathrm{L}}\right)\\ \partial_{\Delta\lambda}\overline{\mathbf{\Sigma}}_2^{-\mathrm{T}} &= -\left(\overline{\mathbf{\Sigma}}_2^{-\mathrm{T}} \boxtimes \overline{\mathbf{\Sigma}}_2^{-\mathrm{T}}\right) \bullet\circ \partial_{\Delta\lambda}\overline{\mathbf{\Sigma}}_2.\end{aligned}$$

B.4 Derivatives for the tangent operator

The partial derivative of a symmetric second-order tensor such as $\mathbf{C}$ with respect to itself gives the symmetric fourth-order identity tensor

$$\partial_{\mathbf{C}}\mathbf{C} = \mathbb{S} = \frac{1}{2}\ [(\mathbf{I}\otimes\mathbf{I}) + (\mathbf{I}\boxtimes\mathbf{I})].$$

With this notation, the derivative of the second Piola-Kirchhoff stress tensor with respect to the right Cauchy-Green strain tensor is given by

$$\partial_{\mathbf{C}}\mathbf{S} \quad = \quad \partial_{\mathbf{C}^{\mathrm{e}}}\mathbf{S} \bullet\circ \partial_{\mathbf{C}}\mathbf{C}^{\mathrm{e}} \bullet\circ \mathbb{S}$$

with

$$\begin{aligned}
\partial_{\mathbf{C}^{\mathrm{e}}}\mathbf{S} &= \mathbf{F}^{\mathrm{pl}\,-1}\cdot\partial_{\mathbf{C}^{\mathrm{e}}}\mathbf{S}^{\mathrm{e}}\cdot\mathbf{F}^{\mathrm{pl}\,-\mathrm{T}}\\
\partial_{\mathbf{F}^{\mathrm{pl}}}\mathbf{S} &= -\left(\mathbf{F}^{\mathrm{pl}\,-1}\otimes\mathbf{F}^{\mathrm{pl}\,-1}\right)\cdot\mathbf{S}^{\mathrm{e}}\cdot\mathbf{F}^{\mathrm{pl}\,-\mathrm{T}}\\
&\quad -\mathbf{F}^{\mathrm{pl}\,-1}\cdot\mathbf{S}^{\mathrm{e}}\cdot\left(\mathbf{F}^{\mathrm{pl}\,-\mathrm{T}}\boxtimes\mathbf{F}^{\mathrm{pl}\,-\mathrm{T}}\right),
\end{aligned}$$

where,

$$\begin{aligned}
\partial_{\mathbf{C}^{\mathrm{e}}}\mathbf{S}^{\mathrm{e}} &= -\left[\mathbf{C}^{\mathrm{e}\,-1}\otimes\mathbf{C}^{\mathrm{e}\,-1}\right]\bullet\circ\mathbb{S}\cdot\boldsymbol{\Sigma} + \mathbf{C}^{\mathrm{e}\,-1}\cdot\partial_{\mathbf{C}^{\mathrm{e}}}\boldsymbol{\Sigma}\\
\partial_{\mathbf{C}^{\mathrm{e}}}\boldsymbol{\Sigma} &= \left[1/2\ \lambda\ \mathrm{J}^2\left(\mathbf{I}\ \oplus\ \mathbf{C}^{\mathrm{e}\,-1}\right) + \mu\ (\mathbf{I}\otimes\mathbf{I})\right]\bullet\circ\mathbb{S}.
\end{aligned}$$

C Parameter identification for AZ31 for constant r-values

This appendix presents the model parameter for different constant r-values, specifically, at strain values of 0.03, 0.08 and 0.12. This is done to complement the parameter identification discussed in Chapter 8. The resulting predictive capabilities are demonstrated by the corresponding plots. Following the pronounced anisotropy in terms of r-value, this study focuses on the alloy AZ31.

parameter set based on constant r-value taken at a strain value of 0.3						
	$\mathbb{H}_1$			$\mathbb{H}_2$		
	A	B	C	A	B	C
c_1	-11.2193	-1.0924	4.6275	-7.7089	1.3193	5.3303
c_2	1.4896	0.8801	5.4833	1.8625	0.4666	1.2357
c_3	10.1685	0.3848	2.4757	5.0632	1.0808	3.1638
c_4	6.4143	0.5171	2.3785	1.3950	-3.4689	4.0407
parameter set based on constant r-value taken at a strain value of 0.8						
	$\mathbb{H}_1$			$\mathbb{H}_2$		
	A	B	C	A	B	C
c_1	9.2924	2.7691	0.0000	-4.5413	2.3573	2.8926
c_2	-1.4837	0.8591	2.6207	3.4222	-1.3207	0.4471
c_3	-8.9143	-0.8518	2.8870	3.9238	1.3800	1.0832
c_4	-5.6629	-1.9804	0.1236	0.3681	-2.4746	1.0662
parameter set based on constant r-value taken at a strain value of 0.12						
	$\mathbb{H}_1$			$\mathbb{H}_2$		
	A	B	C	A	B	C
c_1	-16.1633	-1.6170	0.0499	5.1351	0.6124	2.6175
c_2	-5.6270	-0.5673	15.5447	-19.6961	8.8103	0.0409
c_3	25.7463	0.6664	14.8840	2.3562	0.0262	2.5453
c_4	-14.0594	-10.1521	0.0298	-3.0257	1.2755	3.6220

Table C.1: Parameter sets for AZ31 corresponding to the anisotropic material model (see Chapter 3) for constant r-values taken at the strain values 0.3, 0.8 and 0.12.

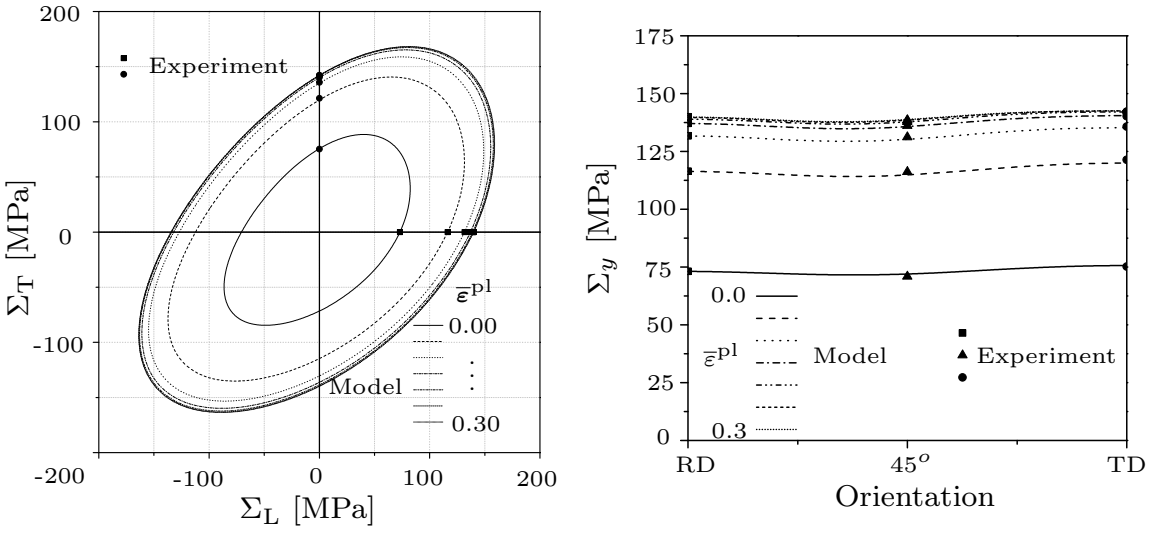

(a) Yield surfaces

(b) Stress as a function of orientation

Figure C.1: Iso-strain curves and stress responses as a function of the material orientation for plastic strain levels ranging from 0 to 0.3 at a strain rate of 0.02/s based on the parameter set identified for a constant r-value at a strain value of 0.03.

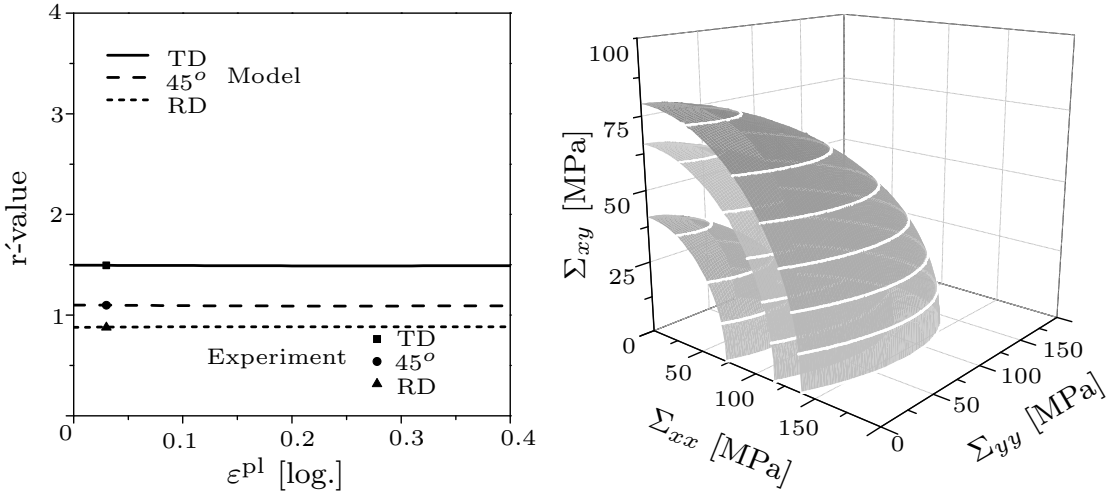

(a) r-value

(b) Iso-strain contours

Figure C.2: r'-values as a function of the plastic strain and convex iso-strain contour surfaces at a strain rate of 0.02/s based on the parameter set identified for a constant r-value at a strain value of 0.03.

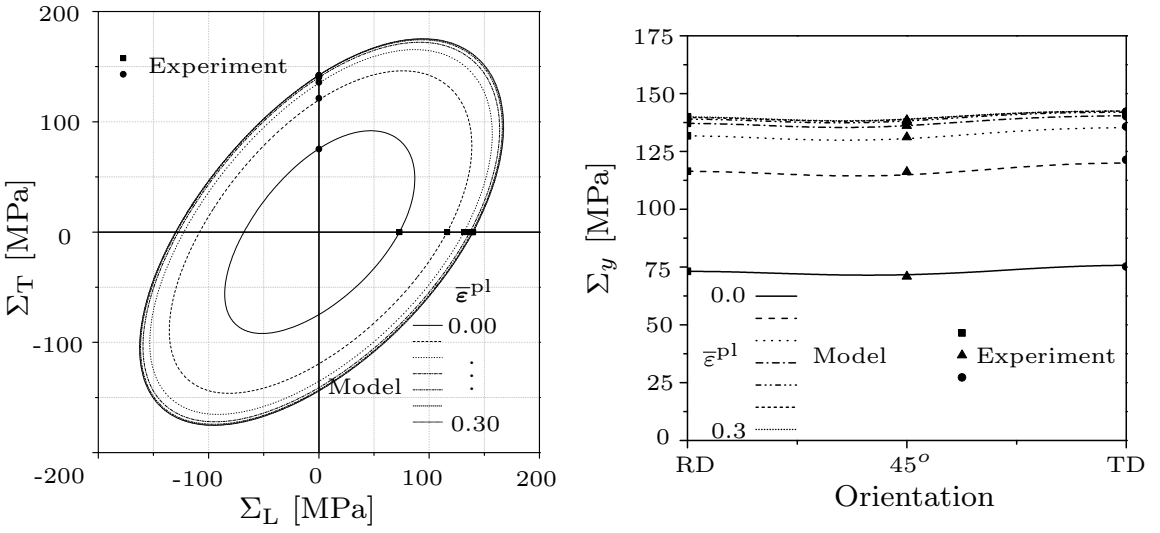

(a) Yield surfaces

(b) Stress as a function of orientation

Figure C.3: Iso-strain curves and stress responses as a function of the material orientation for plastic strain levels ranging from 0 to 0.3 at a strain rate of 0.02/s based on the parameter set identified for a constant r-value at a strain value of 0.08.

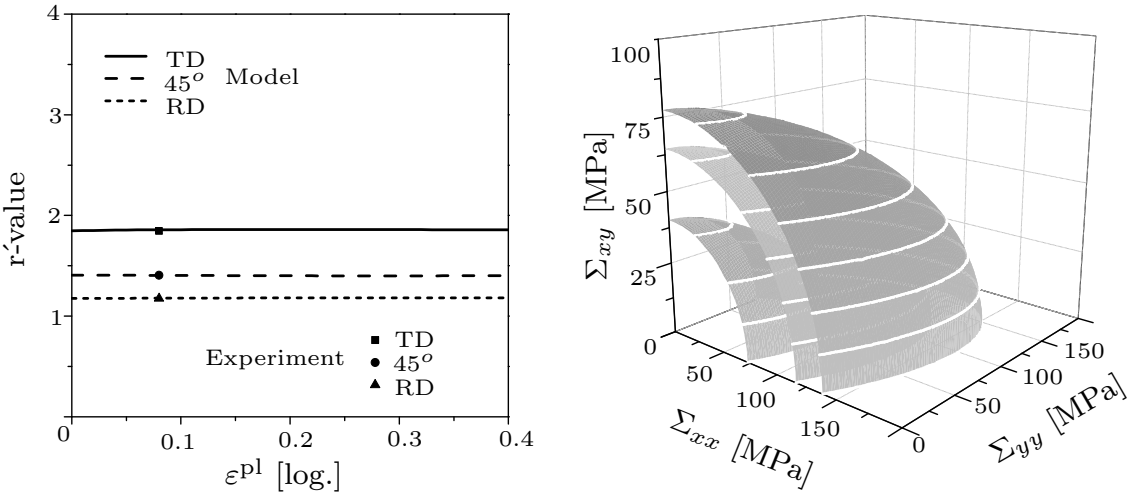

(a) r-value

(b) Iso-strain contours

Figure C.4: r'-values as a function of the plastic strain and convex iso-strain contour surfaces at a strain rate of 0.02/s based on the parameter set identified for a constant r-value at a strain value of 0.08.

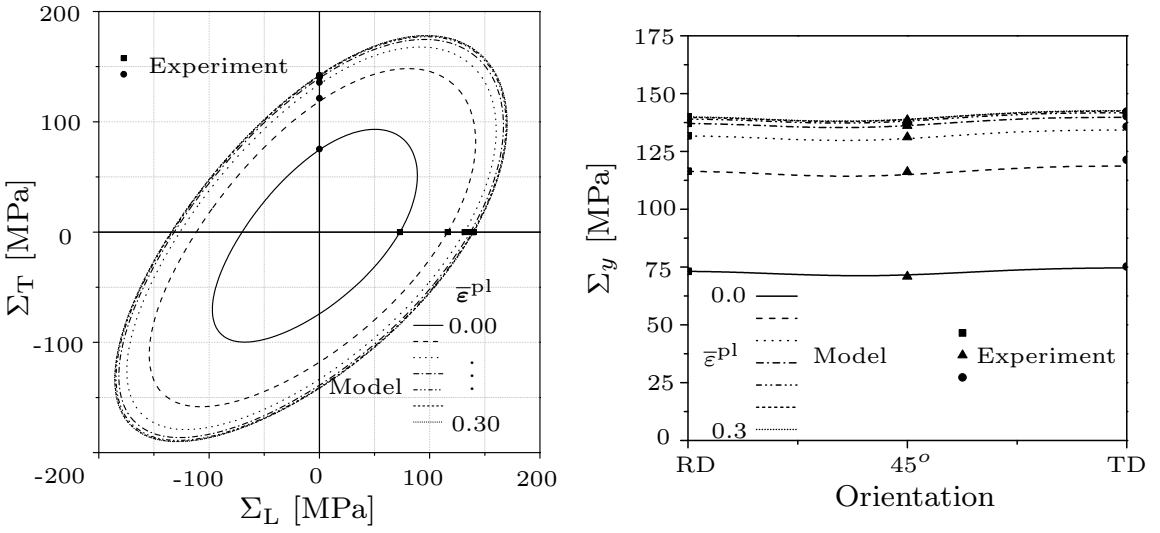

(a) Yield surfaces

(b) Stress as a function of orientation

Figure C.5: Iso-strain curves and stress responses as a function of the material orientation for plastic strain levels ranging from 0 to 0.3 at a strain rate of 0.02/s based on the parameter set identified for a constant r-value at a strain value of 0.12.

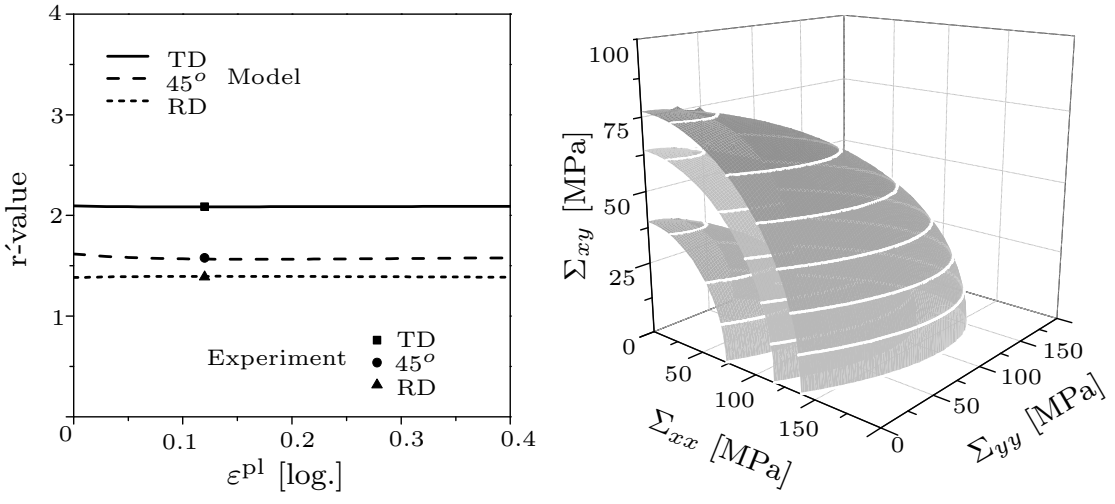

(a) r-value

(b) Iso-strain contours

Figure C.6: r'-values as a function of the plastic strain and convex iso-strain contour surfaces at a strain rate of 0.02/s based on the parameter set identified for a constant r-value at a strain value of 0.12.

Bibliography

Agnew, S. & Duygulu, O. (2005): *Plastic anisotropy and the role of non-basal slip in magnesium alloy AZ31B*, in: International Journal of Plasticity, Volume 21, 1161–1193.

Agnew, S. R. & Duygulu, O. (2003): *A mechanistic understanding of the formability of magnesium: Examining the role of temperature on the deformation mechanisms*, in: Materials Science Forum, Volume 419-422, 177–188.

Banabic, D. (2007): *Advanced methods in metal forming*, Springer 2007.

Banabic, D., Bunge, H. J., Poehlandt, K. & Tekkaya, A. E. (2000): *Formability of metallic materials*, Springer 2000.

Bohlen, J., Nurenburg, M., Senn, J., Letzig, D. & Agnew, S. (2007): *The texture and anisotropy of magnesium-zinc-rare earth alloy sheets*, in: Acta Materialia, Volume 55, 2101–2112.

Borst, R. (1991): *The zero-normal-stress condition in plane-stress and shell elastoplasticity*, in: Communications in Applied Numerical Methods, Volume 7, 29–33.

Brozzo, P., DeLuca, P. & Rendina, R. (1972): *A new method for the prediction of formability limits in metal sheets*, in: Proc. 7th biennal Conf. IDDR, .

Butuc, M. (2004): *Forming limit diagrams. Definition of plastic instability criteria* 2004, Dissertation, Engineering Faculty of Porto University.

Cazacu, O. & Barlat, F. (2001): *Generalization of Drucker's yield criterion to orthotropy*, in: Journal of Mathematics and Mechanics of Solids, Volume 6, 513–630.

Cazacu, O. & Barlat, F. (2003): *Application of the theory of representation to describe yielding of anisotropic aluminum alloys*, in: International Journal of Engineering Science, Volume 41, 1367–1385.

Cazacu, O. & Barlat, F. (2004): *A criterion for description of anisotropy and yield differential effects in pressure-insensitive metals*, in: International Journal of Plasticity, Volume 20, 2027–2045.

Chaboche, J., Dang-Van, K. & Cordier, G. (1979): *Modelization of strain memory effect on the cyclic hardening of SS316 stainless steel*, in: *Transactions of the 5th International Conference on Structural Mechanics in Reactor Technology*, 1979, Volume L.

Chang, Q., Li, D., Peng, Y. & Zeng, X. (2007): *Experimental and numerical study of warm deep drawing of AZ31 magnesium alloy sheet*, in: International Journal of Machine Tools & Manufacture, Volume 47, 436–443.

Chen, F. & Huang, T. (2003): *Formability of stamping magnesium-alloy AZ31 sheets*, in: Journal of Materials Processing Technology, Volume 142, 643–647.

Ciarlet, P. (1988): *Mathematical elasticity. Volume I: Three-dimensional elasticity*, North-Holland Publishing Company Amsterdam 1988.

Dafalias, Y. (1979): *Anisotropic hardening of initially orthotropic materials*, in: ZAMM, Volume 59, 437–446.

Dafalias, Y., Schick, D. & Tsakmakis, C. (2003): *A simple model for describing yield surface evolution during plastic flow*, Springer 2003.

Doege, E. & Dröder, K. (2001): *Sheet metal forming of magnesium wrought alloys - formability and process technology*, in: Journal of Material Process Technology, Volume 117, 276–281.

Dröder, K. (1999): *Untersuchungen zum Umformen von Feinblechen aus-Magnesiumknetlegierungen* 1999, Dissertation, Universität Hannover.

Drucker, D. (1949): *Relation of experiments to mathematical theories of plasticity*, in: Journal of Applied Mechanics, Volume 16, 349–357.

Drucker, D. (1964): *On the postulate of stability of material in the mechanics of continua*, in: Journal of Mechanique, Volume 3, 2, 235–249.

Erichsen, A. (1914): *A new test for thin sheets*, in: Stahl and Eisen, Volume 34, 879–882.

Feigenbaum, H. & Dafalias, Y. (2004): *Modeling yield surface evolution with distortional hardening*, in: International Journal of Plasticity, Volume 20, 2027–2045.

Graff, S. (2007): *Michromechanical modeling of the deformation of HCP metals* 2007, Dissertation, Technical University of Berlin.

Hantzsche, K., Bohlen, J., Wendt, J., Kainer, K., Yi, S. & Letzig, D. (2010): *Effect of rare earth additions on microstructure and texture development of magnesium alloy sheets*, in: Scripta Materialia, Volume 63, 725–730.

Hasek, V. (1973): *On the strain and stress states in drawing of large irregular sheet metal components*, Technical report, University of Stuttgart, 1973.

Hasek, V. (1978): *Research and theoretical description concerning the influences on the FLDs*, in: Blech Rohre Profile, Volume 25, 213–220.

Hill, R. (1948): *The theory of the yielding and plastic flow of anisotropic metals*, in: Proceeding of the Royal Society A, Volume 193, 281–297.

Hill, R. (1952): *On discontinuous plastic states, with special reference to localized necking in thin sheets*, in: Journal of the Mechanics and Physics of Solids, Volume 1, 19–30.

Hill, R. (1968): *On constitutive quantities for simple materials*, in: Journal of the Mechanics and Physics of Solids, Volume 16, 229–242;315–322.

Hill, R. (1990): *Constitutive modeling of orthotropic plasticity in sheet metals*, in: Journal of the Mechanics and Physics of Solids, Volume 38, 405–417.

Hosford, W. (1966): *Texture strengthening*, in: Metals Engineering Quarterly, Volume 6, 13–19.

Hosford, W. (1993): *The mechanics of crystals and textured polycrystals*, Oxford University Press 1993.

Hosford, W. & Allen, T. (1973): *Twinning and directional slip as a cause for a strength differential effect*, in: Metallurgical and Materials Transactions B, Volume 4, 5, 1424–1425.

Hosford, W. & Caddell, R. (2007): *Metal Forming - Mechanics and Metallurgy*, 3rd Edition, Cambridge University Press 2007.

Hutchinson, J. & Neale, K. (1978a): *Sheet necking- I. Validity of plane stress assumptions of the long-wavelength approximation*, in: Mechanics of Sheet Metal Forming, , 111–126.

Hutchinson, J. & Neale, K. (1978b): *Sheet necking- II. Time-independent behavior*, in: Mechanics of Sheet Metal Forming, , 127–153.

Hutchinson, J. & Neale, K. (1978c): *Sheet Necking- III. Strain-rate effects*, in: Mechanics of Sheet Metal Forming, , 269–285.

Karafillis, A. & Boyce, M. (1993): *A general anisotropic yield criterion using bounds and a transformation weighting tensor*, in: Journal of the Mechanics and Physics of Solids, Volume 41, 1859–1886.

Keeler, S. & Backofen, W. (1963): *Plastic instability and fracture in sheets stretched over rigid punches*, in: Transaction of The ASM, Volume 56, 25–48.

Keeler, S. & Brazier, W. (1977): *Relationship between laboratory material characteristics and press shop formability*, in: Microalloying, Volume 75, 517–530.

Kelley, E. & Hosford, W. (1968): *The deformation characteristics of textured magnesium*, in: Transactions of the Metallurgical Society of AIME, Volume 242, 654–661.

Kintzel, O. (2007): *Modeling of elasto-plastic material behavior and ductile micropore damage of metallic materials at large deformations* 2007, Dissertation, Ruhr-Universität Bochum.

Kintzel, O. & Basar, Y. (2006): *Fourth-order tensors-tensor differentiation with application to continuum mechanics*, in: Applied Mathematics and Mechanics, Volume 86, 291–311.

Kocks, U., Tome, C. & Wenk, H. (1998): *Texture and anisotropy*, Cambridge University Press 1998.

Kokkonen, V. & Hygren, G. (1959): *Investigation into the accuracy of the Erichsen cupping test*, in: Sheet Metal Industries, Volume 36, 167–178.

Kuroda, M. & Tvergaard, V. (2000): *Forming limit diagrams for anisotropic metal sheets with different yield criteria*, in: Journal of Solids and Structures, Volume 37, 5037–5059.

Lee, E. H. & Liu, D. T. (1967): *Finite strain elastic-plastic theory with application to plane-wave analysis*, in: Applied Physics, Volume 38, 19–27.

Lou, X., Li, M., Boger, R., Agnew, S. & Wagoner, R. (2007): *Hardening evolution of AZ31B Mg sheet*, in: International Journal of Plasticity, Volume 23, 44–86.

Marciniak, Z. (1965): *Stability of plastic shells under tension with kinematic boundary conditions*, in: Archives of Mechanics, Volume 17, 577–592.

Marciniak, Z. & Kuczynski, K. (1967): *Limit strains in the processes of stretch-forming sheet metal*, in: Journal of Mechanical Sciences, Volume 9, 609–620.

Marciniak, Z., Kuczynski, K. & Pokora, T. (1973): *Influence of the plastic properties of a material on the FLD for sheet metal in tension*, in: Journal of Mechanical Sciences, Volume 15, 789–805.

Mosler, J. (2007): *On the numerical modeling of localized material failure at finite strains by means of variational mesh adaptation and cohesive elements*, Habilitaion, Ruhr-Universität Bochum 2007.

Nakazima, K., Kikuma, T. & Hasuka, K. (1971): *Study on the formability of steel sheets*, Technical report, Yawata, 1971.

Odqvist, F. (1933): *Die Verfestigung von flusseisenähnlichen Körpern*, in: Journal of Applied Mathematics and Mechanics, Volume 13, 360–363.

Ogden, R. (1984): *Non-linear elastic deformations*, Dover Publications, Inc. Mineola, new York 1984.

Palaniswamy, H., Ngaile, G. & Altan, T. (2004): *Finite element simulation of magnesium alloy sheet forming at elevated temperatures*, in: Journal of Material Process Technology, Volume 146, 52–60.

Palumbo, G., Sorgente, D., Tricarico, L., Zhang, S. & Zheng, W. (2007): *Numerical and experimental investigations on the effect of the heating strategy and punch speed on the warm deep drawing of magnesium alloy AZ31*, in: Journal of Material Processing Technology, Volume 191, 342–346.

Peng, Y., Chang, Q., Li, D., Hu, J. & Zeng, X. (2007): *Numerical simulation of warm deep drawing of AZ31 magnesium alloy sheet with variable blank holder force*, in: Key Engineering Materials, Volume 340-341, 639–644.

Polmear, I. (2006): *Light alloys*, 4 Edition, Elsevier 2006.

Simo, J. & Hughes, T. (1998): *Computational inelasticity*, Springer 1998.

Stutz, L., Letzig, D. & Kainer, K. (2009): *Influence of process temperature on the formability of AZ31 magnesium alloy sheets*, in: Kainer, K. (Ed.): *Magnesium-8th International Conference on Magnesium Alloys and their Application*, 2009, pp. 571–576.

Swift, H. (1952): *Plastic instability under plane stress*, in: Journal of the Mechanics and Physics of Solids, Volume 1, 1–16.

Truesdell, C. (1955): *Hypo-elasticity*, in: Journal of Rational Mechanics and Analysis, Volume 4, 83–133.

Truesdell, C. & Noll, W. (1965): *The nonlinear field theories*, Volume 3, Springer-Verlag 1965.

von Mises, R. (1928): *Mechanics of plastic deformation of crystals*, in: Applied Mathematics and Mechanics, Volume 592, 8, 161–185.

Wonsiewicz, B. & Backofen, W. (1967a): *Plasticity of magnesium crystals*, in: Transactions of the Metallurgical Society of AIME, Volume 239, 1422–1431.

Wonsiewicz, B. C. & Backofen, W. A. (1967b): *Independent slip systems and ductility of hexagonal polycrystals*, in: Transactions of the Metallurgical Society of AIME, Volume 239, 1422–1433.

Wu, H. (2005): *Continuum mechanics and plasticity*, Modern Mechanics and Mathematics, Chapman & Hall/CRC Press 2005.

Xiao, H., Bruhns, O. T. & Meyers, A. (2006): *Elastoplasticity beyond small deformations*, in: Acta Materialia, Volume 182, 31–111.

Yi, S., Bohlen, J., Heinemann, F. & Letzig, D. (2010): *Mechanical anisotropy and deep drawing behaviour of AZ31 and ZE10 magnesium alloy sheets*, in: Acta Materialia, Volume 58, 592–605.